UNIVERSITY OF OKLAHOMA

GRADUATE COLLEGE

BIONANOFIBER-BASED NANOSTRUCTURE FABRICATION AND APPLICATIONS

A DISSERTATION

SUBMITTED TO THE GRADUATE FACULTY

in partial fulfillment of the requirements for the

Degree of

DOCTOR OF PHILOSOPHY

By

LIN WANG
Norman, Oklahoma
2017

Downloaded from SHAREOK. Persistent Handle URL: https://hdl.handle.net/11244/52419

BIONANOFIBER-BASED NANOSTRUCTURE FABRICATION AND APPLICATIONS

A DISSERTATION APPROVED FOR THE
DEPARTMENT OF CHEMISTRY AND BIOCHEMISTRY

BY

_____
Dr. Chuanbin Mao, Chair

_____
Dr. Wai Tak Yip

_____
Dr. Zhibo Yang

_____
Dr. Yihan Shao

_____
Dr. Scott D. Russell

© Copyright by LIN WANG 2017
All Rights Reserved.

Acknowledgements

The pursuing of the PhD degree is like a journey, a journey full of challenge and hardness. However, I was not alone in this journey and was accompanied by many people who were generous to give me encouragement, help and support all the time. The experiences in these years make me strong, not only academically but also spiritually.

First, I would like to express my deepest appreciation to my supervisor, Professor Chuanbin Mao, for his constant guidance and support throughout the project. Without his expert advice, it is impossible to overcome the numerous obstacles encountered in my research and complete this dissertation. His impact on me is not limited to the research, while the rigorous attitude and enthusiasm to science from him will be more influential for my future life.

My special thanks also go to all of my dissertation and advisory committee members, Dr. Scott D. Russell, Dr. Wai Tak Yip, Dr. Zhibo Yang, Dr. Yihan Shao, Dr. Ann H. West and Dr. Jun Li. Thanks very much for your time and valuable suggestions in my research. I would also like to thank Dr. Wai Tak Yip for his sincere help when I was working as a teach assistant.

I extend my appreciation to the members of Samuel Roberts Noble Microscopy Laboratory, Dr. Gregory W. Strout, Dr. Preston Larson and Dr. Scott D. Russell for their professional advice and technical support of TEM and SEM.

My appreciation also goes to all the current and former members of Dr. Mao's research group. They are all very friendly persons and helped me a lot in both research and life. I owe special thanks to Dr. Penghe Qiu and Dr. Jianglin Wang for the hundreds

of helpful discussions and my countless annoying questions. They were both very patient, knowledgable and imparted me with everything they know without reservation.

Finally, I am extremely grateful to my parents and my husband for their continuous understanding, support and sacrifice during these years. They are a great source of motivation and strength which helped me to go further than I could have hoped.

Table of Contents

Acknowledgements iv

List of Tables x

List of Figures xi

Abstract xv

Chapter 1: Introduction 1

1.1 General background 1

1.2 Bionanofibers and their properties 1

1.2.1 Bacterial flagella 1

1.2.2 Filamentous bacteriophage 6

1.3 Fabrication of 1D biotemplated nanostructures 12

1.3.1 Flagella templated 1D nanostructures 13

1.3.2 Phage templated 1D nanostructures 14

1.3.3 TMV templated 1D nanostructures 16

1.4 Bionanofiber-based higher ordered structures 19

1.4.1 1D bundles 19

1.4.2 2D films 22

1.4.3 3D bulk materials 24

1.5 Applications of biofiber templated nanomaterials and their assemblies 24

1.5.1 Energy devices 25

1.5.2 Medical applications 29

Chapter 2: Tuning Electrostatic Nanoparticle Assembly on Filamentous Protein-based Biotemplates without the Need of Biotemplate Modification 32

2.1 Introduction 32
2.2 Materials and Experiments 36
2.2.1 Materials 36
2.2.2 Flagella amplification and purification 36
2.2.3 Phage amplification and purification 37
2.2.4 Synthesis of PEI coated AuNPs directly in water 37
2.2.5 Synthesis of AuNPs in oil phase for study of size effect on the biotemplated assembly 38
2.2.6 Synthesis of magnetic NPs (MNPs) 39
2.2.7 Synthesis and phase transfer of CdSe/ZnS quantum dots (QDs) 39
2.2.8 PEI coating of AuNPs, MNPs and QDs 39
2.2.9 Assembly of NPs onto biotemplates 39
2.2.10 Construction of engineered flagella displaying foreign peptides 40
2.2.11 Characterization by Transmission Electron Microscopy (TEM) 42
2.3 Results and Discussion 42
2.3.1 Assembly of AuNPs on flagella templates 42
2.3.2 Effect of PEI molecular weight on AuNPs assembly 47
2.3.3 Effect of AuNPs size on the assembly 48
2.3.4 Control over the density of AuNPs on each flagellum template 49
2.3.5 Assembly of AuNPs on engineered flagella 53
2.3.6 Generality of the method 58
2.4 Conclusion 61

Chapter 3: Solution phase processed thin films made from biotemplated 1D plasmonic nanoparticles array for solar thermoelectric generation 62
3.1 Introduction 62
3.2 Materials and Experiments 64
3.2.1 Materials 64
3.2.2 Amplification and purification of flagella template 64
3.2.3 Flagella templated assembly of AuNPs 65
3.2.4 Tuning optical property of AuNPs/flagella assemblies through seeded post-growth 65
3.2.5 Fabrication of plasmonic thin films with AuNWs or AuNPs 66
3.2.6 Transmission electron microscopy (TEM) and scanning electron microscopy (SEM) characterization 67
3.2.7 Temperature profile measurement 67
3.2.8 Assembly and testing of the STEG device 67
3.3 Results and Discussion 68
3.3.1 Fabrication of AuNPs-flagella assemblies 68
3.3.2 Manipulation of extinction spectra of AuNPs/flagella assembly in solution 71
3.3.3 Thin film fabrication with plasmonic AuNWs 73
3.3.4 Plasmonic AuNWs thin film based solar thermoelectric generation (STEG) 78
3.4 Conclusion 81

Chapter 4: Virus activated artificial ECM induces the osteoblastic differentiation of mesenchymal stem cells without osteogenic supplements 83
4.1 Introduction 83
4.2 Materials and Experiments 86
4.2.1 Peptides display and films fabrication 86
4.2.2 Cell culture and seeding 87
4.2.3 Cell proliferation 87
4.2.4 Immunofluorescence staining 88
4.2.5 Real-time polymerase chain reaction (PCR) 88
4.2.6 Assay of alkaline phosphatase activity 89
4.2.7 Statistical analyses 90
4.3 Results 90
4.3.1 Self-assembly of phage-based films 90
4.3.2 Morphology and nanotopography of phage-based films 92
4.3.3 Cell adhesion on the phage-based films 95
4.3.4 Cell proliferation and differentiation on the phage-based films 98
4.4 Discussion and Conclusion 102
References 108
Appendix A: List of Abbreviations 128
Appendix B: List of Copyrights and Permissions 131

List of Tables

Table 2.1: Oligonucleotide sequences of peptides displayed on flagella. 41

Table 2.2: Sequences displayed on engineered flagella. G, glycine; E, glutamate; C, cysteine. 54

Table 2.3: Zeta potential of wild type and engineered flagella. 55

Table 4.1: The primer sequences for Real-time PCR analysis. 89

List of Figures

Figure 1.1: Flagellum structure. 3

Figure 1.2: Structure of flagellin protein. 4

Figure 1.3: Morphology of flagella. 6

Figure 1.4: TEM image of wild type M13 phages negatively stained with 1% UA. 8

Figure 1.5: The structure of M13 and Fd bacteriophage particle. 8

Figure 1.6: Advantages of phages as biotemplates for nanomaterial synthesis and assembly. 12

Figure 1.7: Morphology manipulation of flagella templated silica nanotubes synthesized under different pH values. 14

Figure 1.8: TEM images of ZnS, CdS, CoPt and FePt nanowires by using engineered M13 phage as templates. 16

Figure 1.9: TMV templated CdS, PdS and SiO_2 nanowires. 18

Figure 1.10: Ca^{2+} induced phage bundles..... 21

Figure 1.11: Phage films fabricated through layer-by-layer method. 23

Figure 1.12: TiO_2/SWNTs nanocomposites integrated DSSC..... 26

Figure 1.13: LIB anode materials prepared by vertical array of TMV templates. 28

Figure 2.1: Sketch of the s-PEI enabled electrostatic assembly of NPs, including gold NPs (AuNPs), magnetic NPs (MNPs) and quantum dots (QDs) onto filamentous biotemplates (bacteria flagella and pili, and filamentous phages) and the advantages of the method. 35

Figure 2.2: Illustration of flagella purification from bacteria..... 37

Figure 2.3: Construction of recombinant flagella through genetic engineering..... 41

Figure 2.4: TEM images of 1D AuNPs array obtained through flagella templated assembly. 44

Figure 2.5: Mechanism investigation of AuNPs assembly onto flagella. 46

Figure 2.6: Assembly of AuNPs, coated by PEI of different average M.W. 48

Figure 2.7: AuNPs of different sizes synthesized through an oil phase strategy. 49

Figure 2.8: Assembly of AuNPs of different diameters onto the flagella templates..... 49

Figure 2.9: Manipulation of AuNPs assembling density on flagella templates. 51

Figure 2.10: Plot of the corresponding AuNPs density on flagella template under different flagella concentrations. 52

Figure 2.11: Optical property of the AuNPs density on flagella template under different flagella concentrations. 52

Figure 2.12: Crystal structure of flagellin. 54

Figure 2.13: AuNPs alignment on wild type and engineered flagella..... 57

Figure 2.14: Demonstration of generality of the electrostatic assembly method with different NPs (coated by s-PEI) but same biotemplates (flagella). 59

Figure 3.1: TEM images of flagella templates and AuNPs/flagella assemblies. 69

Figure 3.2: TEM images of AuNPs and AuNPs/flagella assemblies. 70

Figure 3.3: Morphology of post grown AuNPs/flagella complexes. 72

Figure 3.4: Optical property of post grown AuNPs/flagella complexes. 73

Figure 3.5: TEM and Spectrum of 50 nm AuNPs. 73

Figure 3.6: Digital images of plasmonic AuNWs film (b) and AuNPs film (a) coating on copper plates. 74

Figure 3.7: Optical property of plasmonic AuNWs film..... 76

Figure 3.8: Morphology of plasmonic AuNWs film. 76

Figure 3.9: The conversion of solar energy to heat through plasmonic AuNWs film. . 78

Figure 3.10: STEG device. 80

Figure 3.11: Performance of STEG device using plasmonic AuNWs film as solar absorber. 80

Figure 3.12: Infrared camera images of plasmonic AuNWs film during irradiation. ... 81

Figure 4.1: Schematic diagram of using phage display technique to produce biomaterials with both unique nanostructures derived from a layer-by-layer method and functional peptides displayed for directing stem cell fate. 85

Figure 4.2: Mechanism of film formation. 91

Figure 4.3: M13 phage biofibers. 91

Figure 4.4: Characterization of phage-based film materials. 92

Figure 4.5: Morphology of phage-based film derived from the different phage concentrations. 93

Figure 4.6: 3D AFM images of phage films derived from different phage concentrations. 94

Figure 4.7: The average surface roughness (Ra) of phage-based films derived from the different phage concentrations. 95

Figure 4.8: Cell adhesion on the phage-based film derived from both low (a, c, e) and high (b, d, f) phage concentration. 97

Figure 4.9: Cell morphologies of MSCs on different substrates. 98

Figure 4.10: Cell proliferation on the phage-based materials. 99

Figure 4.11: Cell differentiation through immunofluorescence staining. 100

Figure 4.12: Cell differentiation through real-time PCR. 101

Figure 4.13: ALP activity assay..... 102

Abstract

Among various strategies for the synthesis and assembly of nano-scaled structures, bio-templating is an efficient method due to the unique physical and chemical properties of the template bionanomaterials, thus has experienced a rapid and vigorous development in past decades. The works in this dissertation are focused on the one-dimensional (1D) biotemplates, especially filamentous bacteriophages and bacterial flagella. The fabrication of hybrid inorganic/biotemplate 1D nanowires and two-dimensional (2D) films, and the 2D films self-assembled from the biofibers, as well as their potential applications in electric and medical fields were described here.

Firstly, a tunable nanoparticles (NPs) assembly strategy on filamentous protein-based biotemplates which forming 1D nanowires without the need of biotemplate modification was described (Chapter 2). To achieve controlled assembly of NPs on biotemplates, it is usually necessary to either genetically or chemically modify the surface of biotemplates. Here we discovered that simply coating small molecular weight polyethyleneimine (PEI) on NPs triggered their electrostatic assembly on the protein-based biotemplates in a controlled manner. Such strategy is facile and versatile in that the NPs to be assembled and the protein-based biotemplates can be independently changed. The pH values and molecular weights of PEI are the two key factors for the dense assembly of NPs onto the biotemplates. Our method exhibited high flexibility in assembling NPs of different sizes and in controlling the NPs density on the biotemplates, avoiding the costly and tedious steps of modifying biotemplates prior to the assembly. It can assemble multiple types of NPs, regardless of their synthetic methods, onto different wild-type biotemplates such as bacterial flagella, pili, and phages.

Secondly, based on the 1D NPs/flagella assemblies obtained in Chapter 2, we further extended the work to manipulate the optical properties of the 1D structure through a seed-mediated overgrowth process (Chapter 3). The overgrowth process simultaneously increased the AuNPs size on the templates as well as reduced their inter-particle distances, thus inducing 3D coupling of surface plasmon of AuNPs on the template and leading to a significantly enhanced and broadened localized surface plasmon resonance (LSPR) bands. We then took advantage of the broadband absorption property of the overgrown AuNPs assemblies and used them as effective solar absorbers. The as-constructed plasmonic absorber exhibited efficient solar-thermal conversion. When such absorber was used in a solar thermoelectric generation (STEG) device, it has been demonstrated capable of generating 1V voltage under 5x solar irradiation.

In addition, a type of 2D film self-assemblied from genetically engineered phage nanofibers was fabricated as artificial extracellular matrix (aECM), and the osteoblastic differentiation of mesenchymal stem cells on the matrix without osteogenic supplements was demonstrated (Chapter 4). The generated virus-activated aECM was with ordered ridge/groove nanotopography and displayed different fibronectin-derived peptides (RGD, its synergy site PHSRN, and a combination of RGD and PHSRN). The unique nanotopography and the display of RGD and PHSRN could induce the osteoblastic differentiation of mesenchymal stem cells (MSCs) without any osteogenic supplements. The aECM formed through self-assembly and genetic engineering of phage can be used to understand the role of peptide cues in directing stem cell behavior while keeping nanotopography constant. Moreover, the materials showed huge potential in the application of bone regeneration.

Chapter 1: Introduction

1.1 General background

Nanobiomaterial is a multidisciplinary scientific field encompassing life science, material science and nanotechnology principles. Among diverse materials, materials at nanoscale have revealed unique and superior mechanical, optical, electronic and magnetic properties, therefore can be applied in electronics, photonics, catalysis, and tissue engineering. The common strategies to synthesize and assemble the nano-scaled structures include electrospinning,[1-3] directional freezing,[4] polymer-templating and bio-templating.[5] Bio-templating is an efficient method to synthesize and subsequently assemble nanomaterials, thus has experienced a rapid and vigorous development in past decade. Biological materials, such as nucleic acids, lipids, proteins, bacteria and viruses recently have attracted interest as nano-biomaterial building blocks because of their precise and sophisticated hierarchical nanostructures and highly specific molecular recognition capabilities.[6-13] With the use of these materials as biomolecular scaffolds, the functional nanomaterials can be synthesized and assembled into structures which can then be integrated into large-scale devices with desired size, shape, alignment and orientation. The works in this dissertation are focused on the nanostructures fabricated based on the one-dimensional (1D) biotemplates and their applications.

1.2 Bionanofibers and their properties

1.2.1 Bacterial flagella

Biology and structure of bacterial flagella

Bacterial flagella are motion organelles protruding from the surface of bacteria. Structurally, they are protein bionanofibers, which are helically self-assembled from

more than 20,000 copies of identical protein subunit called flagellin (Fig.1.1).[14] A type of widely used biotemplate flagella is from a subspecies of bacterium *Salmonella*, called *Typhimurium*, due to its high-bearing capacity of flagella. The outer diameter of the flagella is about 14 nm while the inner diameter is only 2 nm, and the length varies from tens of nanometers to several micrometers (Fig. 1.1). These bio-nanofibers are easy to be mass produced and purified, and have extraordinary mechanical properties. They are also super stable under high temperature (up to 60°C) and drastic pH (pH3 to pH11).[15-17] Flagellin monomer can be functionally divided into 4 domains: D0, D1, D2 and D3. D0 and D1 domains are conservative and tightly packed into a core, therefore, are important for flagellin polymerization (Fig. 1.2).[18] D3 is solvent-exposed and highly variable, and thus can be used to display foreign peptides.[14]

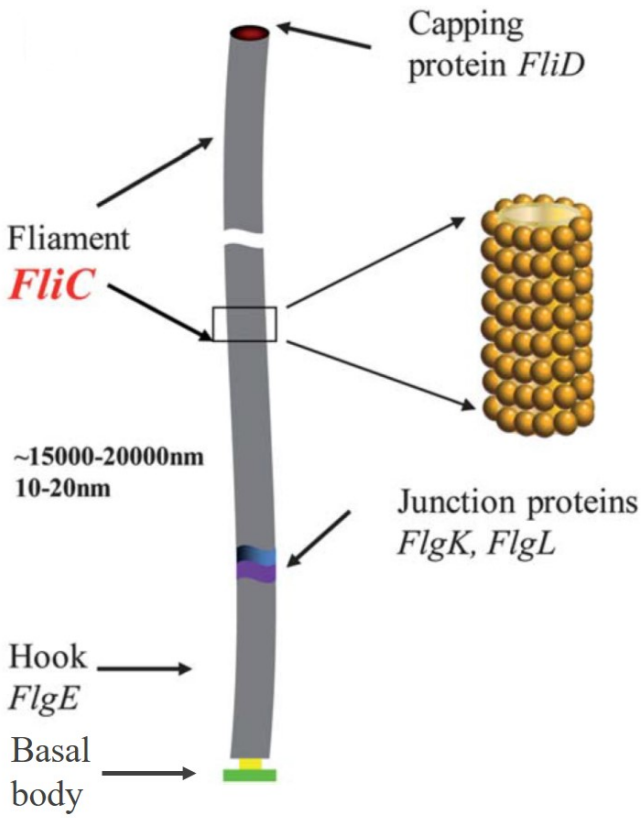


Figure 1.1: Flagellum structure. Flagellum has three components: the basal body, the hook and the filament. The basal body is composed of transmembrane proteins and anchors the flagellum to the bacteria. It is a molecular motor, which rotates the filament. The hook attaches the filament to the basal body. The filament is a molecular propeller and drives the bacterium to move through rotation. The filament part is a biofiber helically self-assembled from flagellin subunits (also called FliC). The diameter of flagellum is about 10 to 20 nm depends on the type of bacteria and the length is up to tens of micrometers. The flagellar filaments purified from the surface of bacteria Salmonella Typhimurium are with a diameter of ~14 nm.[19]

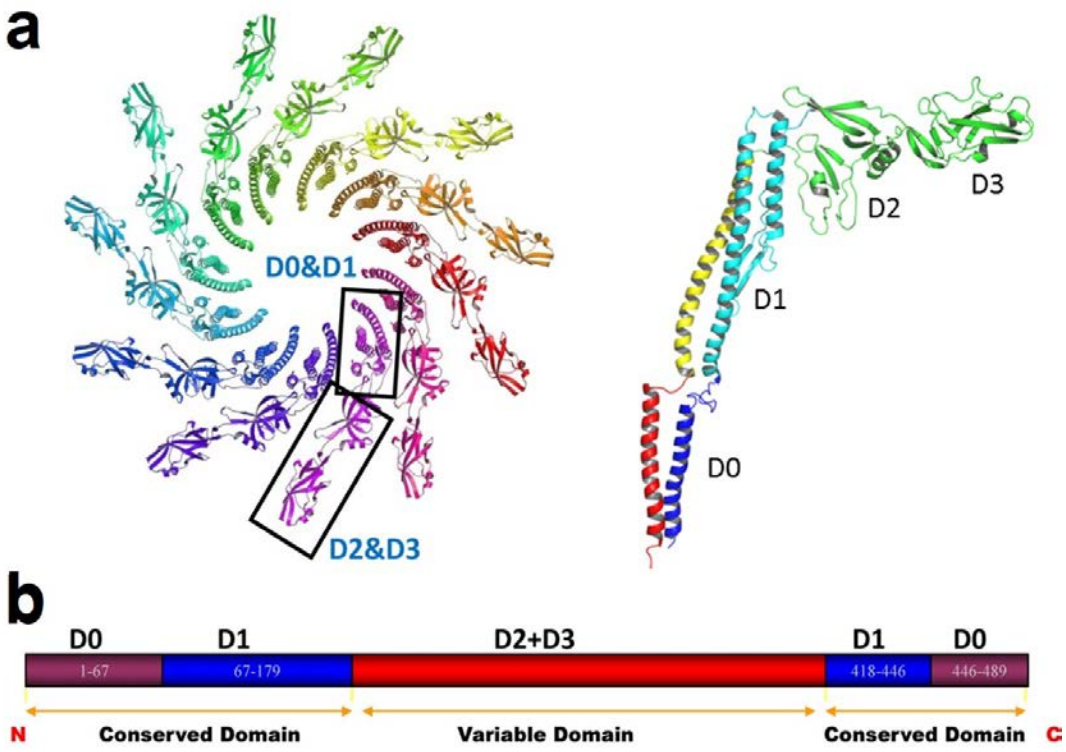


Figure 1.2: Structure of flagellin protein. a) Ribbon diagram of the Cα backbone of flagellum filament and flagellin protein. Flagellin is divided into 4 domains: D0, D1, D2 and D3. Eleven protofilament strands form the helical and tubular structure with D0 and D1 domains tightly packed into core, while D2 and D3 domains extend to the surface. Modified from PDB ID 1UCU.[14] (b) D0 and D1 domains, located at the N- and C-terminals of flagellin are conservative and important for flagellin polymerization. D2 and D3 domains are highly variable and solvent-exposed, and thus insertion of peptides into these domains allows peptide display on the flagellar surface.

Flagella display

Genetically displaying peptides on the surface of flagella is called flagella display.[19-22] For *Salmonella Typhimurium*, D3 domain of flagellin is solvent-exposed and used as the display position (Fig. 1.2). After the flagella display, each flagellin

monomer was fused with the foreign peptide, and after assembly into flagella, the surface chemical and physical properties are modified by the foreign peptide and are uniform and identical along the whole fiber. Unlike other biotemplates, for example, filamentous bacteriophage (fd or M13), which can only display no more than 20 amino acids on the major coat proteins constituting the side walls, flagellin can be inserted with up to 302 amino acids at the highly variable D3 domain without interrupting its self-assembly into functional flagella.[19, 23]

Potential of flagella in nanotechnology

The great stability makes flagella to maintain the intactness under chemical synthesis of inorganic materials. It has been reported that flagellar filaments could also be formed through an *in vitro* assembly of pre-depolymerized flagellin monomers.[24] This fact indicates the probability to manipulate flagella templates with uniform size and tunable length. Furthermore, the configuration of flagella, such as handedness, helical pitch and helical diameter (Fig. 1.3), varies in response to various external stimulations including pH value, ionic strength, temperature and displayed peptide sequences.[19, 25] The diversity of the configuration opens up the possibility of controlling the morphologies of nanomaterials by tuning the morphologies of flagella templates. All these features facilitate the chemical synthesis of inorganic materials with various morphologies on flagella, making them a suitable biotemplate. Moreover, the surface chemistry of flagella can be tuned by displaying foreign peptides through genetic means, which allows further manipulation over the interaction between biomolecules and inorganic complex. Up to 302 amino acids are able to be displayed on each unit protein, which is much higher than other biotemplates. In other words, more sophisticated

surface chemistry manipulation can be achieved on flagella than on other biomolecules, which makes them a better platform for nanomaterial synthesis and assembly as well as for understanding bio-controlled crystal formation. For example, through displaying positively or negatively charged amino acids with different numbers, the surface charge of these bionanofibers can be fully controlled. With their controllable lengths and tunable surface chemistry, flagella are an ideal platform for the controlled synthesis and assembly of inorganic nanocomposites.

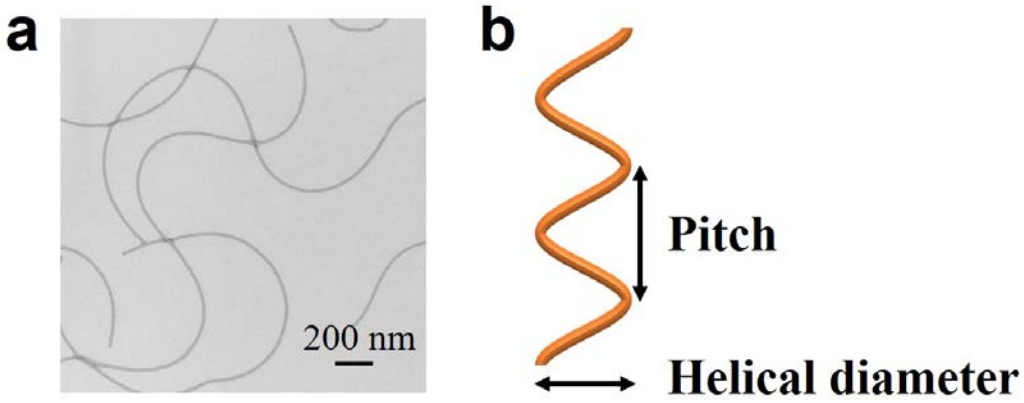


Figure 1.3: Morphology of flagella. a) TEM image of wild type flagella from *Salmonella Typhimurium*, which were negatively stained by 1% uranyl acetate (UA). Natural flagella present sinusoidal wave morphology. b) A filament with normal configuration is helical with a pitch of about 2.2 μm and a helical diameter of about 0.4 μm.

1.2.2 Filamentous bacteriophage

Plant and bacteria viruses, such as M13 bacteriophage, tobacco mosaic virus (TMV)[26] and cowpea mosaic virus (CPMV)[27], played important roles in nanomaterials progress as protein cages or biotemplates, but not only the disease causing organisms.

Most phage used as templates in synthesis and assembly of nanomaterials are filamentous phage strains-M13, fd and fl, although other types of phage such as T4[28-29] and λ[30] are also promising templates. This dissertation will only systematically and comprehensively describe the filamentous bacteriophage based nanobiomaterials.

Biology and structures of phage

Filamentous bacteriophages (also called phage) are bacterial viruses and non-toxic to humans. The phage particles are filamentous and semi-flexible virions with robust physical and chemical properties and can be programmed through genetic engineering. The wild-type filamentous phages are flexible nanofibers of nearly 6nm in diameter and 1μm in length (Fig. 1.4). Inside the virion is a 6407- or 6408-base single-stranded circular viral DNA (ssDNA) (Fig. 1.5). The simple ssDNA encodes all proteins for the phage including 2700 identical copies of the major coat protein, pVIII (encoded by gene VIII), which are helically arranged on the surface to form the side wall and four different types (pIII, pVI, pVII and pIX) of minor coat proteins with two different types on each tip. At one tip of the virion are five copies each of the pIII and pVI (genes III and VI) and the other tip has five copies each of pVII and pIX (genes VII and IX) (Fig. 1.5).[31-32]

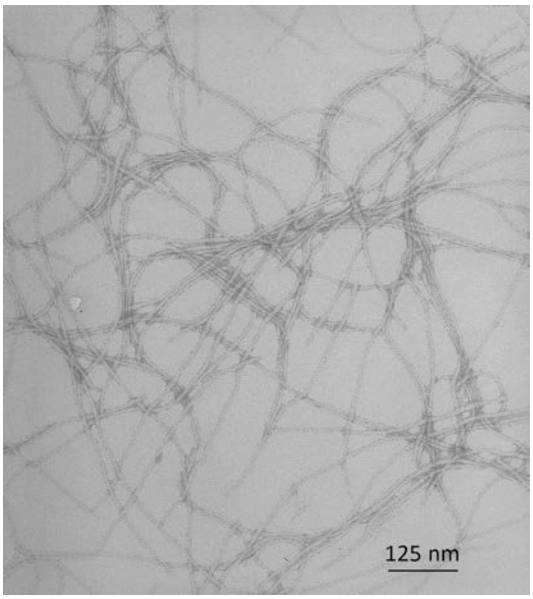


Figure 1.4: TEM image of wild type M13 phages negatively stained with 1% UA.

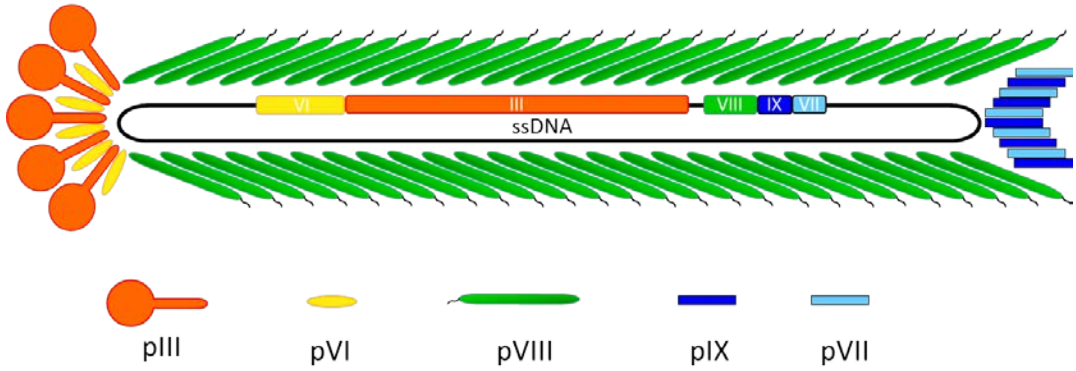


Figure 1.5: The structure of M13 and Fd bacteriophage particle. The single stranded DNA showing the location of coat protein genes is encompassed by 5 types of coat proteins.

The ionic property of filamentous phage contributes to its efficiency as a nanomaterial template. It is dominated by the high expression of the major coat protein pVIII compared to the mere five copies of each minor protein on the surface. The amino terminal of each pVIII protein exposed to the solution includes negatively charged

amino acids (Glu and Asp) with side-chain carboxyl groups extending away from phage surface. The wild-type fd and fl phage shows 1 Glu and 3 Asp on the N-terminal, but M13 phage only shows 1 Glu and 2 Asp with the 12th negatively charged Asp residue replaced by a polar, uncharged Asn residue. At a pH of 8.2, fd and fl have 3.4 negative charges per protein subunit, while M13 has 2.4 negative charges.[33]

The bacteriophage only infects bacteria and does not induce significant toxicity or obvious antibody response in human,[34] thus has been the focus for use in drug delivery and artificial tissue engineering. And fl, fd and M13 phages are non-lytic bacteriophages, the host cells are not adversely affected by the infection, however, the rate of cell growth and division will decrease.[35]

Phage display

All five coat proteins in the phage virion have been used to display foreign peptides or proteins on the amino terminus.[36-40] The most common method is to display designed foreign peptides to pIII or pVIII coat proteins. Moreover, unlike the genetic modification on other protein assemblies, such as flagella, which can only introduce one type of exogenous peptide, two or three different peptides can be simultaneously displayed on different phage coat proteins and this is known as double- and triple-display technique.[41-44] This technology endows phage with multiple functionalities on a single nanoscale structure.

Phage display technique enables the construction of phage display peptide libraries. A phage display library is a heterogeneous mixture of phage clones randomly carrying various foreign DNA to the appropriate site in phage genomes and thus randomly displaying various peptides on phage surfaces.[45] Phage display systems can

be classified according to the recombinant coat proteins. The most popular approach is to fuse the foreign peptides to the N-terminal of the pIII or pVIII protein. pIII-displayed peptide libraries are most widely utilized and commercially available. On the end of this phage particle, a foreign peptide is displayed on all five copies of pIII molecules. Similarly, a foreign peptide is displayed on every copy of the pVIII molecule of the phage particles from the PVIII-displayed peptide libraries called landscape libraries.[46] This kind of libraries are not able to display relatively large foreign peptides (more than about eight amino acids) since the foreign peptide composes a substantial fraction of the total protein coat and will affect the phage assembly. By far the most common application of the phage display peptide libraries are the affinity selection for a target ligand. After several rounds of selection (called biopanning), the phage displayed peptides with the highest binding affinity are determined.[47] The inorganic and organic materials as biopanning targets include metals, metal oxides, semiconductors, magnetics, carbon materials, polymers, organic molecules and others.[48-56] The identified peptides can then be used to modify virions which can be used as templates in further synthesis and assembly of materials with new structures and functions.

Potential of phages in nanotechnology

In comparison to other conventional synthetic templates or biological templates, phage-based synthesis and assembly systems are popular for the following reasons (Fig. 1.6): i) Bacteriophages have a self-correct mechanism and all the particles for one type are identical so they are considered monodisperse NPs; ii) There are many active groups (-NH_2, -COOH) on the phage surface for chemical conjugation with small molecules or nanostructures. In addition, the surface properties of phages can also be controlled by

genetically fusing an exogenous peptide with a coat protein. These characteristics provide ideal positions for nanomaterials synthesis and assembly; iii) Phages can self-assemble into periodically ordered structures, such as liquid crystal, by changing concentration, ionic strength and other variables,[33, 57-59] which can further direct the assembly of nanomaterials into complicated composites; iv) Besides display only one type of exogenous peptides, phage can be engineered to display two or three types of peptides on different coat proteins, so called double- or triple-display. This confers multiple functions (material template, molecule targeting, etc) to individual little phage templates; v) The phages show excellent stability in many acidic, basic and organic solvents thus can stabilize the materials loaded onto them, such as liposomes; vi) Phages can be produced and purified inexpensively on a large scale from natural factories, bacteria, thus promising huge potential in future applications; vii) Phage shows advantages in biomedicine development as a result of the non-toxic properties and strong capability to penetrate brain-blood barriers. Based on above reasons, material scientists have been attracted to seek new opportunities with phage templates in nanotechnology and incorporate them into applications involving catalysis,[60] batteries [61], microelectronics, nonlinear optics, and nanosensors.[62-63]

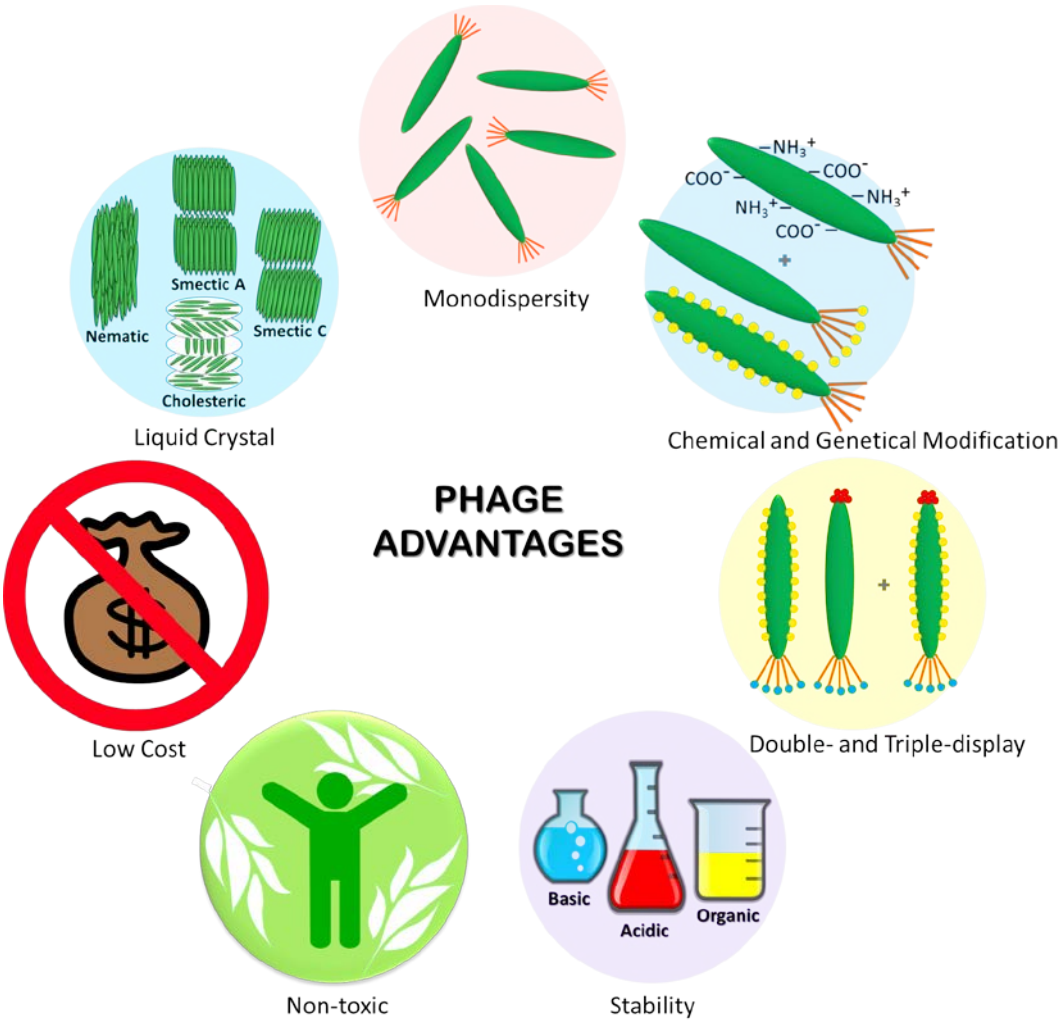


Figure 1.6: Advantages of phages as biotemplates for nanomaterial synthesis and assembly.

1.3 Fabrication of 1D biotemplated nanostructures

1D fibrous biological nanostructure can be used as templates for the synthesis or assembly of nanorods, nanowires and nanotubes. The biological fibrous templates include M13/fd filamentous bacteriophage, bacterial flagella, TMV, microtubule, collagen, etc.[64-66] Most of the templates are precisely self-assembled nanofibers from thousands of same subunits, and with uniform diameter and identical length. This

section will focus on the inorganic 1-D nanomaterials produced on flagella, phage and TMV biological templates of which the surface chemistry is able to be genetically modified.

1.3.1 Flagella templated 1D nanostructures

Recently, flagella have been used for the synthesis of both spherical and tubular inorganic nanomaterials including metals, oxides and quantum dots (QDs).[19, 21-22, 67-70] The current progress in this area can be reflected in three aspects: (i) Metallic nanomaterials: Flagella displaying specific loop peptides have been demonstrated having high affinity to metal ions including Au(I), Cu(II), Co(II), Pd(II), Cd(II) and Ag(I).[70] Followed by a reduction reaction, the NPs or nanotubes of the corresponding metal can be produced; (ii) Oxide nanomaterials: So far titanium oxide (TiO_2) and silica (SiO_2) were synthesized by flagella.[19, 21-22, 68-69, 71]. (iii) QDs: ZnS, ZnS/Mn and CdTe QDs were synthesized by flagella templating.[67] Additionally, it has been reported that both the inside and outside walls of flagella-templated nanotubes could be modified by NPs, i.e. uptake of CdTe QDs into the inner channels and coating of gold, palladium and iron oxide NPs on the outer wall.[21, 72-73] Moreover, flagella exhibit diverse morphologies under different pH values, temperature and ion strength.[74] Based on this phenomenon, Li et al synthesized silica nanotubes (SNTs) templated by flagella and the resultant nanotubes exhibited variable morphologies at different pH values under TEM (Figure 1.7).[19] At pH 4, SNTs were curly and coiled bundles. SNTs exhibited the sinusoidal wave morphology at both pH 8 and 9, but with a shorter wavelength at pH 9. When the pH value was increased to 10.5, SNTs were coiled but containing a single flagella nanofiber in the channel, which is different from the flagella bundles observed

at pH 4. Further increasing the pH to 11, the coiled SNTs became straight. In addition, the peptide sequences displayed on the flagella surface also alter the morphology of SNTs. These results exhibit huge potential of fabricating diverse nanomaterials assisted by flagella.

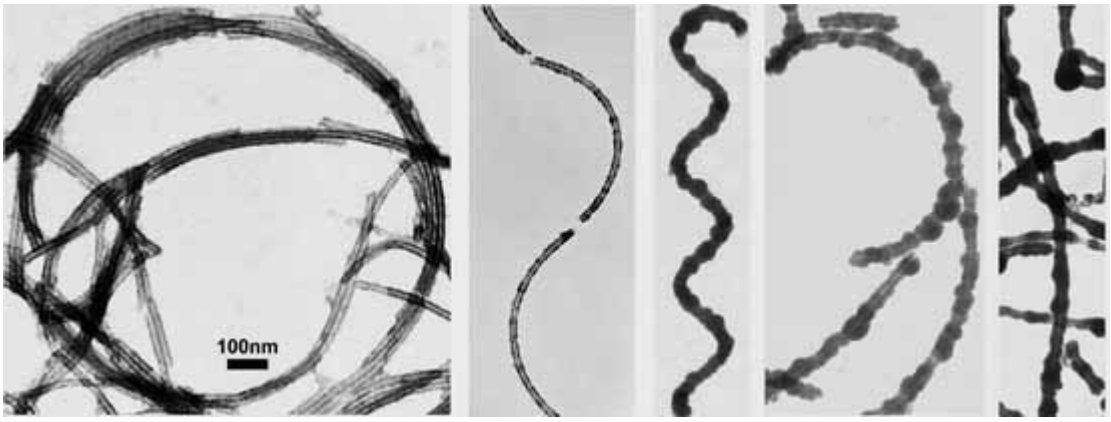


Figure 1.7: Morphology manipulation of flagella templated silica nanotubes synthesized under different pH values.[19] TEM images from left to right correspond to silica nanotubes synthesized under pH of 4, 8, 9, 10.5 and 11 respectively.

1.3.2 Phage templated 1D nanostructures

Bacteriophage is mostly used among all the linear biotemplates. One of the biggest advantages of using phage as template to make linear nanostructures is that peptide sequences binding specifically to a target material can be selected directly through biopanning. A broad types of inorganic materials, including metals, metal oxides, and semiconductors, have been applied as targets for biopanning and a pool of peptides with specific affinity have been established, which confer huge potential on bacteriophages as templates for 1D nanomaterial synthesis.[51, 75-77]

Mao *et al.* reported a pioneer work of synthesizing single-crystal semiconducting nanowires (ZnS and CdS) and ordered magnetic nanowires (CoPt and FePt) based on

genetically engineered M13 phage templates (Fig. 1.8).[77] The peptides displayed on the major coat protein of M13 phage were selected through a screening process from phage library, and were considered to control the composition and phase during NPs nucleation. Taking ZnS as an example, the selected affinity peptide (CNNPMHQNC) was first displayed over the side wall of phages, then ZnS nanocrystals were mineralized onto the virus surface from a metal salt precursor under reduced temperature. After annealing, the polycrystalline assemblies were transformed to single-crystal nanowires with uniform diameter and length (Fig. 1.8a). Similarly, by fusing different nucleating peptides onto M13 phage, CdS, CoPt and FePt nanowires were obtained through either mineralization or chemical reduction (Fig. 1.8b-c). This work represents a universal strategy for the synthesis of 1D nanostructure of various inorganic materials, such as CeO_2, $FePO_4$, Au/Ag alloy, IrO_2, Rh, Ru and Pd, based on the genetically modified phage templates.[41, 43, 60, 78-79]

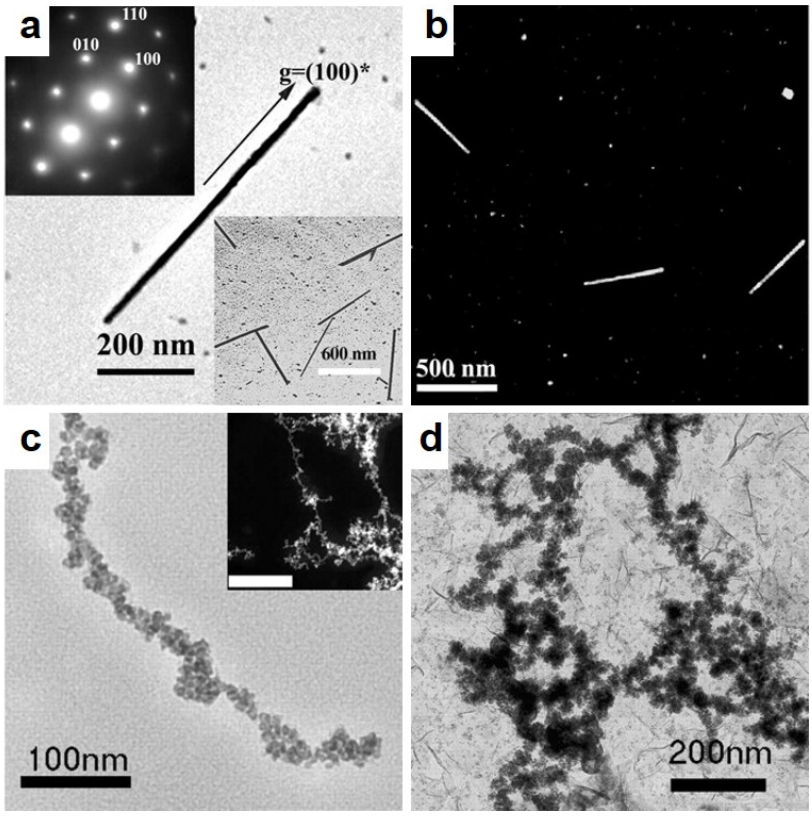


Figure 1.8: TEM images of ZnS, CdS, CoPt and FePt nanowires by using engineered M13 phage as templates.[77] a) Bright-field TEM image of a single ZnS nanowire. Electron diffraction in the inset showed single crystalline pattern. Inset at bottom, low magnification. b) High-angle annular dark-field scanning transmission electron microscopy (HAADF-STEM) image of CdS nanowires. c) CoPt nanowire. Inset, STEM image, scale bar, 100 nm. d) FePt wires.

1.3.3 TMV templated 1D nanostructures

TMV is a plant virus with rod-like appearance. Its capsid is composed of 2130 copies of identical coat proteins and there is a single strand helical RNA in the cavity. The virion is about 300 nm in length, 18 nm and 4 nm in outer and inner diameter respectively. TMV is superior as template for nanomaterial synthesis since it is

extraordinarily stable. TMV is able to withstand high temperature of up to 90 ˚C and a broad pH range from 3.5 to 9 over several hours and its structural integrity is maintained even in some organic solvents, such as ethanol and dimethylsulfoxide (DMSO).[80-81]

So far, a variety of materials were fabricated into linear nanostructures through TMV. Shenton et al synthesized CdS and PdS nanotubes on the external surface of TMV (Fig. 1.9).[26] The dense outer mineral layer and the light internal TMV core of CdS nanotubes were obvious (Fig. 1.9a). Similar results were obtained with PbS nanotubes (Fig. 1.9b). Besides CdS and PbS, Au, Pt, Ag, Pd, Ni, Co, SiO_2 and iron oxides NPs arrays or nanotubes have been organized or synthesized through TMV biological template.[26, 82-83] An interesting phenomenon was observed during the research of this hybrid that TMV virions self-assembled head-to-tail into long nanotubes along the long axis when mineralizing SiO_2 from tetraethoxysilane (TEOS) in acidified solvent (Fig. 1.9c).[26] It is believed that the complemental hydrophobic interactions between two ends of the helical structure give rise to the assembly just like the interactions to assemble protein subunits together into TMV capsid at any cross-section.[84] This highly ordered long fiber structure is not stable but with the coating of inorganic shell or polymer layer it is robust and suitable for further applications.[85]

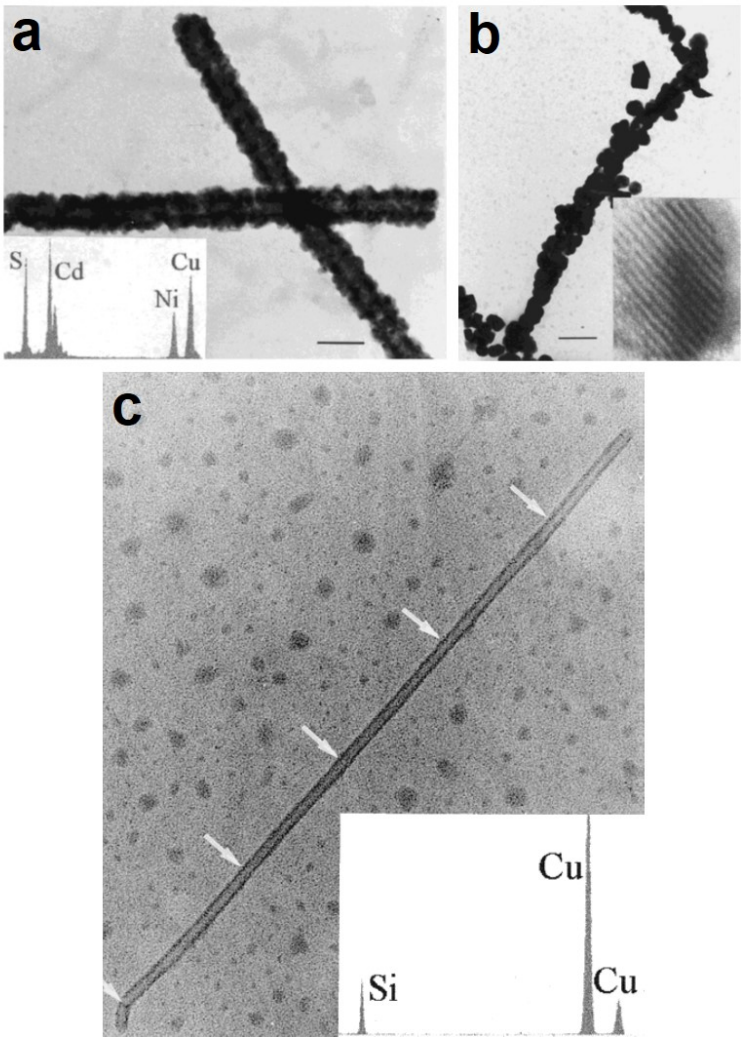


Figure 1.9: TMV templated CdS, PdS and SiO_2 nanowires.[26] a) TEM image of CdS-mineralized TMV. Scale bar, 50 nm. Inset, energy-dispersive X-ray (EDX) spectrum. b) PdS/TMV nanotubes. Scale bar, 50 nm. Inset, high resolution TEM show the crystal lattice of PdS. c) SiO_2 nanotube templated by self-assembled TMV particles. The white arrows show the connecting places of the ends of TMV. Inset, EDX spectrum.

The 4 nm central channel of TMV have also been used as reaction vessel for the growth of nanowires just like the case for 0D protein cage templates. Linear Ag NPs arrays were formed within the channels of the virions.[82] Ni and Co nanowires of about 3

nm in diameter were synthesized selectively in the narrow channel by first activating the TMV with Pd(II) or Pt(II) ions.[86] Then the activated TMVs were metallized by the electroless deposition method in a bath solution containing reductant, and nickel or cobalt ions. The nanowires were about 300 nm long but the ones up to 600 nm were observed which suggested that the end-to-end assembly of TMVs. By changing reaction condition and reductant, the spatial selectivity (exterior or/and interior) of metallization can be achieved.[26, 83, 86] In addition, biometallic alloy nanowires, like CoPt and $FePt_3$, synthesized inside the TMV channel have also been reported.[87]

1.4 Bionanofiber-based higher ordered structures

Fibrous biological templates are capable to assemble into highly ordered 1D, 2D or 3D structures, which are also ideal scaffolds for making inorganic nanomaterial with hierarchical organization. Various strategies have been developed to construct the complex structures from starting building blocks, such as self-assembly at liquid/solid or liquid/liquid interface, evaporation or shearing force induced self-assembly, dip-coating and lay-by-layer method. These strategies greatly rely on the inherent properties of building units including uniform size and shape, exquisite symmetry, modifiable surface chemistry, and liquid crystal structure at high concentration.[84] The assembled hierarchical structures sometimes are directly used as functional nanocomposites, or sometimes undergo the inorganic mineralization for further application.

1.4.1 1D bundles

Inorganic ions are able to trigger self-assembly of bionanofibers into 1D bundles through electrostatic force. Based on this principle, Wang et al used the mineralized hydroxyapatite (HAP)-phage bundles to mimic the lowest level of the bone hierarchical

structure (Fig. 1.10).[88] Fd and M13 virions were chosen as the first building block because their filamentous structure is most like collagen molecules, and with the help of Ca^{2+} they can self-assemble to bundles mimicking collagen fibrils, in which Ca^{2+} ions served as a bridge to cross-link the anionic bacteriophages (calcium ions are expected to coordinate with carboxylic acid residues on the phage surface) (Fig. 1.10 a&b). The formation of Ca^{2+}-phage bundles occurred only at a relatively high concentration of bacteriophages (>5×10^{10} cfu/ml) and calcium ions (>50 mM). The Ca^{2+}-phage complex served as calcium sources and biotemplates to initiate the proper spatial nucleation and growth of the nanocrystalline HAP along the long axis of the phage, and this mimiced the orientation of the HAP mineralization in nature (Fig. 1.10c). The resultant HAP-phage bundles can serve as building blocks to form higher-order structures for bone biomaterial fabrication. He et al found genetically engineered M13 phage can also be used in self-assembly of nanostructure bundles triggered by calcium ions and this method can reduce the Ca^{2+} concentration needed to bridge phage bundles.[89] The M13 phage was genetically modified to display negatively charged peptides E8 (8 Glu) at the major coat protein pVIII and this maked the side wall of M13 phage more anionic. While in this case, cationic calcium ions were able to initiate the electrostatic self-assembly of Ca^{2+}-phage bundles at a much lower concentration (4mM).

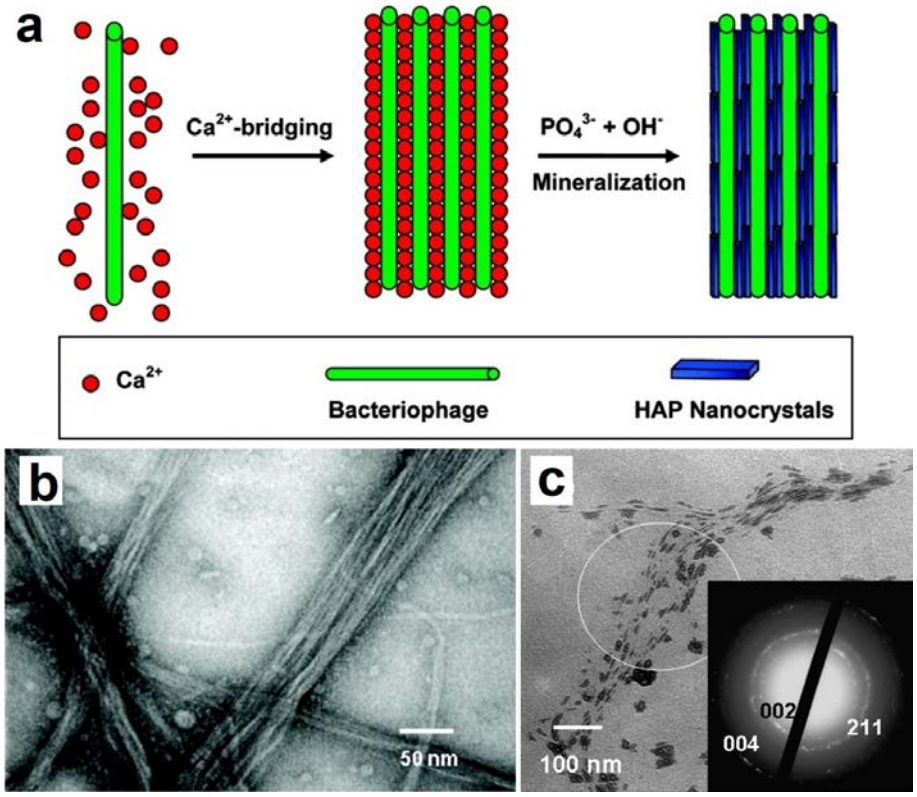


Figure 1.10: Ca^{2+} induced phage bundles.[88] a) Strategy for oriented nucleation and growth of HAP nanocrystals within aligned phage nanofibers. b). TEM image of Ca^{2+}-phage bundles. c). TEM image of HAP-phage bundles.

Moreover, a novel type of mesoporous silica fibers were synthesized using the orderly assembled hexagonal phage bundles as templates.[90] After formation of the inorganic component, the bundled biotemplates were removed by calcination leaving only the mesoporous silica structures. Besides electrostatic interaction, covalent bonds can also be applied for bundle structure formation of bionanofibers. It is reported that the introduction of cysteines on the surface induced self-assembly of flagella into bundles by formation of disulfide bonds.[91]

1.4.2 2D films

Bionanofibers, with or without other molecules, such as polylysine, can be assembled into 2D films. Without the help of other molecules, phage themselves are capable to assemble into ordered film with specific fiber orientation due to the liquid crystalline property. Chung et al fabricated a type of RGD-phage film by a simple horizontal shearing method for neural cell growth.[92] In this kind of film, phage bundles parallel to the shearing direction were observed and showed nematic liquid crystalline pattern. Besides, they also discovered a vertical shearing method to build up phage films by pulling substrate from chiral colloidal M13 solution.[93] The created structures, including nematic orthogonal twists, cholesteric helical ribbons and smectic helicolidal nanofilaments, had multiple levels of hierarchical order, and the delicate structure can be controlled by varying phage concentration, pulling speed, phage and substrate surface properties.

Similar phage films could be achieved through a layer-by-layer strategy with the help of positive molecules. Generally, the thin films are fabricated by depositing positively charged molecule layers and negatively charged phage particle layers alternately. Zhu et al found that assisted by positive polylysine as a cross-linker, both wild type and engineered phages can form ultrathin films through this method.[94] Under an optical microscope and scan electron microscope (SEM), the phage films were composed of parallel phage bundles separated by grooves and the bundles were larger in magnitude when higher phage concentration was used (Fig. 1.11). In addition to phage films, flagella films could also be achieved through this layer-by-layer method

using a polymer, polyethyleneimine (PEI), as the positive layer.[95] The mineralization of $CaCO_3$ on this film was also demonstrated.

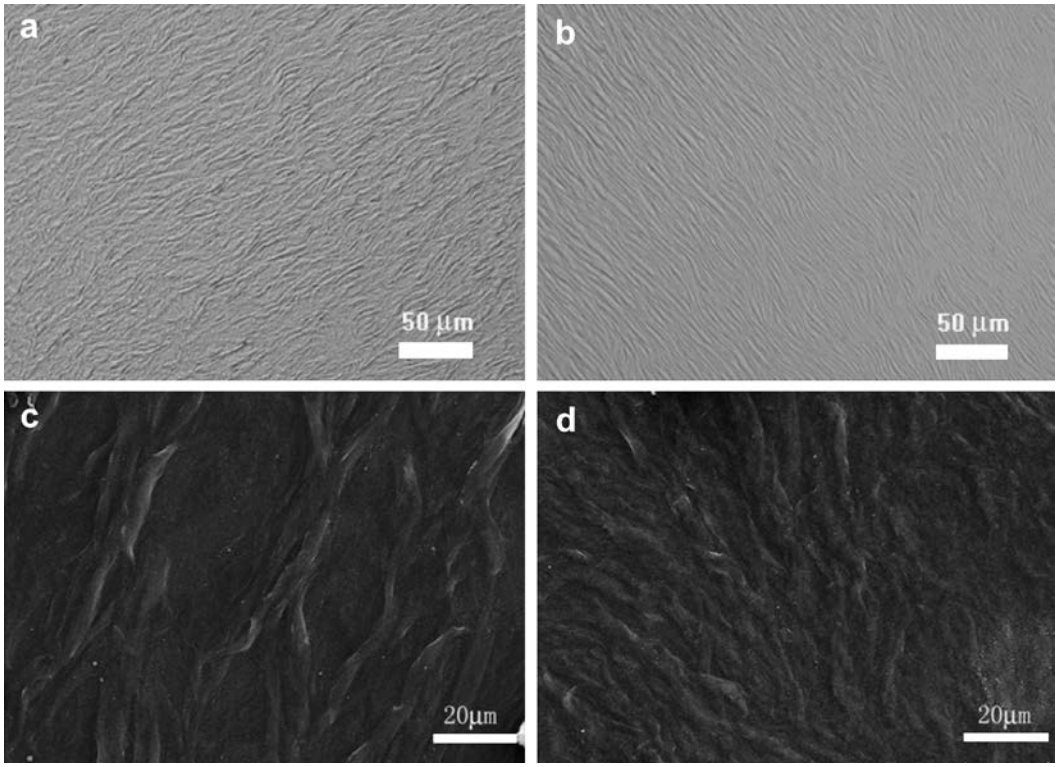


Figure 1.11: Phage films fabricated through layer-by-layer method.[94] Bright field (a, b) and SEM (c, d) images of M13 phage films assembled from the concentrations of phage at 10^{12} pfu/ml (b, d) and 10^{14} pfu/ml (a, c). Phage films were composed of parallel phage bundles separated by grooves.

Recently, it is found that magnetic guidance can assist the formation of highly ordered bionanofiber films.[96] First the magnetic NPs (MNPs) were assembled on the biotemplates such as phages, flagella or bacterial pili, and simply drop-cast on a substrate which was in a strong magnetic field. With this magnetically guided deposition method, MNP-biofibers could be fabricated into various structures including

single-orientation horizontally aligned 2D nanofiber arrays, multi-orientation multilayered 2D films and vertically aligned 3D structures.

1.4.3 3D bulk materials

Due to the small size and flexibility, bionanofibers are hard to be fabricated into 3D materials without other component. Generally, they work as functional parts and are filled into other self-standing 3D materials, or sometimes form 3D bulk material with the assistance of other components. Wang et al filled phage nanofibers displaying RGD peptides into the pores of 3D printed bioceramic scaffold and endowed the inorganic scaffold with bioactivity which could induce osteogenesis and angiogenesis.[97] To mimic the nature nanofibrous protein network matrices, the mixture suspension of engineered phages with liquid crystalline structure and neural progenitor cells (NPCs) were injected into liquid agarose, finally generating orientationally ordered, 3D phage nanofiber matrices. The formed phage nanofibers in the matrices showed nematic liquid crystalline structure and these biomimetic matrices were able to support NPCs proliferation and differentiation.[98] On the other hand, with the help of other component, biofibers themselves as building blocks can be built up into bulk materials and mostly hydrogel. AuNPs/phage hydrogel was reported.[99] Moreover, by using glutaraldehyde as cross-linker, hydrogels composed of only phage particles or phage/single-walled carbon nanotube (SWNT) could be achieved.[100]

1.5 Applications of biofiber templated nanomaterials and their assemblies

So far, the biofiber templated nanomaterials and their assemblies have been explored for applications such as dye-sensitized solar cell (DSSC), lithium ion battery (LIB), photocatalytic water oxidation, hydrogen production, gas and humidity sensing,

electroconductive films, tumor imaging and tissue engineering.[50, 60-61, 101-105] Most of the researches were based on phage templated nanomaterials.

1.5.1 Energy devices

1-D nanostructures, due to their unique electronic, optical, thermal and mechanical properties, are expected to be applied as both structural and functional units in energy devices, mostly DSSC and LIB.[106]

Dye-sensitized solar cell (DSSC)

DSSC is constructed basing on three important components, photosensitizing dye, semiconductor (generally a porous layer of TiO_2 NPs) and electrolyte solution. The dyes absorb sunlight and produce excited electrons, then the electrons are injected into the semiconductor and percolated to the electron collector. The electrolyte ions transfer electrons back to the dyes to regenerate the photosensitizer. To increase the photovoltaic efficiency, phage fibers were introduced into DSSCs.

Dang exploited genetically engineered M13 which displayed single-walled carbon nanotubes (SWNTs) binding peptides, SPHTELP, as a template to assemble and stablize SWNTs (Fig. 1.12).[53] The achieved M13/SWNT bundles were further be used as templates for biomineralization of heterogeneous TiO_2, forming phage based linear SWNT-TiO_2 core-shell complexes. These composites were incorporated in DSSCs as photoanodes. The results indicated that the incorporation of semiconducting SWNTs could help with the electron percolation, thus increase electron collection efficiency and power conversion efficiency (from 8.3% to 10.6% compared with photoanodes with only TiO_2 nanoparticals). In contrast to other carbon nanotube-TiO_2 materials, phage based SWNT-TiO_2 complexes maintained high electron mobility of SWNTs because no

chemical modification was performed. Moreover, different to general surfactants, an excess of free phages in the environment to stablize SWNTs from aggregation was not required. This is important because the free surfactants may hinder the nucleation of heterogeneous TiO_2 on SWNTs surface. Additionally, calcination removal of phage biotemplates which assembled TiO_2 NPs in DSSCs could also increase the photovoltaic efficiency.[107] The left interconnected hollow nano-channels functioned as pathways for easy electrolyte penetration, which facilitateed the electron diffusion at the interface between TiO_2 and electrolyte.

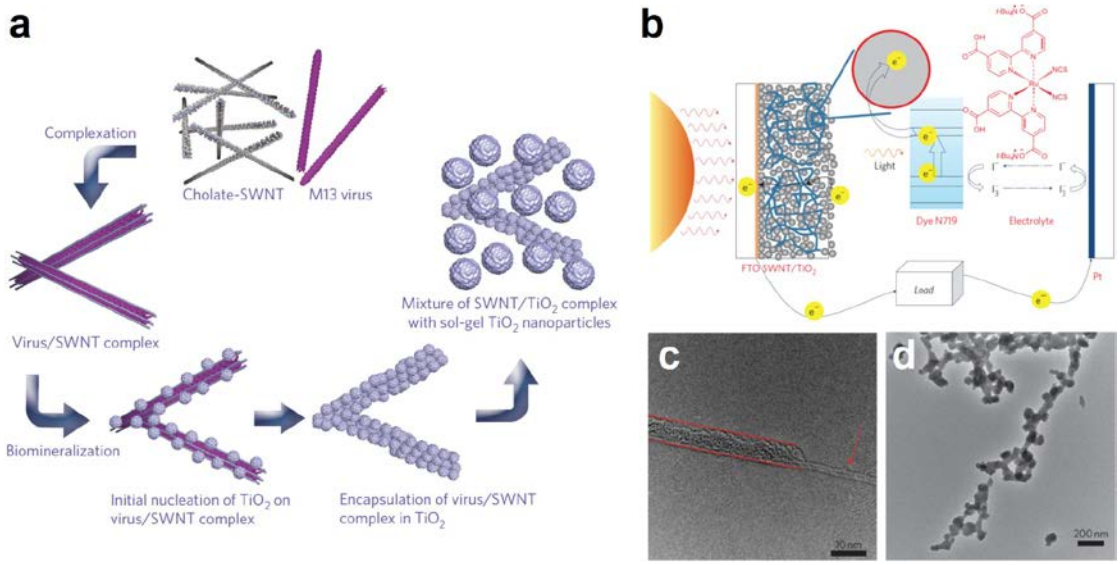


Figure 1.12: TiO_2/SWNTs nanocomposites integrated DSSC.[53] a) Schematic diagram of processing of M13/SWNTs complexation and TiO_2 biomineralization. b) Scheme of dye-sensitized solar cells. c) High resolution TEM image of M13/SWNTs complexes. Viruses are partly burned off. Arrow, SWNTs. Dash line, M13. d) TEM image of TiO_2 crystals on the M13/SWNTs complex.

Lithium ion battery (LIB)

LIBs have been widely used as power sources for portable electric devices including mobile phones, laptops and tablet, digital cameras, etc. The development of new type of LIBs which have higher electrochemical performance and smaller size is always the central issue. Biofiber templated nanomaterials help with this mainly in two ways, increasing the surface area of electrodes which consequently increases the electrode electrolyte interface, or introducing other functional component which can enhance the electronic conductivity.

Inorganic-TMV nanocomposites have been investigated as anode material for LIBs[108-112]. In these studies, TMV were engineered to display a cysteine motif at the N-terminal of each coat protein subunit and after the assembly into virus rod, the cysteines were only surface exposed at one end. The strong covalent interactions between thiol groups on cysteine and metallic atoms enabled the dense, vertical assembly of these virus rods on solid metal substrates (Fig. 1.13a). The virus were then coated subsequently with a thin layer of metal, like Ni, as current collector, and another layer of active anode material, like Si, TiO_2 or V_2O_5, for lithium ion batteries (Fig. 1.13a&b). The 3D virus-based bio-inorganic nanocomposites anode materials have enhanced dramatically the reactive surface area, and consequently the capacity and cycling stability of lithium ion batteries (Fig. 1.13c).

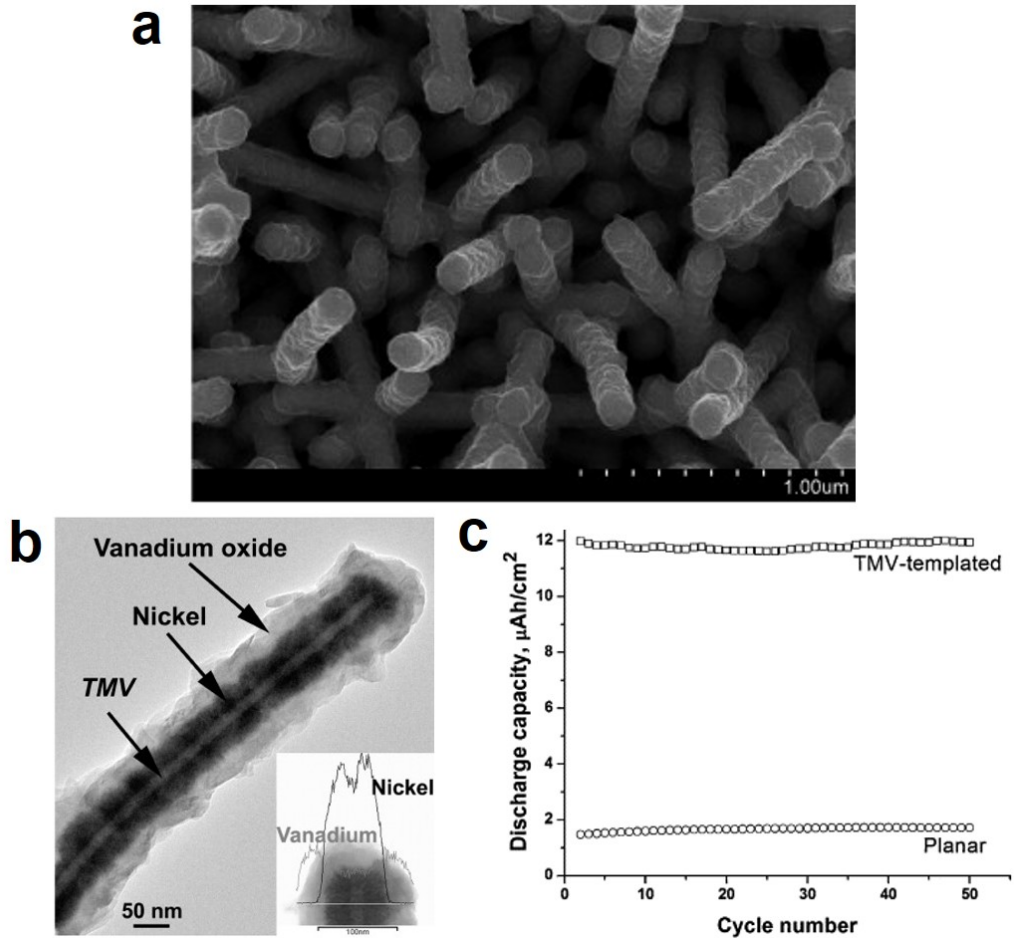


Figure 1.13: LIB anode materials prepared by vertical array of TMV templates.[112] a) SEM image of a vertical array of V_2O_5/Ni/TMV nanorods on Au substrate. b) TEM image of a V_2O_5/Ni/TMV nanowire. Inset, EDX profile shows distribution of V and Ni elements across the nanowire. c) Cycling performance of the cells with or without TMV templated anodes.

Double-display phage system was also introduced to LIBs. In one example, M13 phage major coating protein pVIII was genetically modified with cobalt nucleation motif and gold binding motif.[61] As a result, Au and Co_3O_4 nanomaterials can be subsequently deposited onto the phage nanofibers forming the structure that Au

spherical NPs embedded in the solid Co_3O_4 nanowire matrix. When the Au-Co_3O_4 hybrid nanowires were applied as anode material of LIB, they exhibited remarkably higher capacity and much slower capacity degradation through many cycles of charging and discharging. Instead of fusing foreign peptides only onto one type of protein, the major coating protein pVIII and tip protein pIII were also modified as bifunctional templates to form cathode material for LIB [41]. The inserted motif on pVIII is used to help the nucleation and growth of a-$FePO_4$ nanowires, the major functional components of LIB cathode; and the modified pIII can specifically bind to carbon nanotubes (CNTs). The addition of CNTs enhanced the electronic conductivity of the cathode, and thus resulted in a significant increase in the specific capacity of LIB under high discharging rates. In addition, it is also reported that flagella templated iron oxide materials was used as anode in LIB and demonstrated a superior electrochemical performance.[113]

1.5.2 Medical applications

Tumor imaging

Filamentous phages are integrated in tumor imaging as platforms due to two essential reasons. First, through genetic engineering, phages could display various peptides on different coat proteins, which combine multiple functions such as contrast agent binding and tumor targeting. Second, the assembly of many contrast agent NPs together on one biofiber can significantly enhance the imaging signal especially when the number of targets is limited. Based on these principles, MNPs were assembled on the sidewall of M13 phages which displayed triglutamate and a type of targeting peptide which recognize prostate cancer marker, SPARC glycoprotein, was displayed at one end of phages.[105] The fabricated inorganic-biofiber hybrid nanocomposites were

investigated as contrast agents for *in vivo* magnetic resonance imaging (MRI) imaging of prostate cancer. The signal-to-noise ratio was significantly improved which was induced not only from the targeting, but also the large number of NPs attached to each target molecule. In addition, a similar phage system was reported to image prostate cancer, but instead of MNPs, SWNTs were assembled and stabilized at the sidewall of phages.[104] The photoluminescence of SWNTs enabled the second near-infrared (NIR) window fluorescence imaging which permits the detection of tumors in deep and hard-to-detect areas.

Tissue engineering

Tissue engineering is to fabricate functional tissues by combining the usage of scaffolds, cells and biologically active molecules, which can repair or replace part of or entire damage tissues such as bone, cartilage, neural system, etc. Bionanofiber (especially bacteriophages) based materials, function in tissue engineering mainly through two meanings, mimicking the structure and composition of natural tissues by biomineralization, and introducing bioactive peptides by genetically modification.

The lowest level of natural bone structure is the parallelly oriented collagen molecules mineralized with HAP nanocrystals. To mimic bone structure, M13 virions have been chosen as the first building block because their filamentous structure is most like collagen molecules, and with the help of Ca^{2+} they can self-assemble to bundles mimicking collagen fibrils.[88-89] The Ca^{2+}-phage complex served as calcium sources and biotemplates to initiate the proper spatial nucleation and growth of the nanocrystalline HAP along the long axis of the phage, and this mimicked the orientation of the HAP

mineralization in nature. The resultant HAP assemblies are potential scaffold materials for bone regeneration.

For bone engineering, the differentiation of seeded stem cells to osteoblasts is important for successful bone regeneration. Phages can introduce bioactive factors, such as differentiation inducing peptides, by filling the pores of inorganic 3D scaffold.[97] In addition, phages can self-assembled into 2D films with groove/ridge structures, which provide both topographical and biochemical factors to direct stem cell fate.[94] The morphology and orientation of mesenchymal stem cells (MSCs) growing on the film was changed. Cells were highly stretched and aligned along the phage bundles. This geometric characteristic of phage film surface, together with the displayed osteogenic peptides, could induce MSCs differentiation to osteoblast. Moreover, by displaying peptides which promote neural cell adhesion and neurite extension, phage based matrices were able to support neural progenitor cells (NPCs) proliferation and differentiation, which is essential for neural regeneration.[98]

Chapter 2: Tuning Electrostatic Nanoparticle Assembly on Filamentous Protein-based Biotemplates without the Need of Biotemplate Modification

2.1 Introduction

One dimensional (1D) organic and inorganic nanomaterials can find many applications including sensors, optical waveguides, and electronic devices.[114-118] Biotemplated assembly of preformed nanomaterials is a promising approach to such materials. Protein-based 1D nanostructures, such as filamentous bacteriophages (phages),[41, 47, 61, 77, 89, 119-120] bacterial flagella and pili,[67, 113, 121] and tobacco mosaic viruses (TMV)[82, 122-124] are used frequently as biotemplates to achieve this goal. Previously, it is widely believed that genetic engineering or chemical modification of these 1D bio-nanostructures is more desired in order to allow them to template nanomaterials assembly in a controlled manner. In the genetic engineering approaches, the capsid proteins of the biotemplates are modified by genetic means to display foreign peptides (or proteins) in the solvent-exposed domain. In order to achieve materials-specific NPs assembly on the biotemplates such as phages, the materials-specific foreign peptides are normally selected by evolutionary approaches, such as biopanning,[41, 47, 61, 77, 89, 119-120, 125-127] or sometimes by special designs.[67, 82, 113, 122-123] In the chemical modification, click chemistry or other bioconjugation chemistry has been used to conjugate peptides or polymers onto the biotemplates in order to achieve controlled materials synthesis.[128-130] Both the genetic engineering and chemical modification approach have been demonstrated highly effective in the fabrication of uniform 1D nanostructures of many different materials; however, both of them require

high experimental skills, more chemical and/or biological reagents, and intensive labor to produce engineered biotemplates. Moreover, for each type of material, generally a different type of peptides or surface functional molecules has to be displayed or chemically modified onto the biotemplates. Thus, they are neither cost-effective nor easy to reproduce.

Here in this work, we report a novel electrostatic interaction based strategy to assemble pre-synthesized NPs onto protein-based biotemplates to form 1D inorganic nanostructures. This strategy involves no genetic or chemical modification of the biotemplates, but simply uses the wild type versions to achieve NPs assembly, significantly simplifying the process. The electrostatic interaction was created between the highly positively charged branched polyethyleneimine (PEI) coated NPs and the naturally negatively charged biotemplates such as bacterial flagella and pili and filamentous phages (Fig. 2.1). Bacterial flagella (with an outer diameter of ~14 nm and an inner diameter of ~2 nm as well as a tunable length) and pili (~6 nm wide and 1-2 μm long) are protein nanotubes and nanowires collected from the surface of bacteria cells, respectively, while filamentous phages are bacteria-specific protein-terminated virus nanofibers (~900 nm long and 7 nm wide) secreted by bacteria. We found that dense assembly of NPs onto these protein-based biotemplates only took place by using small M.W. PEI (s-PEI) and within a proper pH range. The NPs assembly through this approach is highly tunable in both the size and the assembling density of NPs. More importantly, the electrostatic based assembly can be applied universally to different types of NPs and biotemplates, thus it's a simple and general approach for biotemplated 1D NPs assembly. Although electrostatic interaction has been employed universally to

assemble NPs onto polymeric or inorganic substrates, such as nanowires,[131-132] nanosheets,[133-134] nano/micro-spheres,[135] it is much more challenging to apply such an interaction onto protein-based biotemplates, due to the mixed presence of positively charged, negatively charged, non-charged and even hydrophobic functional groups on the biotemplates surface, which is highly unfavored for the charge-based electrostatic interaction. The work demonstrated here will be the first example of using electrostatic interaction to achieve high-density assembly of inorganic NPs onto protein-based biotemplates.

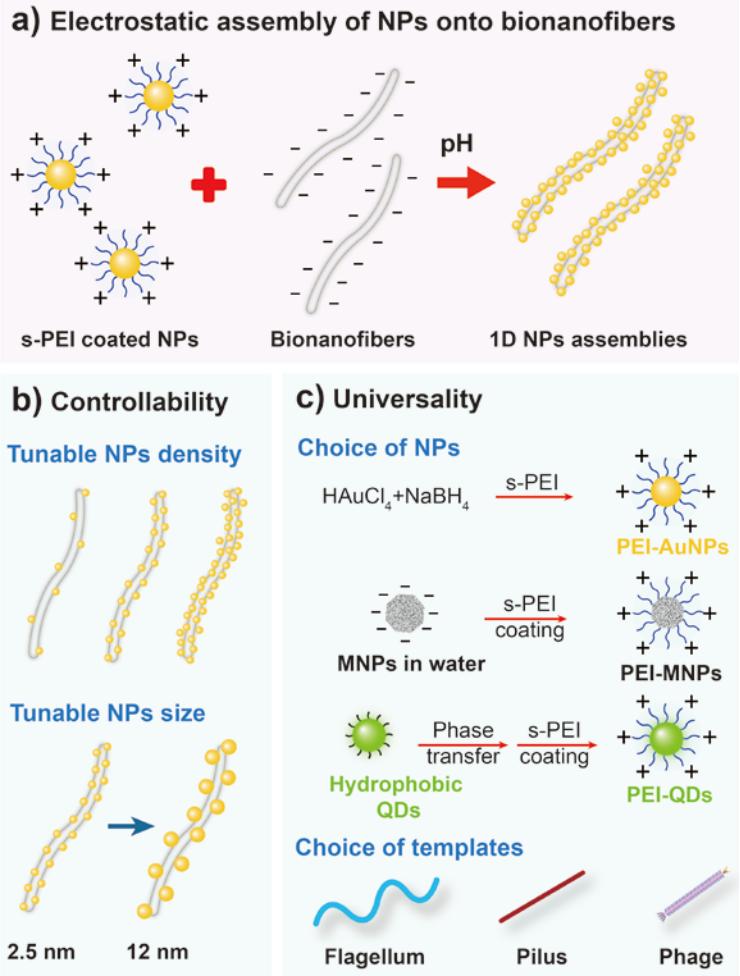


Figure 2.1: Sketch of the s-PEI enabled electrostatic assembly of NPs, including gold NPs (AuNPs), magnetic NPs (MNPs) and quantum dots (QDs) onto filamentous biotemplates (bacteria flagella and pili, and filamentous phages) and the advantages of the method. a) Under proper pH, the s-PEI coated NPs can form dense assembly along the biotemplates through electrostatic interaction; b) Such an approach is highly controllable and assembly of NPs at different densities and of different sizes can be achieved; c) This method can be extended as a universal method to assemble NPs prepared by different methods onto different biotemplates. s-PEI coated AuNPs, aqueous-prepared MNPs and oil-prepared QDs were all demonstrated to be able to assemble onto different biotemplates including flagella, pili and phages.

2.2 Materials and Experiments

2.2.1 Materials

Polyethyleneimine (PEI, M.W. 1200, 1800 and 10000), sodium borohydride, Gold (III) chloride trihydrate ($HAuCl_4 \cdot 3H_2O$), ferric chloride, ferrous chloride, nitric acid, ammonium hydroxide, 1,2,3,4-tetrahydronaphthalene (tetralin), oleylamine (OAm), oleic acid, 3-mercaptopropionic acid (MPA) and reagents used for CdSe/ZnS QDs synthesis and phase transfer were all purchased from Sigma-Aldrich and used as received.

2.2.2 Flagella amplification and purification

Wild type *Salmonella Typhimurium* were cultured in LB medium at 37 °C. The cells were collected by centrifugation at OD around 0.8 and redispersed into a small volume of phosphate buffered saline (PBS) buffer of pH 7.5. Flagella were then detached from the body of bacteria by vortexing and purified by polyethylene glycol (PEG, MW 8000)/NaCl (16.7%/3.3M) precipitation (Fig. 2.2). The purified flagella collected by centrifugation were dissolved in deionized (DI) water. The concentration of flagella was determined by UV absorption at 280 nm.

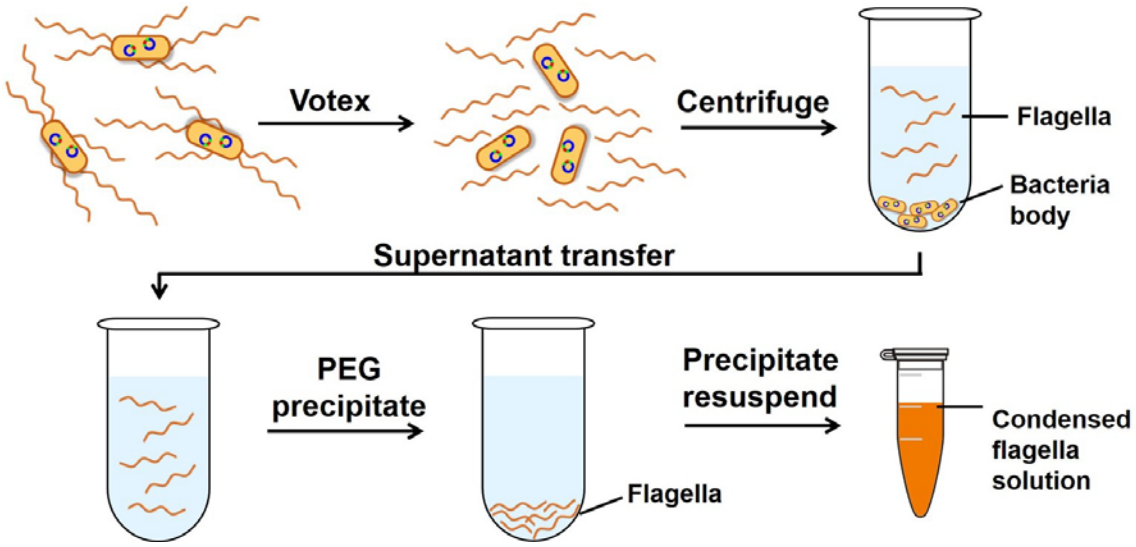


Figure 2.2: Illustration of flagella purification from bacteria.

2.2.3 Phage amplification and purification

Wild type M13 phages were amplified by co-culture with *E. Coli* ER2738 overnight at 37 °C. The phages were first separated from *E. Coli* by centrifugation at 8200 g for 50 min. Then the phages in the supernatant were purified by double PEG/NaCl precipitation and finally dissolved in DI H_2O. The concentration of the phage nanofibers was determined by measuring their absorption at 269 nm.[88]

2.2.4 Synthesis of PEI coated AuNPs directly in water

In a standard trial, to a mixed solution containing 750 µl of 12 mM $HAuCl_4 \cdot 3H_2O$, 10 µl of 15 wt% branched PEI (MW 1800) and 4.25 ml of DI water, 300 µl of 10 mM freshly made $NaBH_4$ solution was added dropwise. The resultant solution was stirred for another 5 min to obtain PEI coated AuNPs. To study the effect of PEI chain length on the NPs assembly, PEI of different molecular weights (MWs), i.e. 1200 and 10000, but of the same mass concentration, was also used to synthesize AuNPs. The pH of the obtained AuNPs solution was adjusted to 5.5 by 10 mM NaOH for further use.

2.2.5 Synthesis of AuNPs in oil phase for study of size effect on the biotemplated assembly

AuNPs of different sizes, i.e. 2.5 nm, 7 nm and 12 nm, were synthesized in the oil phase, which allows better control over the particle size. The 2.5 nm AuNPs were synthesized following a published method.[136] Briefly, the precursor solution composed of 25 mg $HAuCl_4 \cdot 3H_2O$, 2.5 ml tetralin and 2.5 ml OAm was magnetically stirred for 10 min under 40 ˚C. Then, 0.5 ml of reducing solution, which was freshly prepared by mixing 130 mg t-butylamine-borane (TBAB), 3 ml tetralin and 3 ml OAm, was injected into the precursor solution. The reaction was maintained for another 1 h at 40 ˚C after the injection of the reducing solution. These small AuNPs were used as seeds for preparing AuNPs of larger size. To obtain 7 nm AuNPs, 33.4 µl of the seed solution was added to 5 ml of OAm, then a total of 168 µl of 60 mM $HAuCl_4 \cdot 3H_2O$ in ethanol was added evenly in 3 times (56 µl of $HAuCl_4$/time), each followed by stirring and heating at 90 ˚C for 1 h. To form 12 nm AuNPs, 1 ml of the above-prepared 7 nm AuNPs solution was mixed with 5 ml of OAm, and a total of 128 µl of 60 mM $HAuCl_4 \cdot 3H_2O$ in ethanol was added evenly in 4 times (32 µl of $HAuCl_4$/time), each followed by stirring and heating at 90 ˚C for 1 h. The AuNPs of different sizes were washed with ethanol for two times and finally dissolved in tetrahydrofuran. To transfer the as-prepared AuNPs into water, 1 ml of AuNPs solution was mixed with 6 µl of a mixed solution, composed of 500 µl MPA, 1 g tetramethylammonium hydroxide (TMAH) and 4 ml methanol. After 30 min, the supernatant was removed by centrifugation and the pellet was redispersed readily into 1 ml water.

2.2.6 Synthesis of magnetic NPs (MNPs)

To synthesize iron oxide NPs, under vigorous stirring, 4 ml of 1 M aqueous ferric chloride solution and 1 ml of 2 M aqueous ferrous chloride solution were mixed with 50 ml of 0.7 M NH_4OH solution. The stirring was continued for about 5 min, and then the product was centrifuged (3,000 rpm, 10 min). The pellet containing MNPs was redispersed into 2 M nitric acid. Afterwards, the NPs were centrifuged down again at 3,000 rpm for 10 min and resuspended into 10 ml water.

2.2.7 Synthesis and phase transfer of CdSe/ZnS quantum dots (QDs)

The synthesis of CdSe/ZnS QDs was conducted following exactly the reported method.[137] The as-synthesized hydrophobic CdSe/ZnS QDs were transferred into the water by using deprotonated MPA, thus rendering the QDs negatively charged in water.

2.2.8 PEI coating of AuNPs, MNPs and QDs

An optimized amount of 1 wt% PEI (MW 1800) solution, which was previously adjusted to pH 5.5, was added to 1 ml of AuNPs, MNPs or QDs in the aqueous phase. The mixtures were first sonicated for 30 seconds and then stirred overnight during which the surface of NPs would be coated by PEI.

2.2.9 Assembly of NPs onto biotemplates

In a standard assembly process, 300 μl of 150 μg/ml flagella in water was added to 1 ml of AuNPs, MNPs or QDs solutions at pH 5.5. The mixture was then incubated on a rocker shaker for 30 min, followed by a low-speed centrifugation (2000 g). Then the resultant pellet containing AuNPs-flagealla complexes was collected and resuspended into DI H_2O. To study the effect of AuNPs and flagella ratio on the assembly pattern, flagella solutions of different concentrations, including 1000, 500,

150, 50, 25 and 12.5 μg/ml, were used, and the assembly was done following the same protocols.

In the case of using filamentous phages as biotemplates, 5×10^{11} M13 phages were added to 1 ml of the AuNPs or MNPs solution. After incubation for 30 min, the resultant NPs-phage complexes were collected by centrifugation and then redispersed into DI H_2O.

2.2.10 Construction of engineered flagella displaying foreign peptides

The peptides insertion into flagellin were conducted by modifying the DNA responsible for the flagellin expression. Detailed procedures can be found in our published paper.[19-20] Briefly, the pairs of single stranded oligonucleotides, which encode foreign peptides, were synthesized with 5' end phosphorylated (Life Technologies). The pair of single strand oligonucleotides for each peptide was complementary and formed double strand DNA fragment with Xho I and Bgl II sticky ends at 5' end and 3' end after annealing (Fig. 2.3). The primers sequences are summarized in Table 2.1. The resultant double strand DNA fragments were then inserted into linear plasmid PLS411 which was first treated with Xho I and Bgl II restriction enzymes to form complementary sticky ends to the inserted fragment, and ligated by T4 ligase. PLS411 is an expression vector containing flagellin gene with a multi-cloning site in the central region corresponding to the highly variable D3 domain of flagellin. The right insertion of foreign peptides in plasmid was confirmed by sequencing.

Table 2.1: Oligonucleotide sequences of peptides displayed on flagella.

Name	Sequence of oligonucleotides
G10	5'-GA TCT ggc ggt ggc ggt ggc ggc ggt ggc ggt ggc C-3' 5'-TC GAG gcc acc gcc acc gcc gcc acc gcc acc gcc A-3'
E10	5'-GA TCT gaa gag gaa gag gaa gaa gag gaa gag gaa C-3' 5'-TC GAG ttc ctc ttc ctc ttc ttc ctc ttc ctc ttc A-3'
(EG)5	5'-GA TCT gaa ggt gaa ggc gaa ggt gaa ggc gaa ggt C-3' 5'-TC GAG acc ttc gcc ttc acc ttc gcc ttc acc ttc A-3'
E5G5	5'-GA TCT gaa gag gaa gag gaa ggt ggc ggt ggc ggt ggc C-3' 5'-TC GAG gcc acc gcc acc gcc acc ttc ctc ttc ctc ttc A-3'
(EC)5	5'-GA TCT gaa tgt gag tgc gaa tgt gag tgc gaa tgt C-3' 5'-TC GAG aca ttc gca ctc aca ttc gca ctc aca ttc A-3'
E5C5	5'-GA TCT gaa gag gaa gag gaa tgt tgc tgt tgc tgt C-3' 5'-TC GAG aca gca aca gca aca ttc ctc ttc ctc ttc A-3'

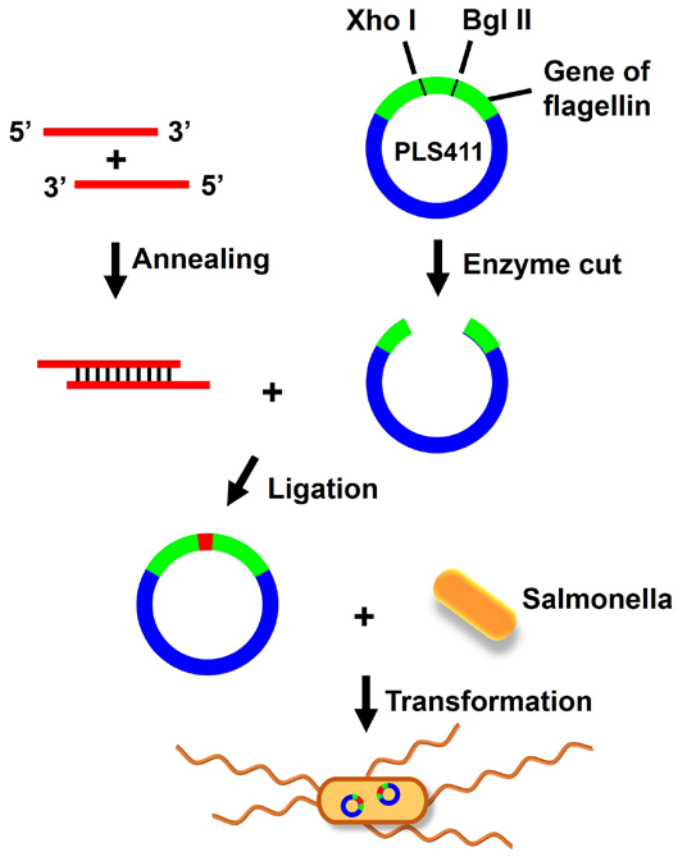


Figure 2.3: Construction of recombinant flagella through genetic engineering.

The recombinant plasmid was then transformed into a competent cell of *Salmonella* SL5928. SL5928 is an attenuated live vaccine strain of *Salmonella* in which the flagellin gene has been inactivated via the transposon insertion, which makes the cell incapable of expressing functional flagella. High flagella-bearing bacteria were selected after three rounds of motility plate experiments. The existence and sequence of plasmid was confirmed by sequencing after each round. The purification of engineered flagella was similar to wild type flagella but with the addition of ampicillin.

2.2.11 Characterization by Transmission Electron Microscopy (TEM)

The assembled NPs-biotemplates complexes were drop casted onto TEM grids for direct TEM observation without negative staining. The purified flagella or phages were negatively stained with 1% (w/v) uranyl acetate (UA) for TEM observation.

2.3 Results and Discussion

2.3.1 Assembly of AuNPs on flagella templates

Due to the fact that most of proteins and their assemblies such as flagella are negatively charged in nature,[22, 138] NPs with positive charges are therefore needed in order to create the electrostatic force. PEI is a hyperbranched polymer and rich in amine groups, thus it is an ideal surface capping agent for the preparation of positively charged NPs. The as-prepared PEI (MW 1800) coated AuNPs are 3-5 nm in diameter (Fig. 2.4a) with a zeta potential of +58 mV. Such a high positive charge ensures that the AuNPs can be stable for more than a month without any apparent change. In most part of the current work, we employed bacterial flagella as a model biotemplate to demonstrate the electrostatic interaction driven NPs assembly. The flagella were detached from a non-engineered subspecies of bacterium *Salmonella*, called *Typhimurium* (Fig. 2.4b) and are

about 14 nm in diameter. In comparison to other types of 1D biotemplates, such as phages and TMV, which are generally less than 1 μm in length, flagella can reach a length of up to 15 μm,[14] thus they are potentially more useful for device fabrication. Engineered flagella have been reported to be used widely as templates for 1D fabrication of many types of inorganic nanomaterials, including Au, Cu, Co, Cd, Pd, SiO_2, TiO_2 and hydroxyapatite (HAP).[19, 21, 69-70, 139] The flagella monomer, flagellin, has an isoelectric point (PI) of 5.3.[19, 140] Thus before conducting the AuNPs assembly, the pH of the AuNPs solution was adjusted to be 5.5 (the value turned to 5.9 after addition of flagella) to ensure that the flagella will be negatively charged during their interaction with AuNPs. Within a few minutes of mixing the flagella and AuNPs, colored fine flocculates were observed in the previously clear solution, suggesting the formation of AuNPs/flagella complex. The flocculates were then collected by low speed centrifugation and examined by TEM (Fig. 2.4). As a result of the AuNPs assembly, the morphology of the flagella has been outlined without negative staining (Fig. 2.4c). Under a higher magnification (Fig. 2.4d), it can be seen that the AuNPs have been assembled very densely on the surface of the flagella, suggesting that the electrostatic force was strong and highly effective to induce the templated NPs assembly.

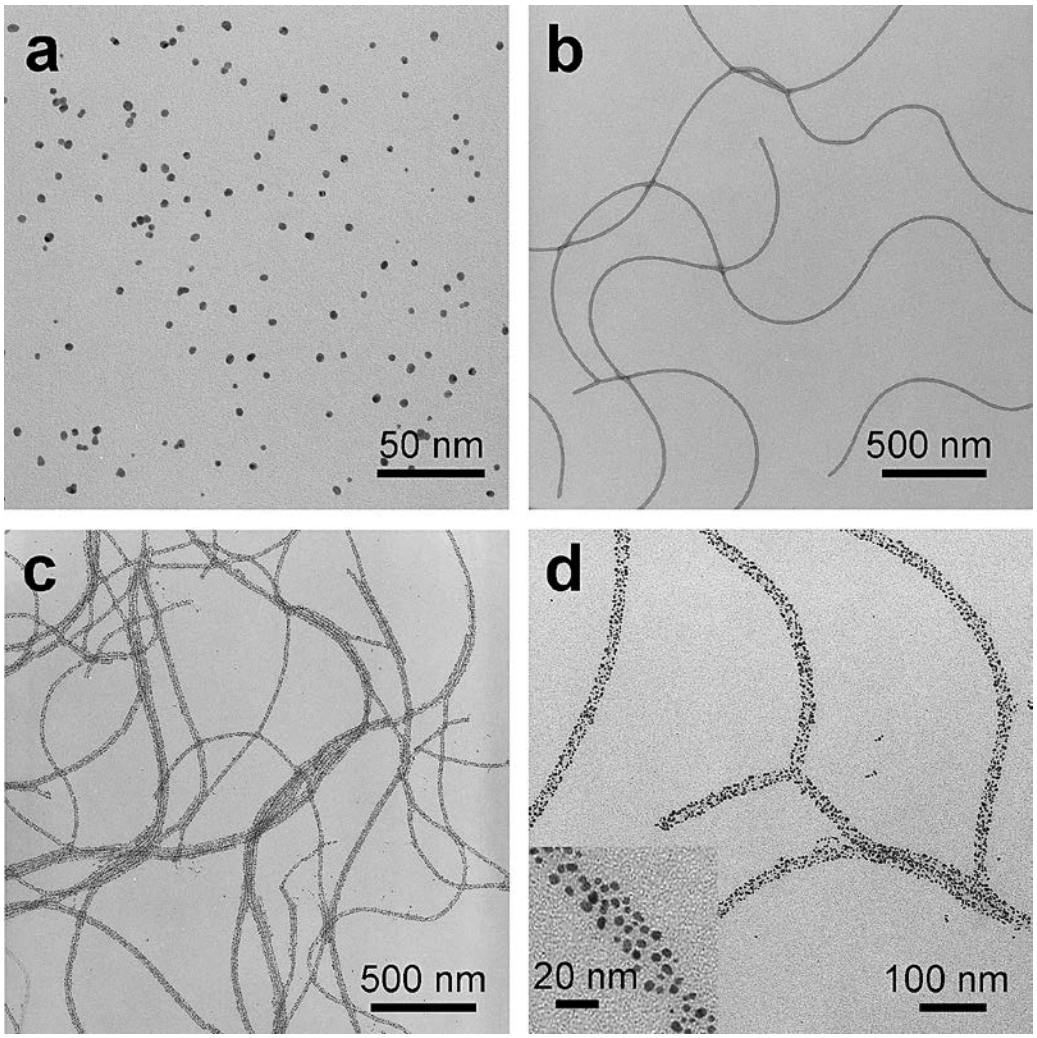


Figure 2.4: TEM images of 1D AuNPs array obtained through flagella templated assembly. a) As-synthesized s-PEI-coated 3-5 nm AuNPs. b) Negatively stained as-purified wild-type flagella nanofibers. The flagella have a diameter of about 14 nm and a length in the range of several up to 15 μm. c, d and inset) Low and high magnification images of AuNPs that have been assembled onto the wild-type flagella templates. No negative staining was applied to the samples.

To further confirm the electrostatic interaction induced assembly mechanism, we first conducted the assembly process in exactly the same manner, but at pH 2.9, at

which both the PEI coated AuNPs and flagella are positively charged. As a result, no pellet could be collected by low speed centrifugation and the AuNPs were hardly seen assembled onto the flagella templates under TEM (Fig. 2.5a&b). On the other hand, in solutions with pH values above the PI of flagellin, such as 5.9, 6.5, 7.4 and 8.5, densely assembled AuNPs-flagella 1D nanostructures that are similar to those shown in Fig. 2.4 can be formed repeatedly (Fig. 2.5c&d). However, when the solution pH values were above 8.5, although the flagella are negatively charged, due to the loss of charges on the PEI coated AuNPs, no 1D templated assembly was observed but all the AuNPs were aggregated (data not shown). Furthermore, we also studied the effect of pH values on the pre-assembled AuNPs-flagella structures. The pellet containing densely assembled AuNPs (Fig. 2.5d, right) was redispersed into a pH 3.0 solution. It was found later that most of the AuNPs were released back into the solution, leaving only a few particles on the templates (Fig. 2.5e&f). All these data provide solid evidence that the strong pH-dependent electrostatic interaction between the AuNPs and the biotemplates, has led to the assembly of these two types of materials into 1D nanostructures.

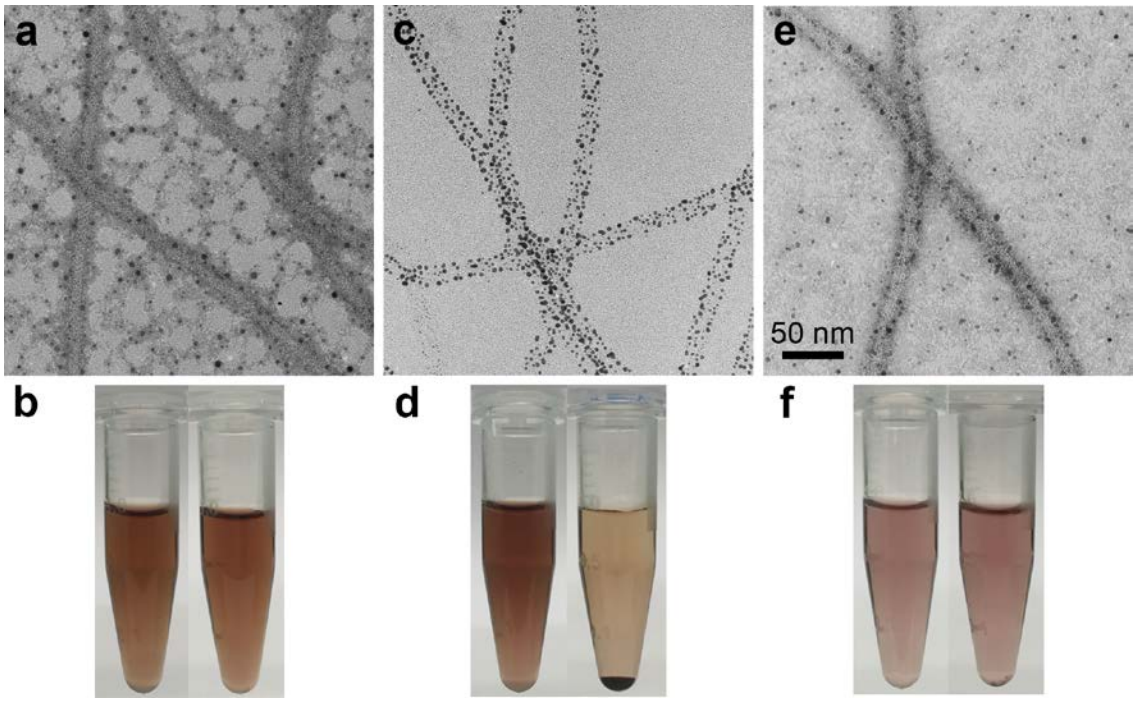


Figure 2.5: Mechanism investigation of AuNPs assembly onto flagella. a) No AuNPs assembly can be seen at pH 2.9, at which both AuNPs and flagella are positively charged. b) A mixed solution of AuNPs and flagella before (left) and after (right) centrifugation, showing that no assemblies could be collected by centrifugation. c) A typical AuNPs-flagella assembly obtained at higher pH values, such as 5.9, 6.5, 7.4 and 8.5. Under these pH values, the AuNPs are positively charged; while flagella are negatively charged. d) a mixed solution of AuNPs and flagella before (left) and after (right) centrifugation, showing that pellets of assemblies could be collected by centrifugation. e) When the pellet of AuNPs-flagella assemblies was re-dispersed back into a pH 3.0 solution, most of the AuNPs were detached from the flagella template. f) a suspension of AuNPs-flagella assemblies in pH 3.0 solution before (left) and after (right) centrifugation, showing that no pellet was formed after centrifugation due to the detachment of AuNPs from the templates. Negative staining was applied to nanofibers in a) & e).

2.3.2 Effect of PEI molecular weight on AuNPs assembly

We then investigated the effect of PEI M.W. on the assembly of AuNPs onto the flagella. PEI of three different M.W., i.e. 1200, 1800 and 10000 Da., was used to synthesize the PEI-coated AuNPs. The synthesis was carried out following the same procedures and the monomer concentrations of PEI (though with different chain lengths) were kept constant. The resultant AuNPs showed no obvious size difference. We then studied the assembly behavior of these AuNPs. It was discovered that the assembly of AuNPs is strongly dependent on the M.W. of PEI, and the smaller M.W. PEI more tended to induce efficient assembly of AuNPs onto flagella templates. AuNPs coated by PEI of 1200 and 1800 Da. formed dense 1D array along the flagella (Fig. 2.6a&b); while with PEI of 10000 Da, there were significantly fewer AuNPs on each flagella nanofiber (Fig. 2.6c). We think that the polymer chain length is the major cause for such a phenomenon. When AuNPs are wrapped by short chain PEI, the overall size of individual NPs is relatively small; however for the long chain PEI coated AuNPs, the polymer ligands are extended remarkably into the solution, which expanded substantially the hydrodynamic size of AuNPs.[141] Because the assembly of AuNPs onto flagella takes place through the charge interaction between PEI and flagella, individual long chain PEI coated AuNPs would occupy significantly more surface area than the short chain PEI coated ones, which resulted in the reduced covering density of the former AuNPs on the flagella templates than the latter ones.

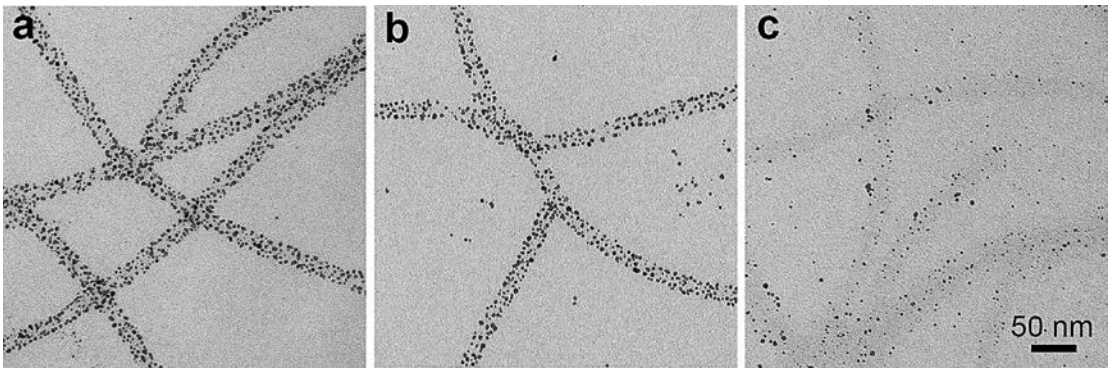


Figure 2.6: Assembly of AuNPs, coated by PEI of different average M.W. a) 1200 Da; b) 1800 Da; c) 10000 Da. Only short chain PEI (1200 Da or 1800 Da) can induce dense assembly of AuNPs on the flagella.

2.3.3 Effect of AuNPs size on the assembly

Because the size of AuNPs (a few nm) is on the same order of magnitude as the diameter of flagella templates (14 nm), we think that the size of AuNPs might have an impact on the pattern of the assembly. For this part of study, we synthesized AuNPs of 2.5, 7 and 12 nm through an oil phase method (Fig. 2.7),[136] followed by phase transfer and PEI coating. The oil phase method provides better control over the size uniformity of the AuNPs. During the assembly process, for all three sizes of AuNPs, the concentration of flagella templates was identical and excess amount of AuNPs was supplied. As shown in Fig. 2.8, AuNPs of all three sizes were organized onto the flagella biotemplates. However, there is apparent difference in the covering density of AuNPs among different sizes. With increasing particles size, the covering density along the biotemplates decreased dramatically. Such a trend is probably the result of the size-dependent strength of interaction between AuNPs and the templates.

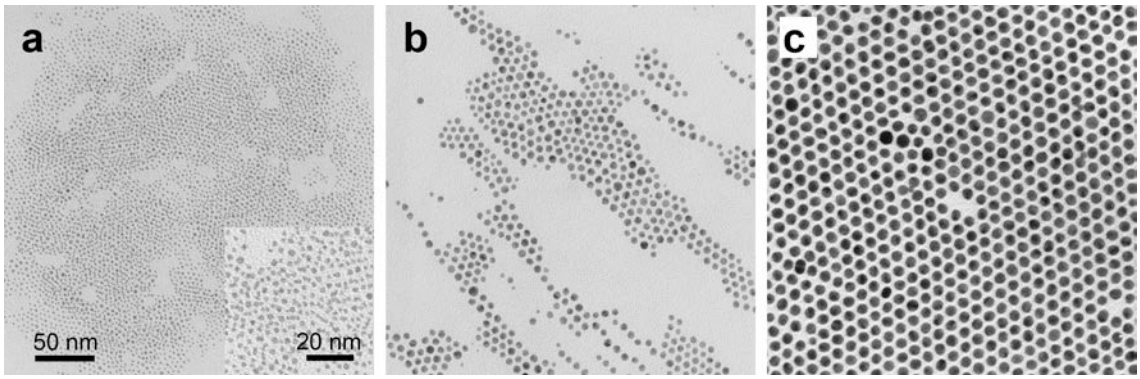


Figure 2.7: AuNPs of different sizes synthesized through an oil phase strategy. a) 2.5 nm; b) 7 nm; c) 12 nm.

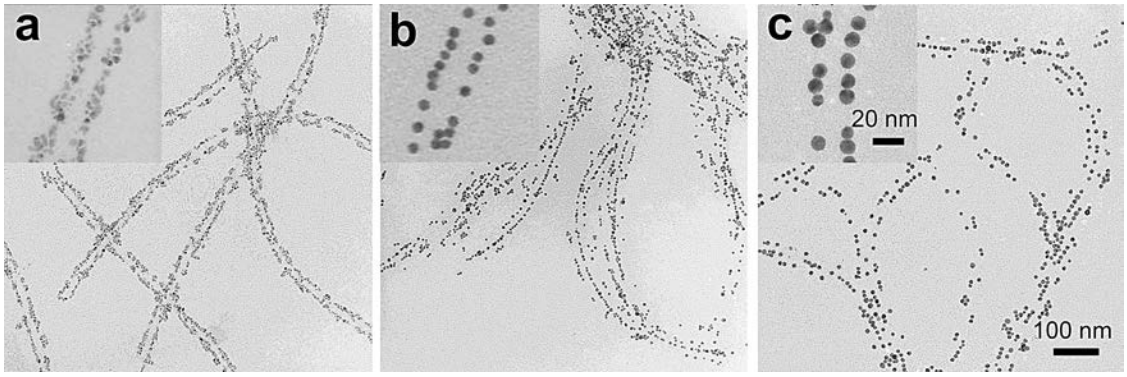


Figure 2.8: Assembly of AuNPs of different diameters onto the flagella templates. a) 2.5 nm; b) 7 nm; c) 12 nm. AuNPs of all sizes can be assembled onto the templates; however, apparent size-dependent assembly density on the templates was observed.

2.3.4 Control over the density of AuNPs on each flagellum template

The density of AuNPs on the nanofibrous biotemplates can be facilely manipulated by changing the ratio between AuNPs and the biotemplates (e.g., flagella). When the amount of AuNPs remained constant, the original concentration of flagella was tuned from 1000 to 12.5 μg/ml. As shown by TEM images of samples prepared from 1000, 500 and 150 μg/ml flagella (Fig. 2.9a, b and c), the average number of

AuNPs on each flagellum template did change correspondingly, although not stoichiometrically, with their relative ratio. However, further increase of the AuNPs/flagella ratio did not lead to higher AuNPs density (Fig. 2.9d), this probably resulted from saturated coverage of the biotemplates surface by the AuNPs at a certain AuNPs/flagella ratio. This can also be seen from the counting of average number of AuNPs on a unit length (200 nm) of the flagella template (Fig. 2.10). The optical properties of AuNPs assemblies were also studied. It is well known that the localized surface plasmon resonance (LSPR) band of AuNPs assemblies is dependent on the inter-particle distance; the closer the NPs are, the more red-shifted the LSPR band will be.[142] Due to the small size and the nonideal monodispersity, the as-synthesized AuNPs showed a relatively broad LSPR band, which made the observation of LSPR band shift upon AuNPs assembly less apparent (Fig. 2.11a). However, the plot of the corresponding LSPR peak wavelength versus the flagella concentration (Fig. 2.11b) showed clearly that the LSPR band of AuNPs did shift gradually from 514 nm to 527 nm along with the reduced supply of flagella. This result is consistent with the fact that the inter-particle distance decreases with increasing assembling density of AuNPs onto flagella, which was more significantly before than after the threshold flagella concentration (150 μg/ml) was reached.

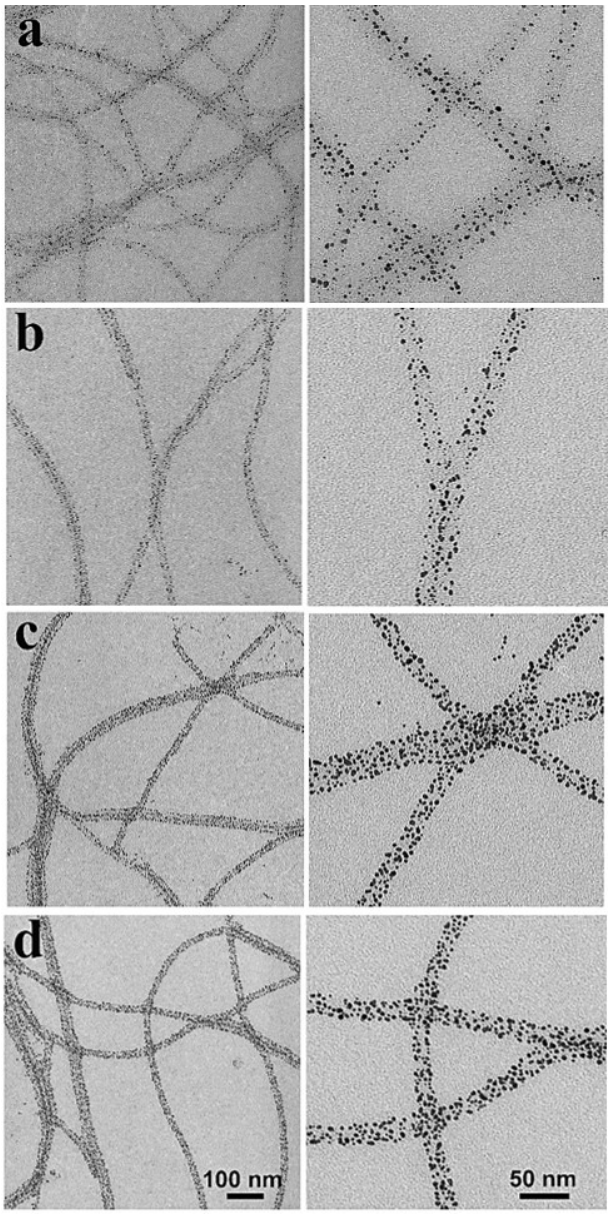


Figure 2.9: Manipulation of AuNPs assembling density on flagella templates. TEM images of AuNPs-flagella assemblies prepared under different AuNPs/flagella ratio at low (left) and high (right) magnification. The amount of AuNPs was kept constant, while the concentration of flagella was a) 1000 μg/ml; b) 500 μg/ml; c) 150 μg/ml; d) 50 μg/ml. The density of AuNPs on flagella gradually increased with decreasing flagella concentration until 150 μg/ml; below this concentration, there was no obvious change on the AuNPs density.

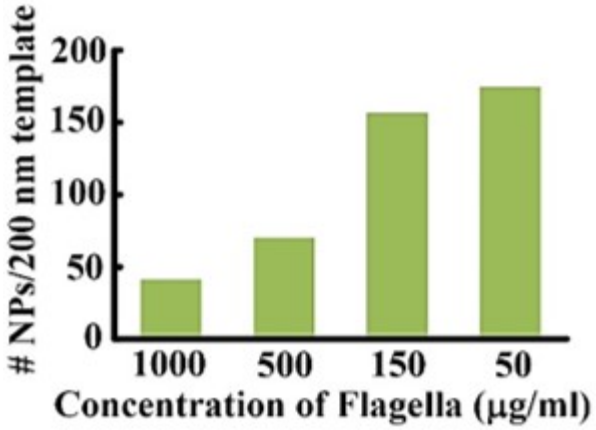


Figure 2.10: Plot of the corresponding AuNPs density on flagella template under different flagella concentrations.

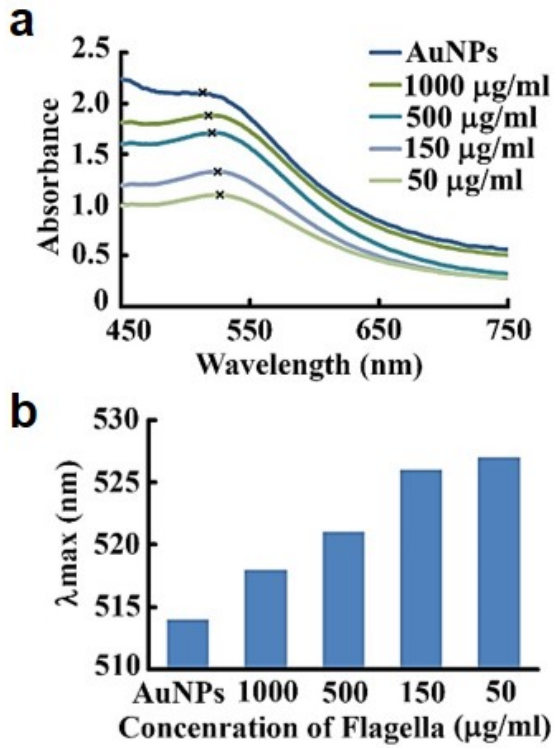


Figure 2.11: Optical property of the AuNPs density on flagella template under different flagella concentrations. a) Absorption spectra of the AuNPs-flagella assemblies. b) Plot of the corresponding LSPR peak maximum versus the flagella concentration.

2.3.5 Assembly of AuNPs on engineered flagella

Although we have successfully tuned the assembly of AuNPs assembly using wild type flagella, the assembly using engineered flagella templates displaying various peptides containing negatively charged residues (glutamate) or/and thiol group bearing residues (cysteine) was also investigated. As shown in Fig. 2.12, the location of displayed foreign peptide on flagellin is on the flagella surface and solvent-exposed. The sequences of displayed peptides are listed in Table 2.2. E10, (EG)5 and E5G5 were designed to introduce more negative charges on the surface of flagella which were expected to allow the assembly of more AuNPs onto an individual flagellum. In addition, effect of the number (E10 vs. E5) and arrangement ((EG)5 vs. E5G5) of negatively charged groups on AuNPs alignment pattern were also considered. Moreover, thiol groups were also introduced onto flagella surface by displaying (EC)5 and E5C5 for some possible covalent bonding between gold and thiol groups. Wild type and G10 flagella were used as negative control for all the other engineered flagella.

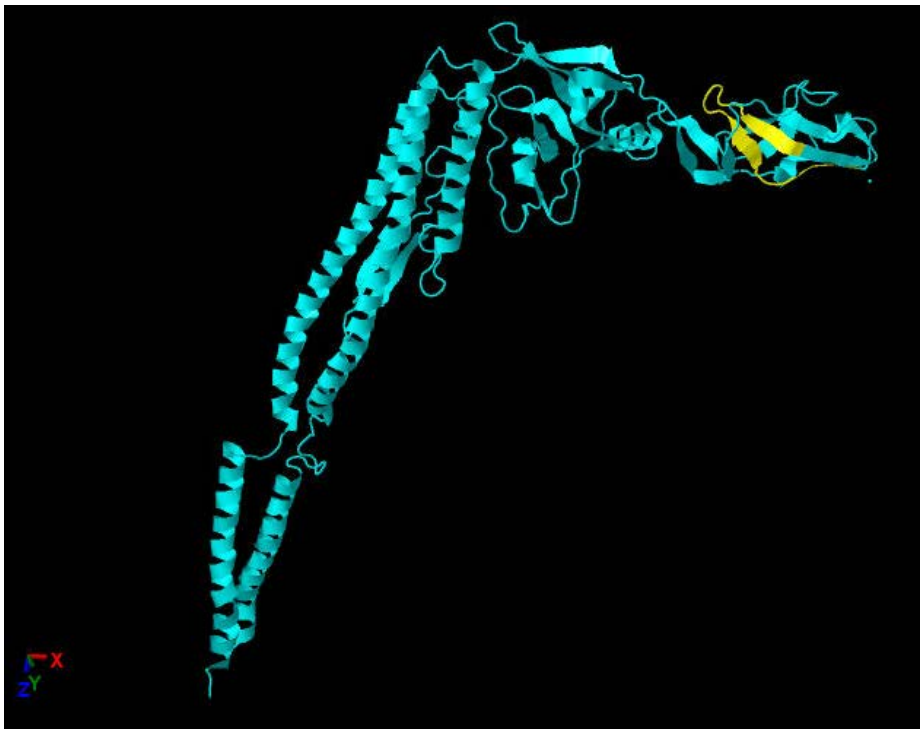


Figure 2.12: Crystal structure of flagellin. Segment in yellow is where the displayed foreign peptide is located. PDB ID is 1UCU.

Table 2.2: Sequences displayed on engineered flagella. G, glycine; E, glutamate; C, cysteine.

Name	Sequence
G10	GGGGGGGGGG
E10	EEEEEEEEEE
(EG)5	EGEGEGEGEG
E5G5	EEEEEGGGGG
(EC)5	ECECECECEC
E5C5	EEEEECCCCC

Zeta potential study was performed to confirm the surface charge change introduced by insertion of foreign peptides. Zeta potentials of all the engineered flagella

containing glutamates are lower than that of the wild type flagella, indicating there are more negative charges on the flagella (Table 2.3). The zeta potential of the G10 flagella was supposed to be the same as that of the wild type flagella, but contradictory result was observed. This may be because that the display of G10 altered the protein structure of flagellin and this structure change increased the surface negative charge.

Table 2.3: Zeta potential of wild type and engineered flagella.

Flagella	Zeta potential (mV)
WT	-22.88
G10	-29.41
E10	-34.74
(EG)5	-30.21
E5G5	-30.42
(EC)5	-27.96
E5C5	-25.72

The assembly was carried out by mixing 300 µl of 25 µg/ml wild type or engineered flagella with 1 ml of AuNPs solution. Such a low flagella concentration was used to ensure that AuNPs are over supplied so as to exclude the impact of inadequate nanoparticles supply on the density of AuNPs on the template. The engineered flagella with different displaying peptides exhibited different capability to assemble AuNPs (Fig. 2.13). Compared to the wild type flagella, the AuNPs density on E10 and G10 flagella were just slightly increased as a result of increased negative charges on their surface; while there was no obvious density difference of AuNPs on (EG)5 and E5G5 flagella. The influence of charge density of template is not apparent on the AuNPs assembly pattern. The possible reason may be that the positive charge density on AuNPs

introduced by PEI is too high, thus they are not sensitive to the weak charge density change on the template. These results indicated that tuning the assembly pattern through tuning the charge density of flagella template is not suitable for the PEI-AuNPs system. For further research, we will synthesize AuNPs using surface ligand with weak positive charges and explore the effect of template charge density on their assembly pattern.

Concerning (EC)5 flagella, the separate fibrous distribution indicated that the cysteines only formed intra-flagellum disulfide bonds but no one between different flagella. The intramolecular disulfide bonds changed the surface chemistry or structure of (EC)5 flagella, which made it not suitable for AuNPs binding. For E5C5 flagella, the additional cysteine-derived thiol residues formed inter-flagella disulfide bonds and induced the self-assembly of bundle structures in which the flagella aligned in parallel. AuNPs were closely packed on these flagella bundles. This large scale hybrid structure indicated the possibility to control the higher order of AuNPs assembly on engineered flagella templates.

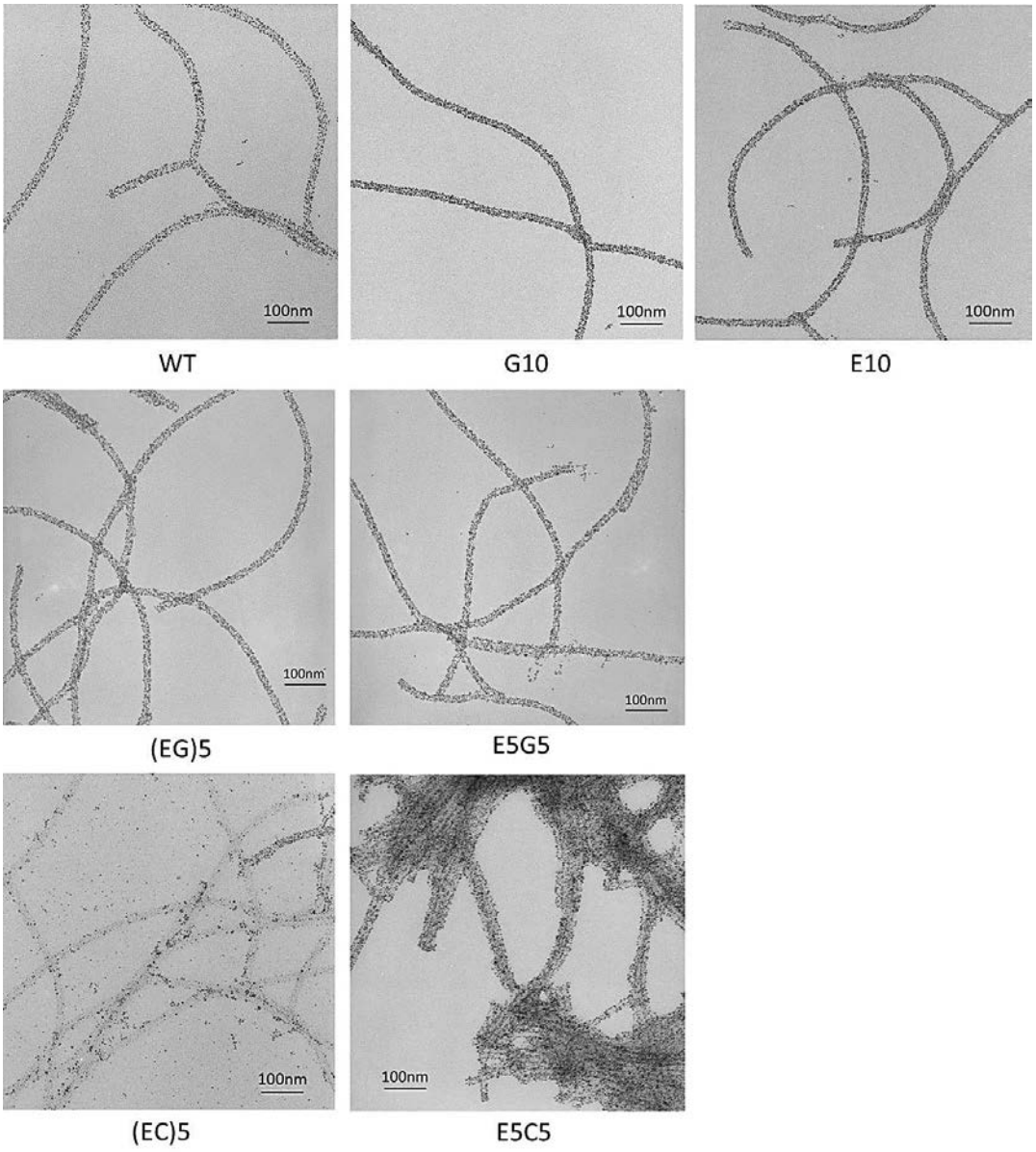


Figure 2.13: AuNPs alignment on wild type and engineered flagella. The density of AuNPs on G10 and E10 flagella was higher than wild type flagella. There was no obvious density difference of AuNPs on (EG)5 and E5G5 flagella compared to wild type flagella. The density of AuNPs decreased dramatically on (EC)5 flagella. For E5C5 flagella, the introduction of additional cysteine-derived thiol residues induced the flagella to form bundled structure by inter-flagella disulfide bonds, thus controlled the higher order of AuNPs assembly.

2.3.6 Generality of the method

The above results have demonstrated clearly the effectiveness of our proposed electrostatic strategy in assembling s-PEI coated AuNPs onto the flagella biotemplates. We believe that such an assembling strategy should be independent of the types of NPs and biotemplates. Namely, any type of s-PEI coated positively charged NPs should be able to assemble onto any type of biotemplates, as long as they are negatively charged. To test this hypothesis, we expanded our assembly strategy to two other types of NPs, namely iron oxide magnetic NPs (MNPs) and quantum dots (QDs), and two other types of linear biotemplates, namely filamentous phages and pili. The MNPs were prepared in the aqueous phase without any surface capping ligands but they can disperse stably in an acidic solution;[143] while the CdSe/ZnS QDs were synthesized in the oil phase followed by a phase transfer process using 3-mercaptopropionic acid (MPA).[137, 144] Both types of NPs were then wrapped by a layer of s-PEI. The s-PEI-coated MNPs and QDs formed stable dispersion in water (Fig. 2.14a&c). Both the MNPs and CdSe/ZnS QDs can be assembled well onto the flagella templates (Fig. 2.14b&d), regardless of the type of materials and their surface ligand structures, as long as there is a PEI layer on the outermost surface. When the biotemplates were changed from flagella to phages (Fig. 2.15a) or pili (Fig. 2.15d), high density assembly of the s-PEI coated AuNPs and MNPs can also be achieved through our electrostatic assembly approach (Fig. 2.15b&c for phages; Fig. 2.15e&f for pili). These results suggest that the method demonstrated here can be employed as a general method for the biotemplated 1D assembly of NPs. This is in dramatic contrast to the conventional genetic engineering based strategy, which demands a unique peptide sequence for each type of materials.

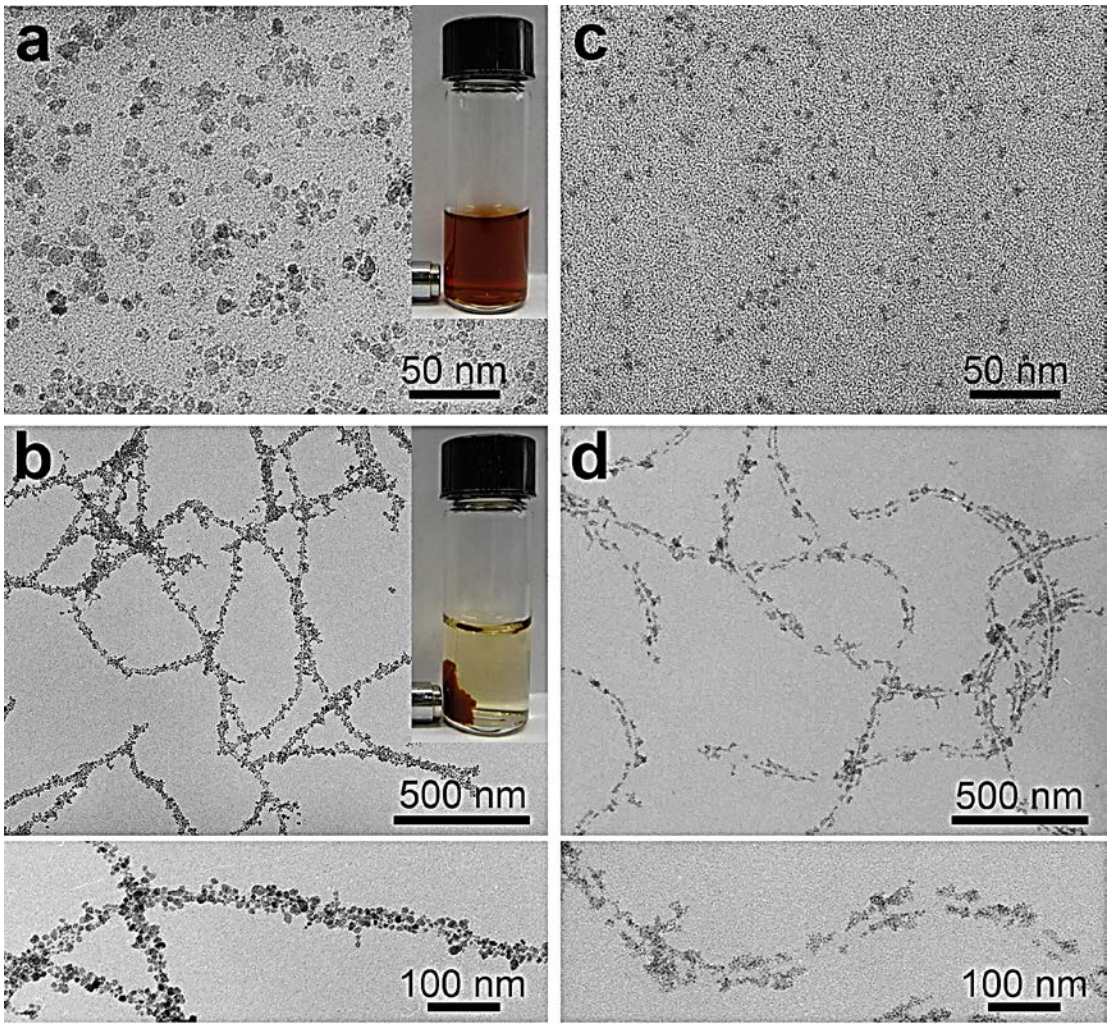


Figure 2.14: Demonstration of generality of the electrostatic assembly method with different NPs (coated by s-PEI) but same biotemplates (flagella). a) TEM image of aqueous-prepared MNPs after s-PEI coating but before being coated on the flagella. b) Low (top) and high (bottom) magnification images of 1D assembly of MNPs onto the flagella. Insets: Response of MNPs to a magnet before (a) and after (b) being assembled on the flagella. c) TEM image of oil-prepared QDs after phase transfer and s-PEI coating but before being assembled on the flagella. d) Low (top) and high (bottom) magnification images of 1D assembly of QDs onto the flagella.

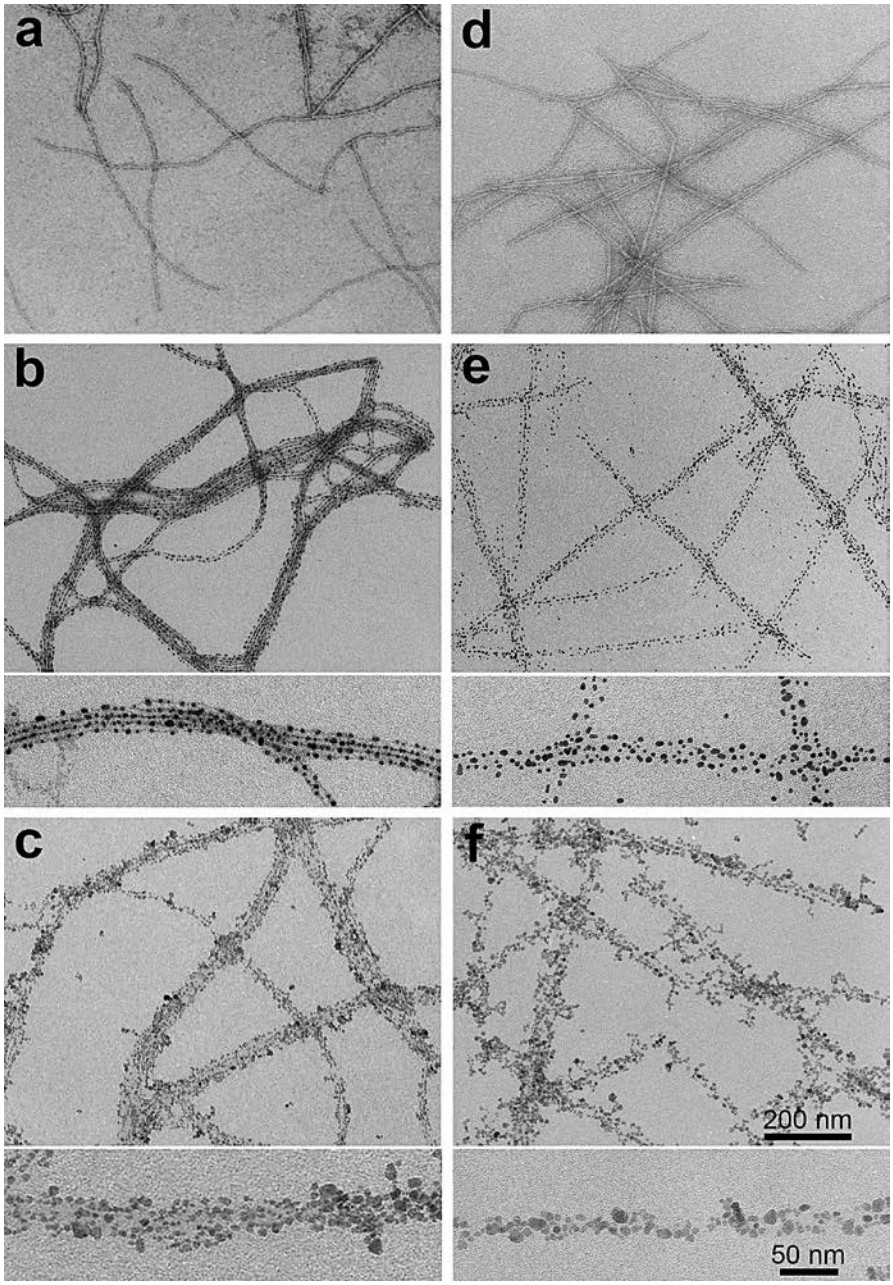


Figure 2.15: Demonstration of generality of the electrostatic method with the same s-PEI coated NPs but other biotemplates (pili and filamentous phages) different from the flagella. a) and d) Representative TEM images of the negatively stained phages (a) and pili (d) biotemplates. b) AuNPs-phage assemblies; c) MNPs-phage assemblies; e) AuNPs-pili assemblies; f) MNPs-pili assemblies. b, c, e, f) Top, low magnification; bottom, high magnification.

2.4 Conclusion

In summary, we have developed an electrostatic assembly strategy to fabricate 1D inorganic-biological hybrid nanostructures by using natural protein-based bionanostructures as biotemplates. Our method does not require either the genetic engineering or chemical modification of the biotemplates, thus it significantly simplifies the fabrication process. The key is to harness the negatively charged nature of wild-type biotemplates while simply using them to template the assembly of s-PEI coated NPs. The simple electrostatic interaction between the negative charges of the biotemplates and positive charges of the s-PEI coating (on the NPs surface) has allowed us to form a variety of inorganic-biological hybrid nanostructures, in a "plug-and-play" format, by independently changing the biotemplates or NPs. We discovered that proper pH and s-PEI are the two key factors to achieve dense 1D assembly of NPs on the biotemplates. We demonstrated that our new method can be indeed used to assemble NPs of different sizes and with controlled density. We also proved that our method can assemble multiple types of NPs onto different types of templates, such as flagella, pili and phages. The flagella, pili and phages are three different examples of biotemplates and the NPs used are typical examples of different synthetic systems, i.e. AuNPs were directly prepared with s-PEI coating surface, MNPs were prepared in aqueous phase first followed by s-PEI coating and CdSe/ZnS QDs were prepared in oil and treated by phase transfer and s-PEI coating. Therefore, we believe that our method has the potential to be a general method for assembling different inorganic nanoparticles onto different biotemplates.

Chapter 3: Solution phase processed thin films made from biotemplated 1D plasmonic nanoparticles array for solar thermoelectric generation

3.1 Introduction

Solar energy, due to its great abundance, long-term sustainability and easy accessibility, has been considered as the most appealing renewable energy resource. Among various solar energy harvesting methods, solar-thermal conversion has been demonstrated useful in many applications including seawater desalination, solar heating, solar thermoelectric generation, and solar thermophotovoltaics. In these applications, a high-quality substrate that can absorb sunlight in broadband and then convert it very efficiently into heat, is essential to the performance of the devices. Recently, plasmonic nanoparticles (NPs) of Au, Ag, Cu and Al, have drawn intensive interest in photothermal applications. One of the most unique characters possessed by plasmonic NPs is perhaps their tunable optical properties originating from the localized surface plasmon resonance (LSPR). Such optical tunability can be achieved through manipulation of size and morphology of the plasmonic NPs, as well as through assembling of the NPs to induce coupling of LSPR between adjacent NPs. The tunable optical property of plasmonic NPs allows on-demand selective absorption of light in a wide range of wavelengths. Besides, plasmonic NPs convert light to heat far more efficiently than other non-plasmonic light absorbers. Both these two advantages make the plasmonic NPs quite suitable for solar based heat generation applications.

Previously, plasmonic solar absorbers have mainly been fabricated through physical approaches, such as focused ion beam and e-beam lithography, thermal

evaporation, physical and chemical vapor deposition.[145-148] However, these approaches are suffering from two drawbacks. First, plasmonic solar absorbers fabricated by these methods usually have complicated multi-layered structure that needs multi-step processing, which makes them neither cost-effective nor easy for scalable production. Second, although the as-fabricated plasmonic solar absorbers have relatively broad optical bands,[145-147, 149-151] they are still far away from absorbing throughout the typically desired wavelength range of the solar light, i.e. 400-2200 nm. On the other hand, in comparison to the physical methods, solution phase synthesis and process of materials can be conducted in a much simpler manner and can be easily scaled up for mass production. In addition, solution phase processing may also enable new properties to materials. For example, films deposited through materials in the solution phase are usually flexible, and thus can be used in the emerging soft electronics fabrication.

Here, for the first time, we introduced a solution-phase approach to fabricate high efficient solar absorbers by using linear biotemplates, namely bacterial flagella. With the assistance of bacterial flagella, we fabricated a novel type of plasmonic absorber which has high absorbance (> 90%) all over a broadband frequency covering 400-2200 nm wavelength range. Different from previous plasmonic absorbers, the composition of our material is relatively simple that only flagella and AuNPs are included. Moreover, no difficult fabrication technique or devices are required while only “wet” chemistry is performed. Briefly, small AuNPs are first assembled on flagella templates through electrostatic interaction forming linear AuNPs arrays. Followed by a further seeded-growth of the assembled AuNPs on flagella, the size and the gap between them are adjustable which consequently makes the spectrum of the composites tunable. When the

gaps between the adjacent NPs getting small enough, interparticle plasmonic coupling fall into the near-field coupling region, which induces strong field localization and enhancement, and finally broaden the absorption spectrum band. This unique property of broadband absorption of the 1D nanocomposites in solution can be easily maintained when they are deposited on a substrate to form a mesoporous 2D black thin film. In this process, the rigidity and steric hindrance which is introduced through the biotemplate restrict the 1D nanocomposites from tight stacking, thus we are able to obtain a mesoporous structure with no requirement for another anti-reflection coating. The fabricated absorber exhibits impressive solar-thermal conversion efficiency and an application in solar thermoelectric generation (STEG) has also been demonstrated in this work. The above mentioned advantages collectively make our proposed system an outstanding candidate and could further widen the application realm of plasmonic absorber materials.

3.2 Materials and Experiments

3.2.1 Materials

Polyethylene glycol (PEG, MW 8000), polyethyleneimine (PEI, MW 1800), sodium borohydride ($NaBH_4$), Gold (III) chloride trihydrate ($HAuCl_4 \cdot 3H_2O$), polyvinylpyrrolidone (PVP, MW 29000), ascorbic acid and dimethylformamide (DMF) were all purchased from Sigma-Aldrich and used as received.

3.2.2 Amplification and purification of flagella template

Salmonella serotype Typhimurium were used as flagella donor in this work. The bacteria were cultured in Luria-Bertani broth medium at 37 °C until OD_{600} 0.8 and then were collected through centrifuge. The pellet was re-suspended in pH 7.5 phosphate

buffered saline (PBS) buffer followed by rigorous vortexing which detaches flagella from the surface of bacterial body. After another round of centrifuge, flagella in the supernatant were precipitated by adding the precipitation solution (150 ml per 1 L of supernatant) which contains 16.7% (w/v) PEG and 3.3M NaCl. After overnight precipitation at 4 °C, the purified flagella were recovered and redispersed in DI water for future use. The protein concentration was quantified by UV absorption at 280 nm.[20, 152-153]

3.2.3 Flagella templated assembly of AuNPs

To obtain positively charged small AuNPs, 1 ml of 5 mM $NaBH_4$ solution was added dropwise to a premixed solution, containing 750 µl of 12 mM $HAuCl_4 \cdot 3H_2O$, 10 µl of 15 wt% branched PEI and 4.25 ml of DI water, under rigorous stirring. The pH of the obtained AuNPs solution was then adjusted to 5.5 by 10 mM NaOH for further electrostatic assembly on biotemplates. In an assembly process, 1.5 ml of 150 µg/ml flagella in water was added to 5 ml of above AuNPs solution. The mixture was then incubated on a rocker shaker for 30 min, followed by a low-speed centrifugation (2000 g) to remove the unassembled AuNPs. After another wash by water, the resultant pellet containing AuNPs-flagealla complexes was collected and resuspended into 500 µl DI H_2O for further seeded growth.

3.2.4 Tuning optical property of AuNPs/flagella assemblies through seeded post-growth

To a 5 ml solution containing 100 µl of washed AuNPs/flagella assemblies, 400 µl of 5 wt% PVP and different amount (3, 9, 27 or 81 µl) of 60 mM HAuCl4, 1 ml of 10 mM ascorbic acid was added dropwise under gentle stirring. After addition of ascorbic

acid, another 30 min stirring was performed to complete the reaction. The post-grown AuNWs were collected and redipersed in H2O for optical property study, or in ethanol for thin film fabrication.

3.2.5 Fabrication of plasmonic thin films with AuNWs or AuNPs

The above AuNWs prepared with 81 μl of HAuCl4 were used for solar film fabrication. 3 ml of a concentrated AuNWs solution in ethanol were added onto a piece of copper substrate, which has been sealed by glass slides along the edges to prevent leak. The sample was air-dried and the resultant black film had an coated area of 4.5 cm x 3.3 cm.

The 50 nm spherical AuNPs used for fabrication of control film were prepared through a seeded method. Briefly, 13 nm citrate-coated AuNPs were first synthesized following a reported method.13 The citrate ligands were then replaced by PVP through overnight rigorous stirring. Then, the PVP-coated AuNPs were centrifuged and redispersed into ethanol in 5 times of the original concentration. To obtain 50 nm AuNPs, 4.4 ml of 0.1 M ascorbic acid in methanol was added dropwise into the growth solution, which contains 0.45 mM HAuCl4, 3% (w/v) PVP, 16 ml of DMF, and 80 μl of the seed solution. The reaction was allowed to take place overnight under gentle stirring. Afterwards, the AuNPs were collected by centrifuge and concentrated into ethanol. The AuNPs control film was made using the same amount of gold and the same evaporation method as the plasmonic absorber described above.

3.2.6 Transmission electron microscopy (TEM) and scanning electron microscopy (SEM) characterization

The morphology of Salmonella Typhimurium and purified flagella were characterized by Zeiss 10A TEM after negative staining using 1 % (w/v) uranyl acetate (UA). The as-assembled and post-grown AuNPs/flagella complex were directly observed without staining. The film samples were first sputter coated with Iridium and the SEM measurements were carried out using a Zeiss NEON high resolution SEM.

3.2.7 Temperature profile measurement

The AuNWs and AuNPs films on copper plates, as well as a pristine copper plate, were placed on top of a thick stack of cotton paper in the open air. A type k thermocouple probe was taped to the edge of the copper substrates, and the temperature was read using a digital multimeter (Southwire, 13070T). Sunlight was simulated using a xenon lamp, and was output through a heat resistant optical fiber. Simulated sunlight with average power density of 0.1 and 0.5 W/cm2 was considered equivalent to 1x and 5x the natural sunlight respectively. For all light-related tests, the substrates were irradiated by simulated sunlight at an angle of 90°.

3.2.8 Assembly and testing of the STEG device

A commercial TEG unit (TECTEG, TEG1-1268-4.3) was used for the tests (Fig. 3.10a). The device was assembled by sandwiching the TEG unit in between the plasmonic film coated copper plate and an aluminum heat sink, with the hot side of the unit contacting with copper plate and the cold side with the heat sink (Fig. 3.10b). The assembled device was tightened with screws to ensure good thermal contact between each components.

When testing the device under simulated sunlight, the heat sink was placed half way underwater at room temperature. The voltage generated and the surface temperature of the copper plates were collected using a digital multimeter. The thermal images were taken using an infrared camera (ICI 7320P). All the tests were conducted under ambient conditions.

3.3 Results and Discussion

3.3.1 Fabrication of AuNPs-flagella assemblies

Bacterial flagella are protein nanofibers protruding from the cell surface. They function to sense external environment, as well as to control the motion of bacteria.[154-155] The intact flagella on bacteria can reach up to 20 μm in length with only about 14 nm in diameter. Such extremely high aspect ratio makes them idea template for 1D nanoparticles assembly. Moreover, the bionanofibers are assembled from helically arranged flagellin protein monomers in an extremely ordered manner. Thus, the chemical and physical properties of flagella are highly uniform throughout the entire surface, which makes them further favored for templating nanomaterials. The flagella used in this work were non-costly mass amplified and purified from wild type Salmonella Typhimurium, which bears high flagella density (Fig. 3.1a). Due to the use of vortex for flagella detachment, some of the bionanofibers were broken into shorter pieces during purification. The length of the purified flagella is generally ranged from several microns to 15 microns (Fig. 3.1b). Though shorter than the intact flagella, they are still much longer than other widely used 1D biotemplates in nanomaterial synthesis such as bacteriophages and tobacco mosaic virus (TMV), which are generally less than 1 μm in length.[13-14, 156-157]

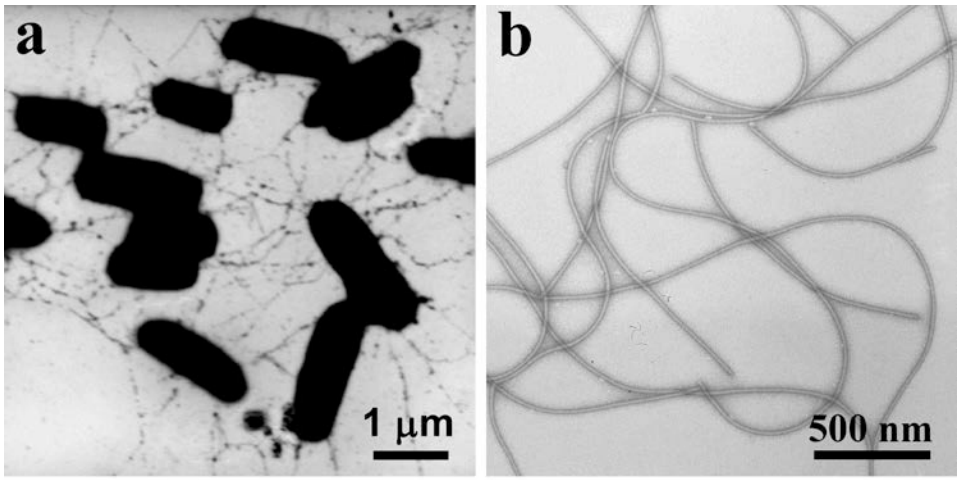


Figure 3.1: TEM images of flagella templates and AuNPs/flagella assemblies. a) Salmonella Typhimurium which have flagella protruding from the bacterial bodies. b) Purified flagella bionanofiber. Negatively stained with 1% UA.

We adopted an electrostatic-based strategy to assemble AuNPs onto flagella. A detailed investigation on the templated assembly will be reported elsewhere. Because the isoelectric point for flagellin monomer is about 5.3,[152, 158] the flagella can be considered as negatively charged supermacromolecules under neutral conditions. PEI is a hyperbranched polymer and rich in amine groups, thus it is an ideal surface capping agent for the preparation of positively charged NPs. The as-prepared PEI coated AuNPs are well dispersed in water and are 3-5 nm in diameter (Fig. 3.2a, see experimental section for details of preparation). To assemble the PEI coated AuNPs onto flagella, the two solutions were mixed under a proper pH condition. Within a few minutes, colored fine flocculates appeared out from the previously clear solution, suggesting the formation of AuNPs/flagella complex. The flocculates were collected by centrifuge. The pellets can be redispersed into water to form a stable suspension without visible flocculates. TEM examination shows that AuNPs have been evenly and densely

assembled to the surface of flagella and formed neat 1D AuNPs arrays (Fig. 3.2b&c). The TEM result confirms that our electrostatic based strategy is highly effective to induce the assembly of PEI coated positively charged NPs onto negatively charged flagella template. We also studied the absorption spectra of the AuNPs before and after assembly onto flagella. However, no obvious difference in the LSPR band was noticed, suggesting that although densely assembled, there is not much plasmon coupling among AuNPs on flagella, mainly due to their smaller size and large inter-particle distance in relative to the size of AuNPs.

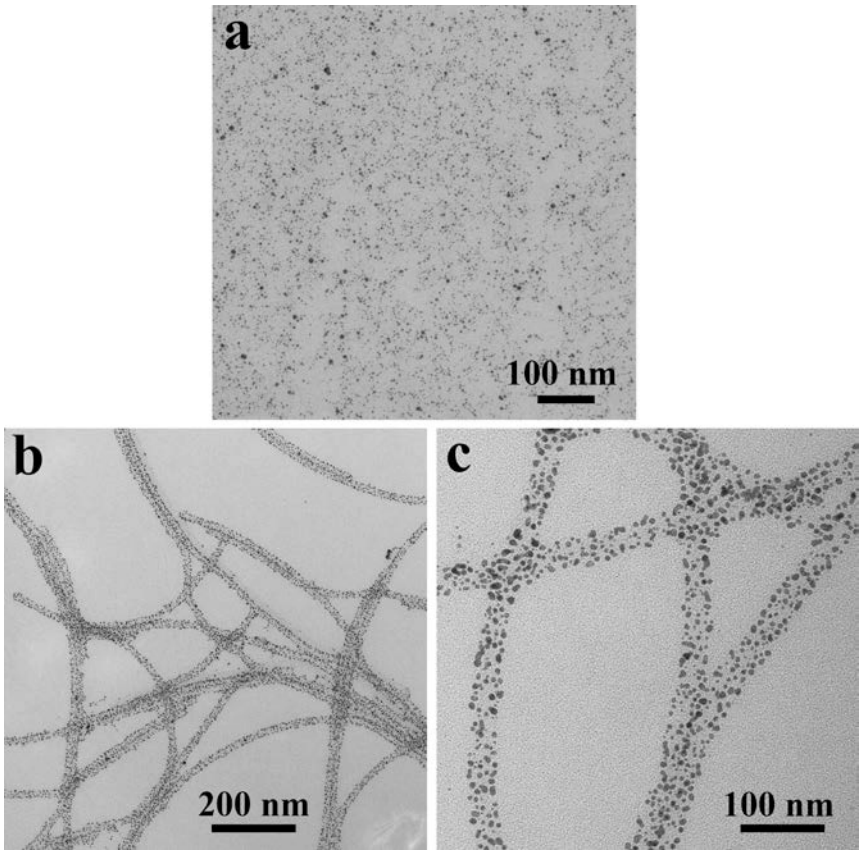


Figure 3.2: TEM images of AuNPs and AuNPs/flagella assemblies. a) AuNPs. b) and c) AuNPs/flagella assemblies at low (b) and high magnification (c). The AuNPs densely assembled all over the biotemplates which clearly displayed the morphology of flagella without negative staining.

3.3.2 Manipulation of extinction spectra of AuNPs/flagella assembly in solution

In comparison to smaller AuNPs (i.e. 3-5 nm), larger sized AuNPs will have much stronger LSPR effect. Besides, when multiple metal NPs are located closely to each other (i.e. sitting into an 1D array), the LSPRs of individual NPs are coupled owing to the electromagnetic interactions. And when the inter-particle distance is small enough to fall into the near-field coupling region, strong field localization and enhancement will happen and lead to the broaden of the optical band.[159] Therefore, we further conducted overgrowth on the AuNPs/flagella assemblies. In this process, the small AuNPs that had been immobilized onto the flagella template acted as seeds and grew into larger sized AuNPs, which simultaneously led to smaller inter-particle distance. As a result, both the LSPR band intensity and width of the 1D AuNPs array increased, favoring strong absorption toward the wideband solar light.

The reagents involved in the overgrowth process included AuNPs/flagella assembly, $HAuCl_4$, ascorbic acid and PVP in water. With the addition of a weak reducing agent (ascorbic acid), Au ions would only be reduced on the surface of AuNPs seeds. In the seeded growth, the amount of $HAuCl_4$ solution was tuned from 3 μl, 9 μl, 27 μl to 81 μl (see details in the method section) while keeping the amount of AuNPs/flagella assemblies constant. With increased supply of $HAuCl_4$, the size of AuNPs on flagella became increasingly larger, as a consequence, the gaps between adjacent NPs getting increasingly smaller (Fig. 3.3). And this allows us to fine tune the optical property of the AuNPs/flagella assemblies. The alteration of optical properties can be easily observed by color changes of the post-grown solutions, which turned to light red (3 μl), light purple (9 μl), dark purple (27 μl) and greyish black (81 μl)

respectively (Fig. 3.4a). The absorption spectrum were also explored. Consistent with the color change, the LSPR bands were broadened gradually and finally became flattened over a long wavelength range with 81μl of $HAuCl_4$ added (Fig. 3.4b). As a control, freely dispersed 50 nm AuNPs, which were of comparable diameter to the individual AuNPs in the 1D arrays in Fig. 2d, only showed a narrow LSPR band at around 540 nm (Fig. 3.5). This further confirms that the strong coupling between the neighboring AuNPs is the predominant reason for the broadband absorption of the AuNPs/flagella 1D assemblies. From now on, the 1D AuNPs/flagella assemblies will be termed as plasmonic Au nanowires (AuNWs).

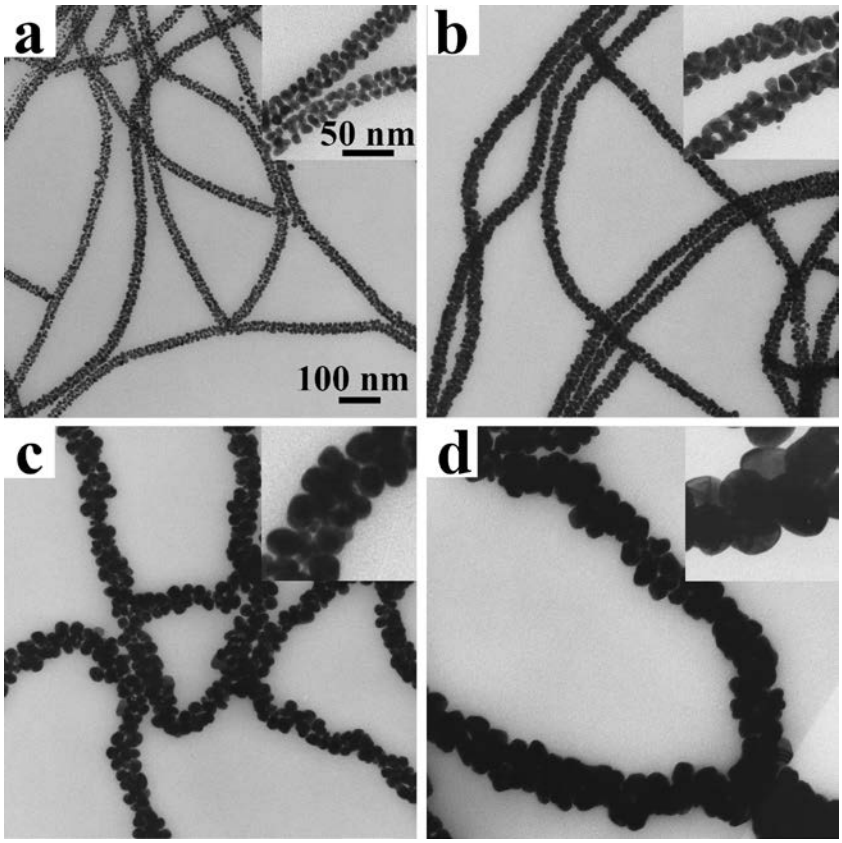


Figure 3.3: Morphology of post grown AuNPs/flagella complexes. TEM images. Insets: high magnification images. The amounts of $HAuCl_4$ added to the post growth reactions are 3 μl (a), 9 μl (b), 27 μl (c) and 81 μl (d), respectively.

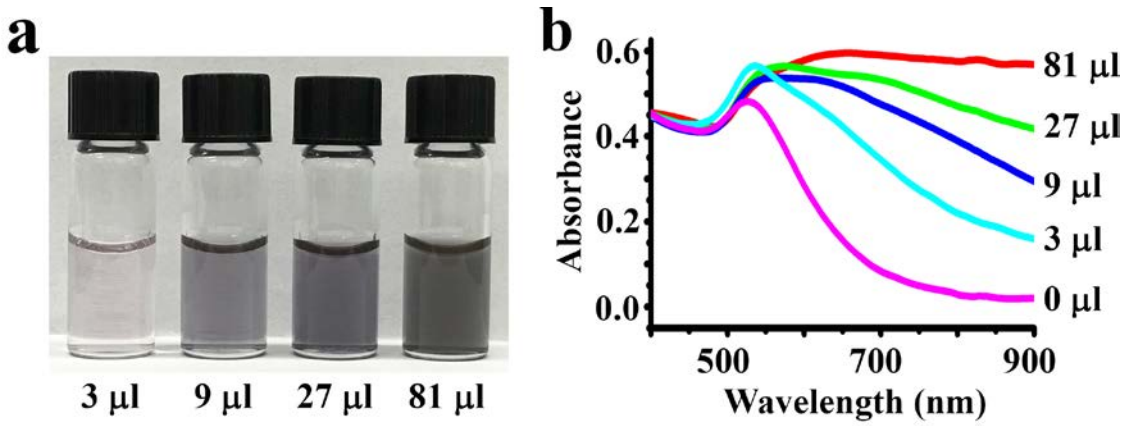


Figure 3.4: Optical property of post grown AuNPs/flagella complexes. a) AuNPs/flagella complexes in solution after post growth. b) Absorption spectrum from 400 nm to 900 nm. With the increasing of $HAuCl_4$, the SLPR band was getting broader.

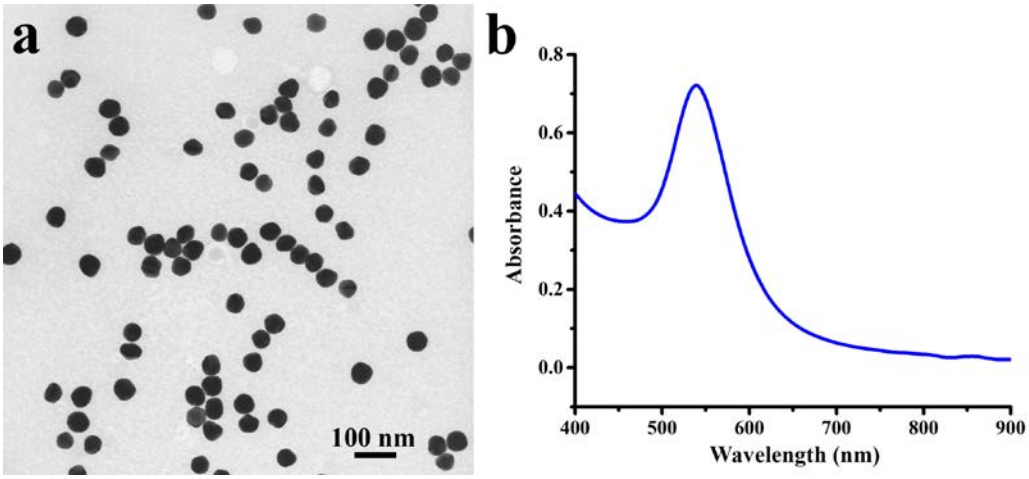


Figure 3.5: TEM and Spectrum of 50 nm AuNPs. a) TEM image of AuNPs. The diameter of the NPs is about 50 nm. b) Spectrum of 50 nm AuNPs in solution.

3.3.3 Thin film fabrication with plasmonic AuNWs

The plasmonic AuNWs (Fig. 3.3d) with the broadest LSPR band were selected for the fabrication of thin film for solar thermal generation. Ethanol dispersed plasmonic AuNWs were first pipetted directly onto an edge-sealed copper plate, the solvent was

then evaporated under ambient conditions to obtain the thin films. The resultant film has lateral lengths of 4.5 cm× 3.3 cm (Fig. 3.6b), and its dark black color indicates that the optical properties of the original plasmonic AuNWs in the solution phase have been successfully maintained after being dried out to form films. As a control group, AuNPs film which was composed of only free AuNPs of similar size (50 nm) but without flagella templates was also fabricated. The as-prepared AuNPs film exhibited a shiny gold appearance (Fig. 3.6a), very close to that of the bulk gold. Copper plate was used here as the substrate because of its high thermal conductivity, which is important for the performance of the STEG device.

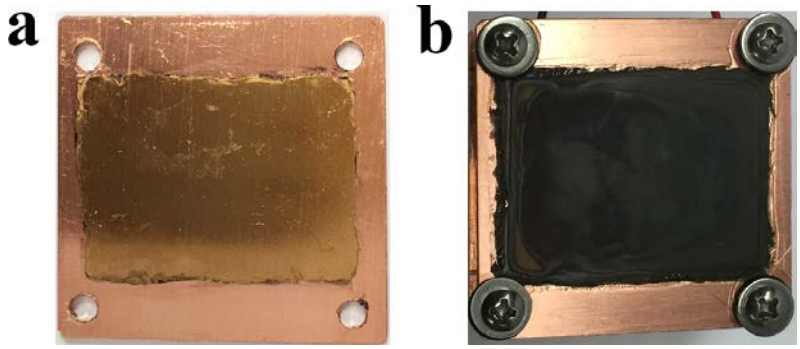


Figure 3.6: Digital images of plasmonic AuNWs film (b) and AuNPs film (a) coating on copper plates.

To further address the difference between the two films, their optical properties and structures were investigated. The plasmonic AuNWs film had a broadband absorption that covered the whole effective solar spectrum (400-2200 nm), with at least 90% absorption at each wavelength (Fig. 3.7). In contrast, the AuNPs film had much weaker absorption. Its absorption dropped to 80% at 620 nm, and further dropped to 70% and 40% at around 1000 nm and 1600 nm, respectively. Under SEM, in the AuNPs film, the AuNPs were piled up tightly and each was closely contacted with the neighboring

NPs (Fig. 3.8a&b), which made the overall film compact and smooth with high reflection. However, the black plasmonic AuNWs film were composed of loosely organized linear AuNPs/flagella assemblies and the whole structure was mesoporous (Fig. 3.8c&d). We think this flagella-based unique structure significantly contribute to the broadband absorption of the plasmonic AuNWs film in two aspects. First, as mentioned previously, the adjacent NPs on an individual flagellum fiber were restrained from contacting with each other and separated by small gaps, which led to strong plasmon coupling effect and greatly broadened LSPR band. This is mainly the result of post-growth of the pre-immobilized AuNPs seeds on the flagella templates. Second, unlike free spherical AuNPs, the rigidity and steric hindrance of the linear AuNPs/flagella assemblies would prevent the formation of tight stacking or bundled structures during evaporation-based thin film fabrication. Instead, mesoporous structures were formed. When a beam of light comes in, the mesoporous structure can effectively enhance the light absorption through reducing direct light reflection back into air, but inducing multiple reflection of light inside the mesoporous structure.[160] In general, the flagella template played an essential role in the generation of the outstanding optical property of the fabricated plasmonic AuNWs film.

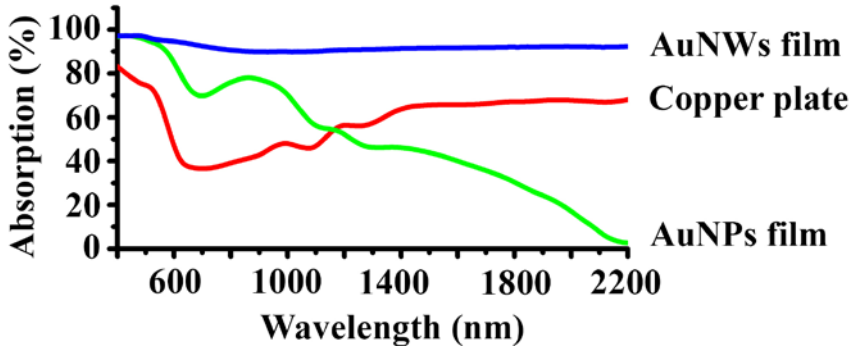


Figure 3.7: Optical property of plasmonic AuNWs film. Spectrum of plasmonic AuNWs film, AuNPs film and copper plate. AuNWs film exhibited a broadband absorption with high efficiency.

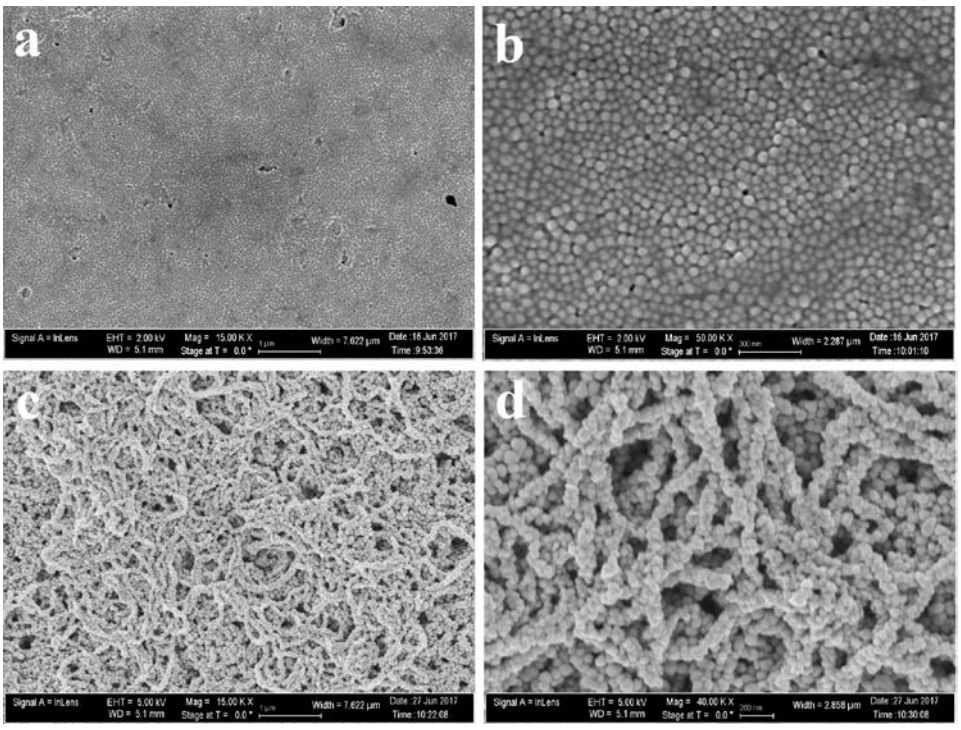


Figure 3.8: Morphology of plasmonic AuNWs film. a) and b) SEM images of AuNPs film. c) and d) SEM images of plasmonic AuNWs film. a) and c) Low magnification; b) and d) high magnification. AuNPs film was composed of tightly packed AuNPs, while plasmonic AuNWs film was composed of linear AuNPs/flagella complexes which formed a mesoporous structure.

The conversion of solar energy to heat was also studied. The plasmonic AuNWs film coated copper (AuNWs/Cu) plate and pure AuNPs film coated copper (AuNPs/Cu) plate, as well as the pristine copper (Cu) plate, were set on top of a thick stack of cotton paper to minimize heat transfer. Simulated sunlight with 1x (0.1 W/cm^2) and 5x (0.5 W/cm^2) the natural sunlight power intensity were irradiated on the films, and the surface temperature was recorded during the 16 min irradiation. For all the films, the temperature increased along with the irradiation time (Fig. 3.9a). In the first several minutes, the temperature increased quickly, and then slowed down because of the heat loss to the environment. After irradiation by 1x sunlight, the temperature increase, ΔT, defined as T_{960sec}-T_{0sec}, of the AuNWs/Cu plate was 47.5 °C, which was much higher than that of the Cu plate (20.2 °C) or AuNPs/Cu plate (28.0 °C) (Fig. 3.9b). When 5x sunlight was applied, the temperature difference became increasingly larger, and the ΔT were 73.9 °C, 103.3 °C and 144.5 °C for Cu, AuNPs/Cu, and AuNWs/Cu plates respectively.

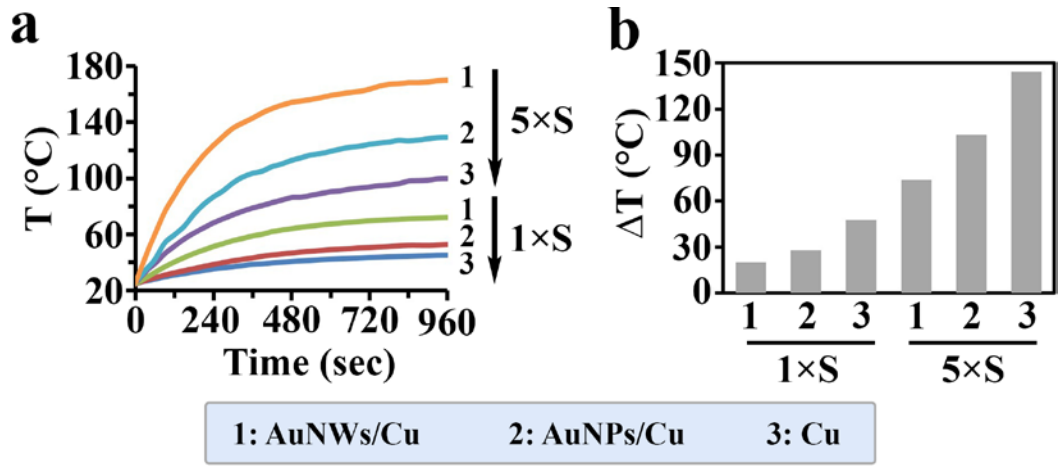


Figure 3.9: The conversion of solar energy to heat through plasmonic AuNWs film. a) Temperature profile irradiated by simulated sunlight of 1× and 5× the natural sunlight power intensity. b) Plot of the temperature increase ($\Delta T=T_{960sec}-T_{0sec}$) for each film. AuNWs/Cu, plasmonic AuNWs film coated copper plate; AuNPs/Cu, pure AuNPs film coated copper plate; Cu, pristine copper plate. 1×S, 1× sunlight power; 5×S, 5× sunlight power.

3.3.4 Plasmonic AuNWs thin film based solar thermoelectric generation (STEG)

STEG is an effective way to exploit solar energy, in which heat generated by solar light is used as source for thermoelectric generation.[161] A powerful solar absorber that can convert the sunlight into heat at high efficiency will significantly boost the performance of the device.[162] Therefore, to demonstrate the potential application of our plasmonic AuNWs based thin film for solar thermal conversion, we constructed a STEG device with a commercial TEG segment (Fig. 3.10) (see details in method section). During testing, the heat sink part was placed halfway in a water bath to maintain the cold side at a relatively low temperature (about 24.5 °C). Throughout the simulated sunlight irradiation, the voltage generated by the device was recorded, and the

temperature of the hot side (AuNWs/Cu, AuNPs/Cu, or Cu plates) was monitored by both a thermal probe and an infrared camera. As it can be seen that, both the voltage and the temperature increased rapidly at first and shortly after reached a steady state (Fig. 3.11a&b, Fig. 3.12), at which the solar heat generation and heat transfer to the TEG segment was balanced. The output voltages at the steady state for STEG assembled with AuNWs/Cu, AuNPs/Cu and Cu plates under 1x power intensity are 254.4, 149.5 and 92.0 mV, respectively, and 1061.0, 622.0 and 356.9 mV under 5x power intensity, respectively. The correlation between the output voltage and the temperature of the hot side is also plotted in Fig. 3.11c. Both the temperature and output voltage suggest that our plasmonic AuNWs based thin film can absorb and convert solar energy more efficiently, resulting in higher temperature increase and subsequently higher output voltage out of the STEG device. It is worth noting that under 5x concentrated simulated solar irradiation, the stable output voltage reached more than 1 V. Considering that the STEG device was not encapsulated in vacuum, thus there was considerable air conduction heat leakage. And besides, the number of thermal contacts has a negative impact on the thermal conduction in the TEG device. By using in-house built TEG segment, the number of thermal contacts can be reduced by half, which will enhance the thermal flow and therefore, performance of the device.

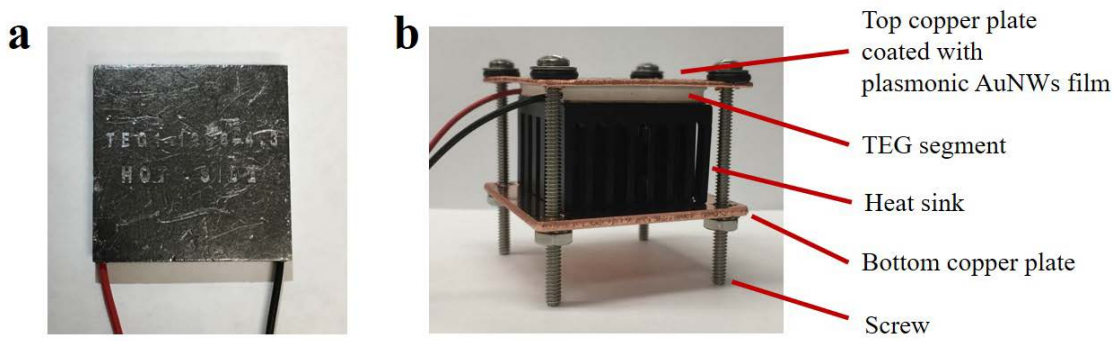


Figure 3.10: STEG device. a) Commercial TEG segment. b) STEG device.

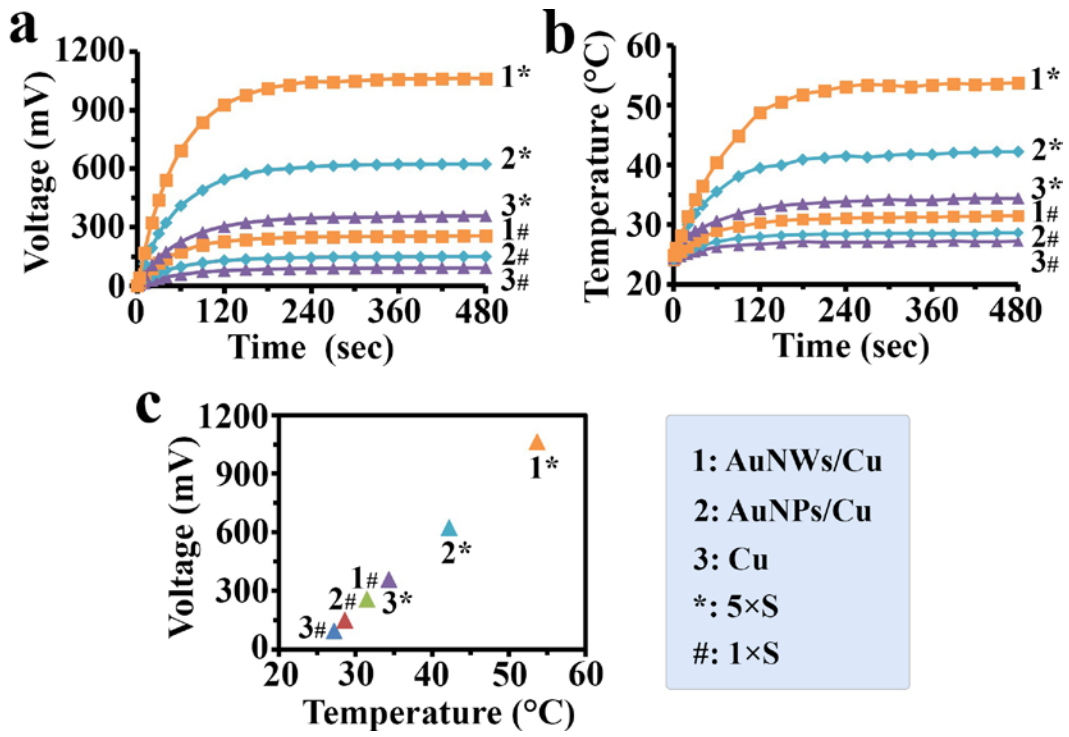


Figure 3.11: Performance of STEG device using plasmonic AuNWs film as solar absorber. a) Voltage-time curve of different films. b) Temperature-time curve of different films. c) Plot of voltage to temperature of hot side at the end point of testing (480 sec). AuNWs/Cu, plasmonic AuNWs film coated copper plate; AuNPs/Cu, pure AuNPs film coated copper plate; Cu, pristine copper plate. 1×S, 1× sunlight power; 5×S, 5× sunlight power.

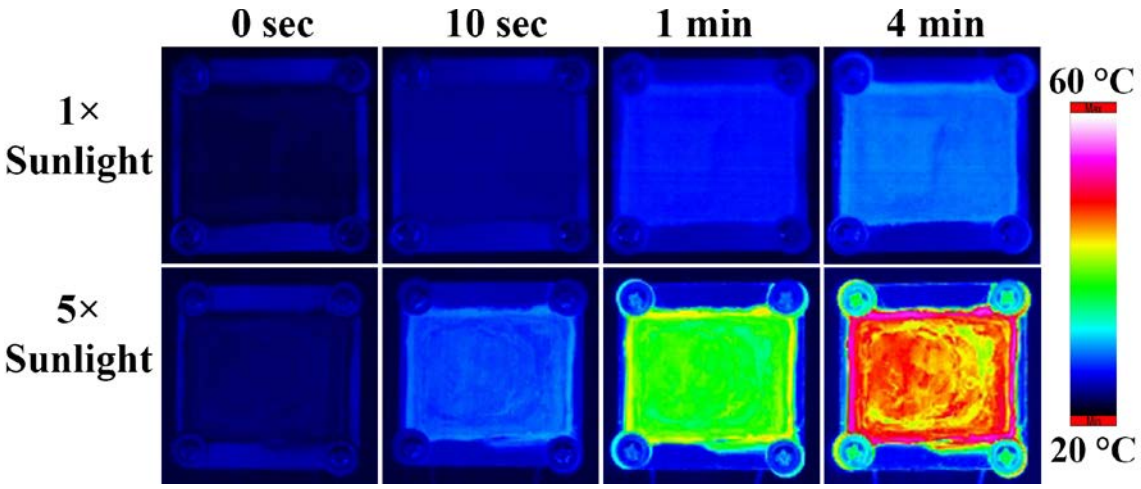


Figure 3.12: Infrared camera images of plasmonic AuNWs film during irradiation.

3.4 Conclusion

In summary, we employed a novel strategy to use bacterial flagella nanofibers as templates to assemble small AuNPs into linear arrays. Due to the relatively small size, the AuNPs were assembled in 3D manner around the cylindrical surface of the templates. Then through a seed-mediated overgrowth process, we successfully created plasmonic AuNWs. The overgrowth process simultaneously increased the AuNPs size on the templates as well as reduced their inter-particle distances, thus inducing 3D coupling of surface plasmon of AuNPs on the template and leading to a significantly enhanced and broadened LSPR bands. We then took advantage of the broadband absorption property of the plasmonic AuNWs and used them as effective solar absorbers. The as-constructed plasmonic absorber exhibited efficient solar-thermal conversion. When such absorber was used in a STEG device, it has been demonstrated capable of generating 1V voltage under 5x solar irradiation. In comparison to the current physical method of fabricating solar absorbers, the composition and fabrication process in our method are simple and environmentally friendly, which opens up a

promising alterative approach for thermal concentration in the conversion of solar energy into electricity.

Chapter 4: Virus activated artificial ECM induces the osteoblastic differentiation of mesenchymal stem cells without osteogenic supplements

4.1 Introduction

Stem cell niche as a specific extrinsic mircoenvironment integrate a complex array of molecular signals that, in combination with induced cell-intrinsic regulatory networks, control stem cell function and balance their numbers in response to physiological demands.[163-164] In most instances, stem cells in the niche are in contact with extracellular matrix (ECM), which provides multiple structural and biochemical cues to govern a series of stem cell behaviors in the temporal and spatial dimension.[165-166] Thus, more attention is being paid to the design of artificial ECM (aECM) by integrating some physical, chemical and/or mechanical factors into biomaterials for directing stem cell functions.

Nanotopograpy as a particular physical factor is now receiving more interest because it has advantageous features such as a large surface-to-volume ratio and a higher degree of biological plasticity compared with conventional micro- or macrostructures.[167] Emerging literature presents many interesting findings on how nanotopography enhances cell adhesion, alters cell morphology, affects cell expansion, initiates intracellular signaling, provides contact guidance and mediates stem cell differentiation.[93-94, 98, 167-168] Considering nanoscale topography in the design of biomimetic materials is a fashional idea because the resulting materials resemble the *in vivo* niche. On the other hand, biochemical cues as a traditional regulatory factor in the stem cell niche have been widely studied for a long time.[169-171] These signals can be

classified into three types, including integral membrane proteins, localized secreted ECM components and soluble proteins like growth factors and cytokines.[164] The biochemical cues have been demonstrated to affect stem cell fates by targeting some specific signaling pathways such as β1 integrins activated MAPK signaling, Wnt signaling pathway in the hematopoietic stem cell (HSC) and Notch signaling in the development of the nervous system.[172-174] Therefore, it is increasingly interesting to introduce biochemical factors into artificial materials to directly control cell behaviors.

M13 filamentous phage, a virus that specifically infects bacteria and is harmless to human beings, is a bionanofiber (~880 nm long and ~6.6 nm wide).[94, 101] It is made of DNA as a core and protein coat as a sheath that wraps the core. The coat protein constituting the side wall of phage is termed pVIII and encoded by gene VIII of the phage DNA. Compared to other nanofibers, M13 phage is unique in that it cannot only be used as an organic building block to build 2-D films and 3-D scaffolds with unique topographical structures through self-assembly, but also introduce different peptides on the constituent building block to provide biochemical cues by the well-established phage display technique.[94, 98] Inserting a foreign gene into gene VIII leads to the display of a foreign peptide as fusion to pVIII and the concomitant presentation of foreign peptide on the side wall of phage. The ease of displaying a peptide on the side wall of phage nanofibers enables us to use phage to study the peptide cues (biochemical cues) that can direct the stem cell fate. In addition, the ease of assembly of phage nanofibers into a nanostructured film further gives us the capability of studying the stem cell fate on a nanostructure with specific peptide sequence displayed on the phage nanofibers that generate a unique nanotopography. These unique properties of phage allow us to

systematically study the effect of different peptides on the substrates with constant nanotopography on the stem cell fate (Fig. 4.1).

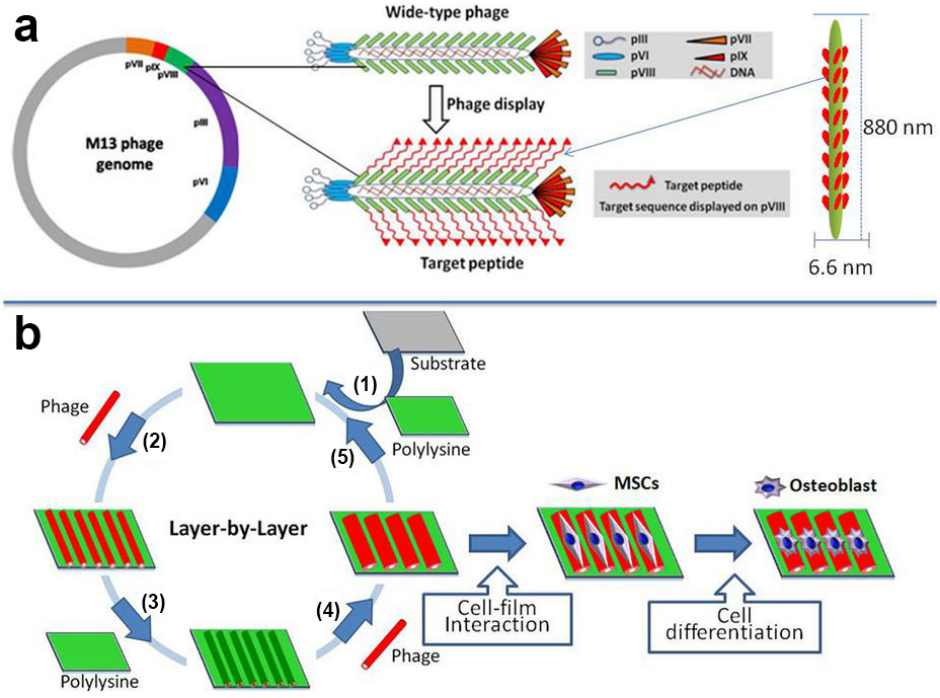


Figure 4.1: Schematic diagram of using phage display technique to produce biomaterials with both unique nanostructures and functional peptides displayed for directing stem cell fate. a) Foreign peptides (RGD or PHSRN) derived from fibronectin were separately inserted and displayed in the N-terminal end of major coat protein (pVIII) constituting the side wall of M13 phage. b) The engineered phages were further used to form phage-based film biomaterials via a layer-by-layer self-assembly method. The polylysine was introduced as the first positively charged layer on the substrate, and then the engineered phage was deposited as a second negatively charged layer. This process was repeated for three times and a phage-based film was formed with phage as a terminating layer (step 1-5). The resultant phage-based films with precisely introduced peptide sequences and well-defined ridge/groove topographical feature were found to direct osteoblastic differentiation of mesenchymal stem cells (MSCs).

In this work, we employed a phage display approach to generate a virus-activated aECM with well-defined topographical and biochemical cues to activate the regulation of the morphology, proliferation and osteoblastic differentiation of rat mesenchymal stem cells (MSCs). We separately displayed different fibronectin-derived peptides (RGD, its synergy site PHSRN, and a combination of RGD and PHSRN) on the side wall of phage nanofibers through phage display technique, and assembled them into a 2-D film based on our established layer-by-layer self-assembly method.[94] We chose to study the two fibronectin-derived peptides to be displayed on phage surface based on the following considerations. Fibronectin is a crucial ECM component of many tissues and regulates a variety of cell activities predominantly through direct interactions with cell surface integrin receptors.[175] The identified adhesive domains of the fibronectin are comprised of at least two minimal and pivotal peptide sequences, including an Arg-Gly-Asp (RGD) sequence located in the 10th type III repeating unit and a Pro-His-Ser-Arg-Asn (PHSRN) sequence in the 9th type III repeating unit.[176] The RGD and PHSRN sequences as pervasive adhesive peptides can influence multiple cell behaviors including cell adhesion, proliferation and differentiation.[175, 177-180]

4.2 Materials and Experiments

4.2.1 Peptides display and films fabrication

RGD and PHSRN were respectively displayed on the N-terminus of pVIII, which was the major coat protein constituting the external side wall of M13 bacteriophage, by following our reported protocols (Fig. 4.1a).[90, 181-182] Filamentous phages were assembled into films following a layer-by-layer self-assembly method developed by our group (Fig. 4.1b).[94] Briefly, the disc-shaped cover slide was sonicated and washed with

DI water, and placed into each well of 24-well culture plate. The poly-L-lysine solution (0.01%) was added to the well with cover slide to form the first layer with positive charge on the cover slide. After drying, the phage solution was added to form the secondary layer with negative charge. The process was repeated for three times and a film was formed on the cover slide with phage as a terminating layer. The morphologies of the individual phage nanofibers were observed by transmission electron microscope (TEM, ZEISS 10A) and Atomic force microscope (AFM, BioScope Catalyst, Bruker) and the fabricated films were examined by optical microscope, fluorescence microscope and scanning electron microscope (SEM, JSM-840A).

4.2.2 Cell culture and seeding

Rat MSCs were purchased from Invitrogen (No: S1601-100) and expanded in the primary media, which contained Dulbecco's Modified Eagle Media (DMEM, Gibco), 15% fetal bovine serum (FBS, Gibco) and 1% antibiotics (penicillin 100 U/ml, streptomycin 100 U/ml). The MSCs in their third passage were seeded onto the phage-based films, and then cultured in primary media. The media was replaced twice a week and the culture was terminated after two weeks.

4.2.3 Cell proliferation

For study of cell viability and proliferation, the MSCs were seeded onto the phage-based film materials to investigate the biocompatibility of different materials and the effects of different concentrations of phage used to make the films in the primary media. The phage concentration was varied from low to high values, including 10^{10} pfu/ml, 10^{11} pfu/ml, 10^{12} pfu/ml, 10^{13} pfu/ml, 10^{14} pfu/ml, 5.0×10^{14} pfu/ml and 7.5×10^{14} pfu/ml. The cell proliferation was then measured by 3-(4,5-dimethylthiazol-2-yl)-

2,5-diphenyl tetrazolium bromide (MTT, Sigma) staining at the designed time points including day 1 and day 3. The cell-film complex was incubated in the MTT solution (20 μl, 5 mg/ml) at 37°C in 5% CO_2 incubator for 4 h. The intense purple formazan derivative formed via cell metabolism was eluted and dissolved in 150 μl/well dimethylsulfoxide (DMSO, Sigma). The absorbance was measured at 490 nm on a plate reader (Biotek, USA).

4.2.4 Immunofluorescence staining

All engineered phage films for osteoblastic differentiation were derived from the constant phage concentration of 10^{13} pfu/ml. After cultured for 2 weeks in primary media, the cells on the films were washed and fixed with 4% paraformaldehyde at 4°C for 30 min. They were permeablized using 0.3% Triton X-100 for 5 min and then blocked with 5% goat serum solution for 1 h at room temperature. After blocking, the cells were incubated overnight at 4°C with the primary antibodies targeting the osteo-specific proteins (Osteocalcin, OCN and osteopontin, OPN) and non-osteo-specific protein (collagen I-α1, COL). Secondary antibody labeled by TRITC was used for labeling OCN, OPN, and COL, respectively, at 1:1000 dilutions in a blocking buffer for 1 h at room temperature. Alexa Fluor 488 phallodin (1:400 in PBS) and DAPI (4,6-diamidino-2-phenylindole) were used to stain the actin filaments and nuclei, respectively. Images of the stained samples were collected with a fluorescence microscope (Nikon, Ti-S).

4.2.5 Real-time polymerase chain reaction (PCR)

Real-time PCR was further assayed by Ambion Power SYBR Green cells-to-Ct Kit (Invitrogen, US) in both primary and osteogenic differentiation media. The template

cDNA was amplified with real-time quantitative PCR using gene-specific primers of OCN, OPN and COL. Acidic ribosomal phosphoprotein (Arbp) was used as a reference gene. Sequences of the primers in this study were shown in Table 4.1. The real-time PCR reaction was done using the following protocol: initial denaturation at 95°C for 5 min and 45 cycles of PCR (95°C for 30 s, 58°C for 30 s and 72°C for 45 s). The assay was carried out in triplicate and relative gene expression was calculated with respect to the gene expression in the control substrate without phage film.[183]

Table 4.1: The primer sequences for Real-time PCR analysis.

Gene	Sequence of primer	Length of fragment
OCN	5’-AAAGCCCAGCGACTCT-3’ 5’-CTAAACGGTGGTGCCATAGAT-3’	217 bp
OPN	5'-GACGGCCGAGGTGATAGCTT-3' 5'-CATGGCTGGTCTTCCCGTTGC-3'	209bp
COL	5’-TCCTGCCGATGTCGCTATC-3’ 5’-CAAGTTCCGGTGTGACTGGTG-3’	235bp
Arbp	5'-CGACCTGGAAGTCCAACTAC-3' 5'-ATCTGCTGCATCTGCTTG-3'	109bp

4.2.6 Assay of alkaline phosphatase activity

After culture for two weeks in the primary media, the MSCs seeded on phage-based film materials were tested for alkaline phosphatase (ALP) activity. The assay was performed by p-nitrophenyl phosphate (pNPP) method. Briefly, the pNPP was used as a substrate for ALP to be hydrolysed to form a soluble yellow reaction products at pH 10.5 and 37°C. The staining reaction was terminated by the addition of 3 M NaOH and the final color showed a maximum absorbance at 405 nm.

4.2.7 Statistical analyses

All experimental analysis of cell proliferation, real-time PCR and ALP assay were performed in triplicate (n = 3). The data were expressed as mean ± SD (standard deviation) at a significance level of $p < 0.05$. Differences among groups were determined by a one-way ANOVA with a Bonferroni *post hoc* analysis with SPSS software (version. 17).

4.3 Results

4.3.1 Self-assembly of phage-based films

Due to the long-rod structure and monodispersity of phage nanofibers (Fig. 4.2),[98, 184] they were firstly assembled into bundles, which were further assembled in a parallel format to form a 2-D phage-based film material on poly-L-lysine substrate (Fig. 4.1b and Fig. 4.3). The resultant film showed a slightly rough surface and ordered ridge/groove topography (Fig. 4.4). The formation of the phage-based film was driven through liquid crystalline phase transitions at the air-liquid interface during the evaporation process.[93-94, 185] In addition, the electrostatic interaction between negatively chargely phage nanofibers and positively chargely polylysine substrate provided another driving force to promote the assembly of phage bundles into films with a unique highly ordered topography where phage bundles as ridges were parallel to each other and separated by grooves.

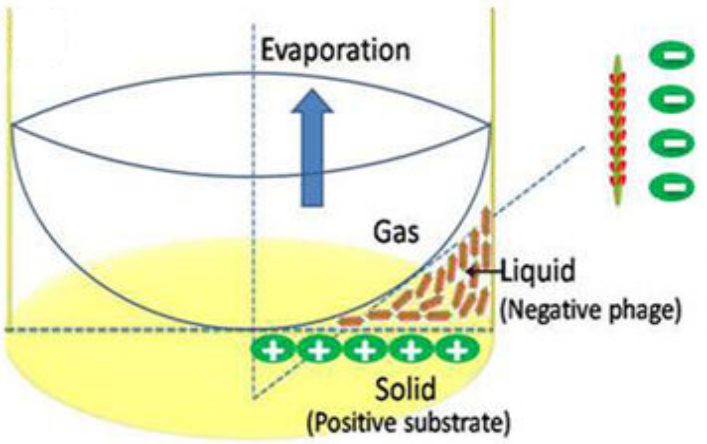


Figure 4.2: Mechanism of film formation. The M13 phage with nanofiber-like structure and monodispersity was driven to form a film by liquid crystalline phase transitions at the arc-shaped air-liquid interface and electrostatic interaction between negatively charged phage nanofibers and positively charged polylysine substrate.

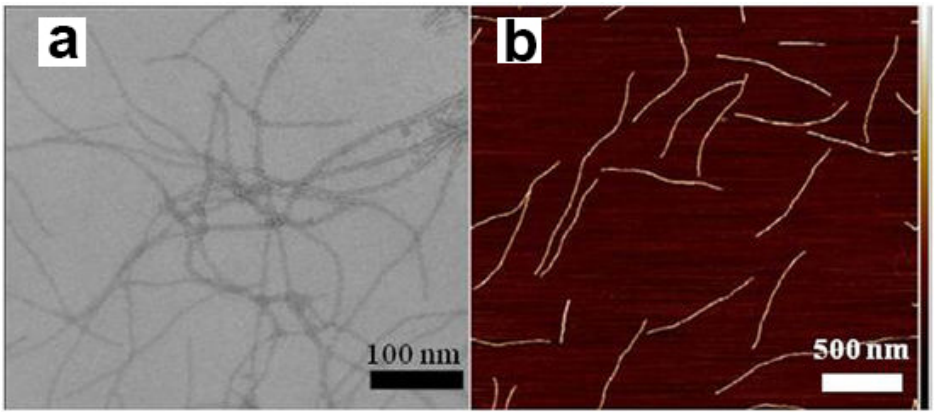


Figure 4.3: M13 phage biofibers. The morphology and size of individual phage nanofibers before they were used to form a film were observed by TEM (a) and AFM (b).

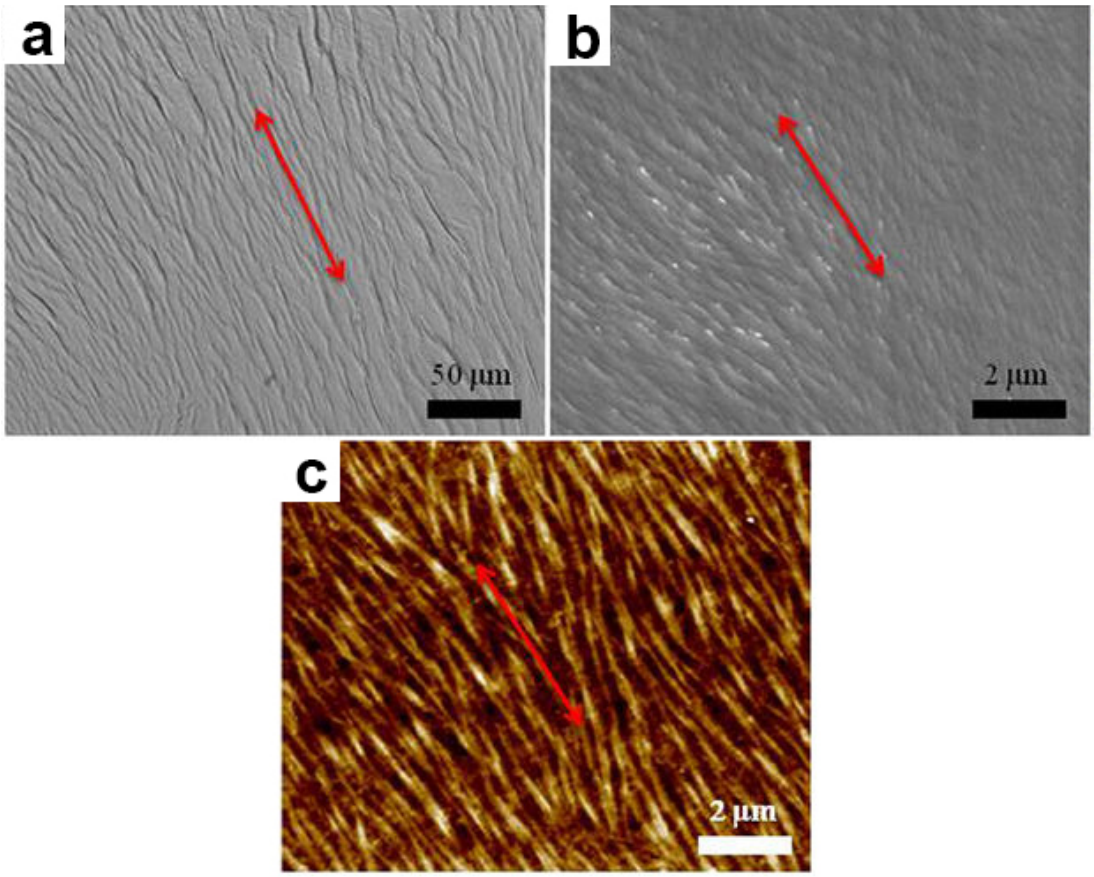


Figure 4.4: Characterization of phage-based film materials. The phage-based film had a unique topography of ridge/groove nanostructure. a) Bright field; b) SEM; c) AFM. The red arrows highlight the highly oriented self-assemblies of phage bundles.

4.3.2 Morphology and nanotopography of phage-based films

We found that the specific ordered ridge/groove topography was controlled by the concentration of phage solution during layer-by-layer assembly. The diameter of phage bundles was around 1000 nm at the higher phage concentration (10^{14} pfu/ml) whereas the diameter was about 500 nm at the lower phage concentration (10^{12} pfu/ml) (Fig. 4.5). In addition, our current data showed that the roughness of phage-based films was dependent on the phage concentration and increased with the rise of the phage concentrations (Fig. 4.6 and Fig. 4.7). Therefore, the surface topography of phage films

could be regulated by altering the size of phage bundles, which could be controlled by varying the phage concentrations.

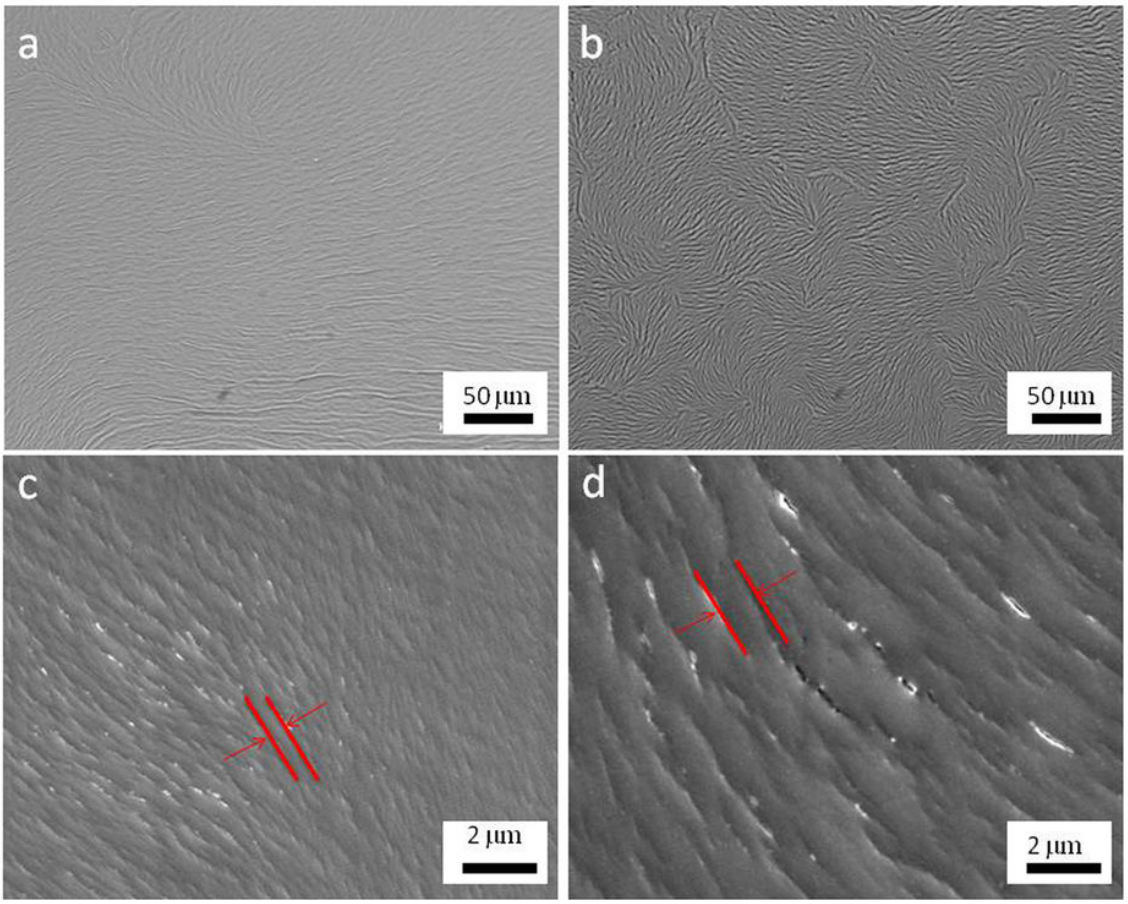


Figure 4.5: Morphology of phage-based film derived from the different phage concentrations. The phage bundles derived from the lower concentration (10^{12} pfu/ml, a and c) of phage solution was smaller than those from the higher concentration of phage solution (10^{14} pfu/ml, b and d). The orientation of phage bundles between neighboring domains is similar and the phage nanofibers showed a longer range parallel alignment with each other in the lower concentration (a and c). However, the orientation of phage bundles was similar inside a small domain but different between neighboring domains in the high concentration (b and d).

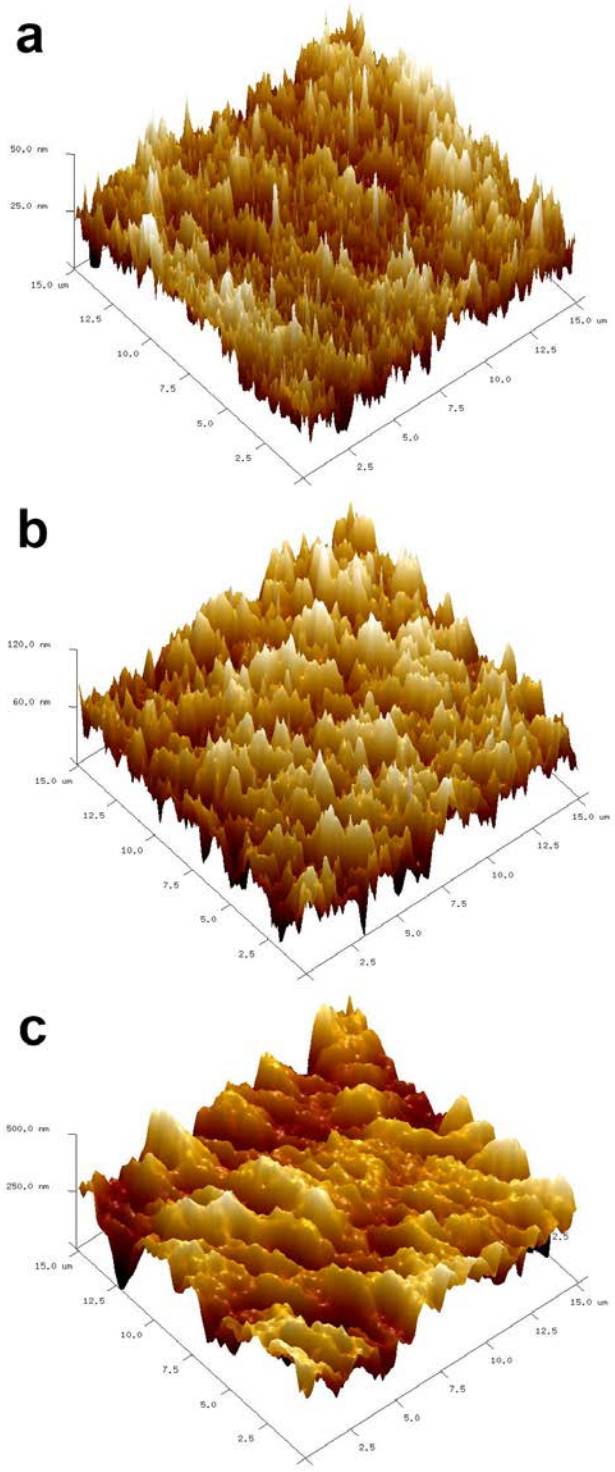


Figure 4.6: 3D AFM images of phage films derived from different phage concentrations. a) 10^{12}, b) 10^{13} and c) 10^{14} pfu/ml.

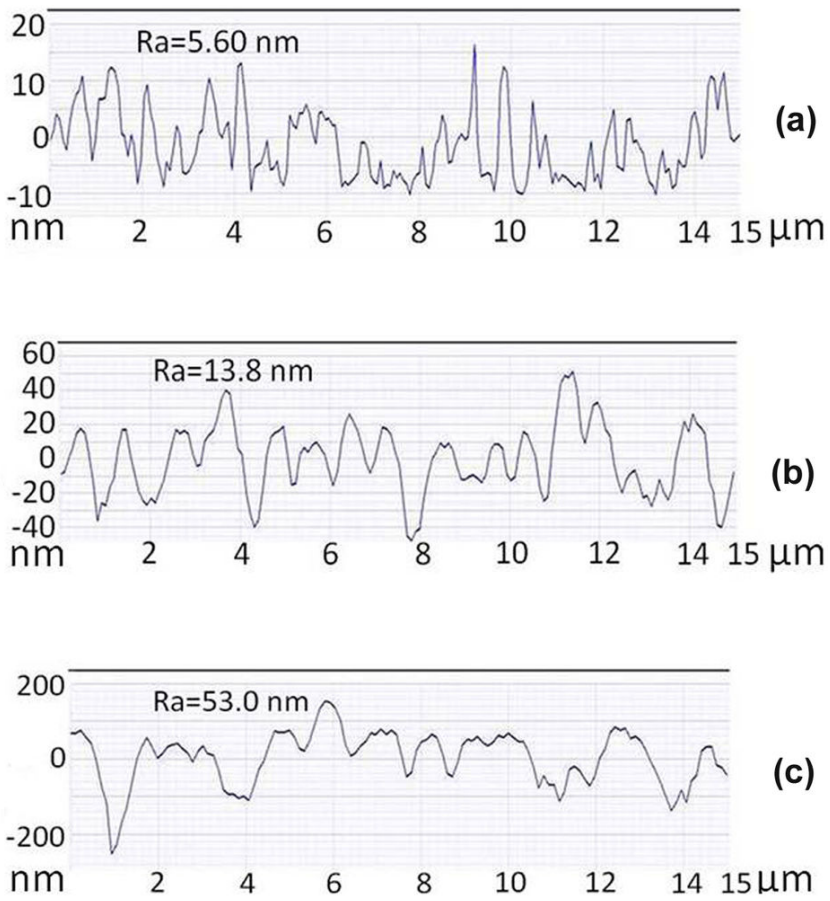


Figure 4.7: The average surface roughness (Ra) of phage-based films derived from the different phage concentrations. The AFM surface line scan profile indicated that the surface roughness of phage films was increased with the rise of phage concentration (a, b and c denoted the phage concentration of 10^{12}, 10^{13} and 10^{14} pfu/ml, respectively).

4.3.3 Cell adhesion on the phage-based films

The rat MSCs were used to evaluate the biological functions of the unique biofilm materials. Our current data confirmed that the ordered ridge/groove structure represented by the phage films significantly induced the elongation and parallel alignment of MSCs along phage bundles in phage-based film materials for all of the peptide sequences displayed on the constituent phage nanofibers (Fig. 4.8a, c and e).

However, cell elongation and alignment were not detected on the phage film derived from higher concentration of phage solution of 10^{14} pfu/ml (Fig. 4.8b, d and f) and the control substrate (i.e., polylysine substrate without phage material) (Fig. 4.9). The significant cell elongation and alignment was also missing if the phage concentration was lower than 10^{12} pfu/ml. Therefore, the optimal concentration of phage solution was defined between 10^{12} pfu/ml and 10^{14} pfu/ml to form the suitable films, which were used to significantly stimulate cell elongation. As shown in Figure 4.5d, on the films assembled from phage at a higher concentration, phage bundles are nearly aligned inside a domain with a size (20–25 μm) comparable to MSCs, however, the orientation of phage bundles between neighboring domains is different. Namely, the direction of elongation of phage bundles in different domains is different and the parallel alignment of nanofibers is only confined in a domain with size similar to MSCs. As a result, the MSCs growing on the films assembled from a higher concentration of phage are not oriented and aligned. Moreover, in the absence of phage bundles, the cells were completely randomly oriented due to the lack of contact guidance by the phage bundles. Therefore, the morphological changes and parallel alignments of MSCs on the phage-based film materials were mainly stimulated by the unique ordered ridge/groove surface topography but not by the peptide sequences displayed on the surface.

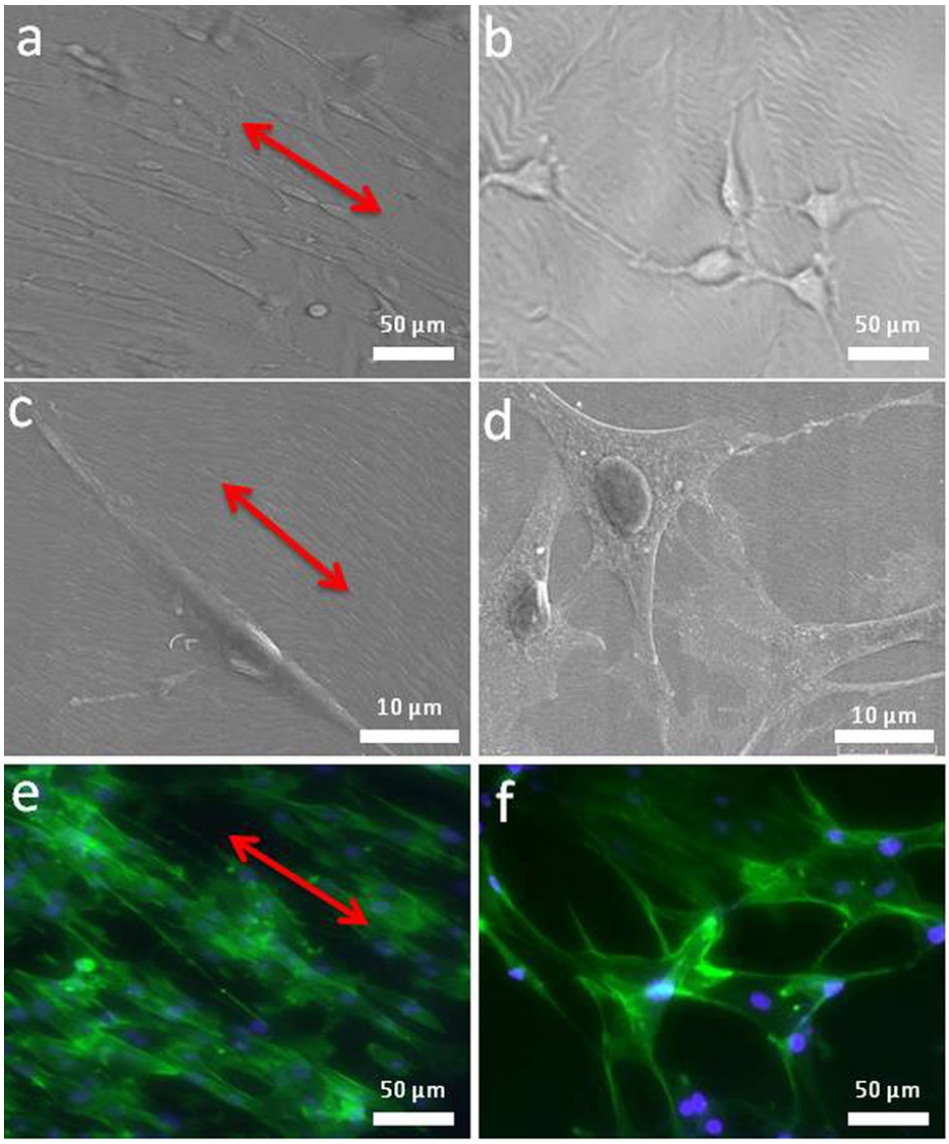


Figure 4.8: Cell adhesion on the phage-based film derived from both low (a, c, e) and high (b, d, f) phage concentration. The MSCs on the phage-based film derived from the low phage concentration (10^{12} pfu/ml) were significantly elongated and aligned along phage bundles (a, c, e) whereas those on the phage-based film derived from the high phage concentration (10^{14} pfu/ml) were randomly oriented and not elongated (b, d, f). Images shown were taken from bright field optical microscopy (a, b), SEM (c, d) and fluorescence microscopy (e, f). Cell nuclei were stained by DAPI (blue) and F-actin were stained by FITC-labeled phalloidin (green).

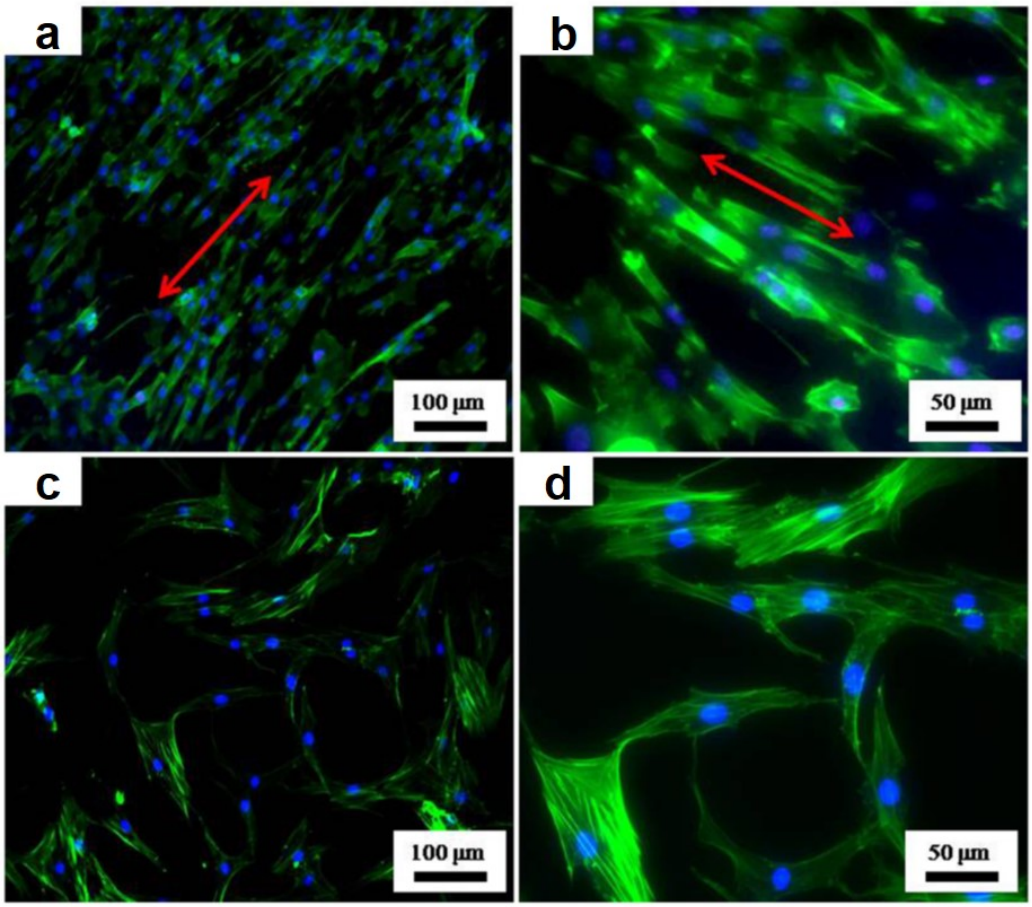


Figure 4.9: Cell morphologies of MSCs on different substrates. Cell alignment could be obviously observed in a large field on the WT-phage film materials (A, B). There was no obvious cell alignment on the control substrate made of the polylysine without phage (C, D). Cell nuclei were stained by DAPI (blue) and F-actin were stained by FITC-labeled phalloidin (green).

4.3.4 Cell proliferation and differentiation on the phage-based films

We proceeded to investigate cell proliferation on the films derived from phage nanofibers with different concentrations and peptides displayed. MTT results demonstrated that cell proliferation was influenced by both the peptide sequences displayed on the constituent phage nanofibers and the concentrations of the phage

solution (Fig. 4.10). Since the phage concentration influenced the size and separation of phage bundles to modulate the nanotopographical cues and the peptide sequences displayed on phage represented the biochemical cues, this fact implied that the cell proliferation was controlled by both topographical and biochemical cues.

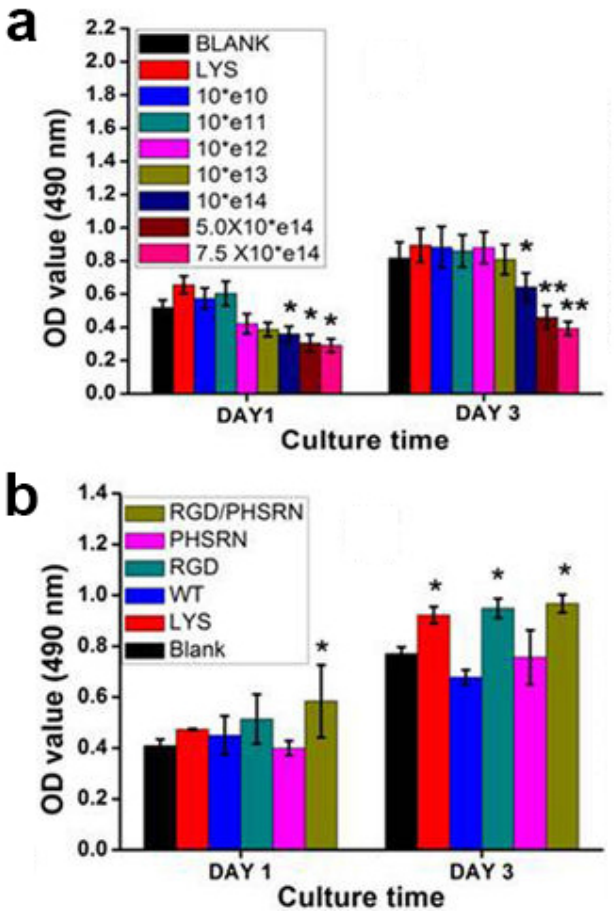


Figure 4.10: Cell proliferation on the phage-based materials. Cell proliferation was significantly influenced by phage concentration (a) and phage types (b). WT, RGD, PHSRN and RGD/PHSRN denoted films made of wild type phage, RGD-displayed phage, PHSRN-displayed phage, and a mixture of RGD- and PHSRN-displayed phage, respectively. CON and LYS denoted poly-L-lysine substrates without phage. BLANK denoted pure glass substrate. All data represented the mean ± standard deviation (n = 3, * $p<0.05$, **$p<0.01$).

To investigate the osteoblastic differentiation of MSCs on the phage-based film materials, the cell-materials were cultured in primary media for 2 weeks. Immunofluorescence staining as a qualitative analysis at the protein level was used to verify the differentiation status. We found that osteocalcin (OCN) and osteopontin (OPN), the two osteogenesis-specific markers, presented positive staining on all materials in the primary media (Fig. 4.11). The OCN and OPN exbihited a higher expression on all phage-based materials than that on the control (poly-L-lysine substrate without phage film). Collagen I (COL) as a positive control of non-osteogenic marker showed high expression on all materials, and there was no significant difference between phage-based and control groups.

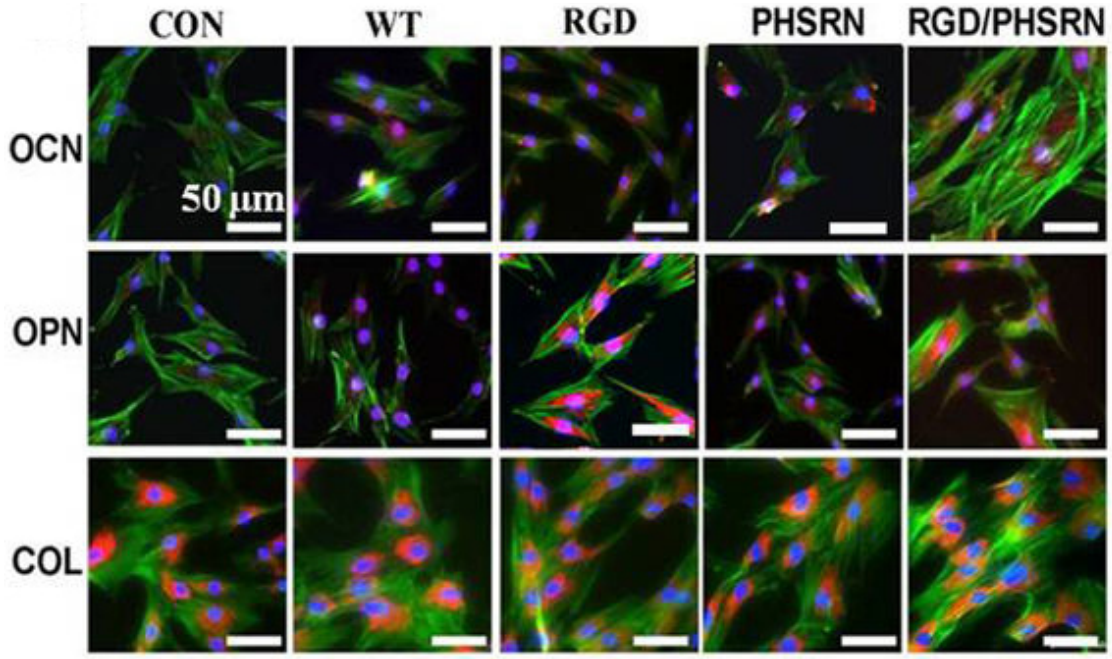


Figure 4.11: Cell differentiation through immunofluorescence staining. OCN, OPN and COL were stained by rhodamine-labeled antibody (red) and cell nuclei were stained by DAPI (blue) and F-actin were stained by FITC-labeled phalloidin (green).

Real-time polymerase chain reaction (PCR) assay was used to further analyze the relative gene level of the osteogenic markers associated with MSCs differentiation on the phage-based materials in the primary media (Fig. 4.12). Both OCN and OPN genes were found to show significant up regulation on the phage-based film materials compared to the control group. Among the different engineered phage nanofibers, RGD/PHSRN-phage presented an extremely high mRNA level of the two osteogenesis-specific proteins (OCN and OPN) in comparison to the control group (**, $p < 0.01$). RGD-phage, PHSRN-phage and WT-phage showed higher expression of OCN and OPN genes than the control (*, $p < 0.05$). However, COL gene as a non-specific osteogenic marker did not show significant difference between phage-based materials and the control. Overall, the phage-based materials enabled to induce the osteoblastic differentiation of MSCs in the primary media without any osteogenic supplements.

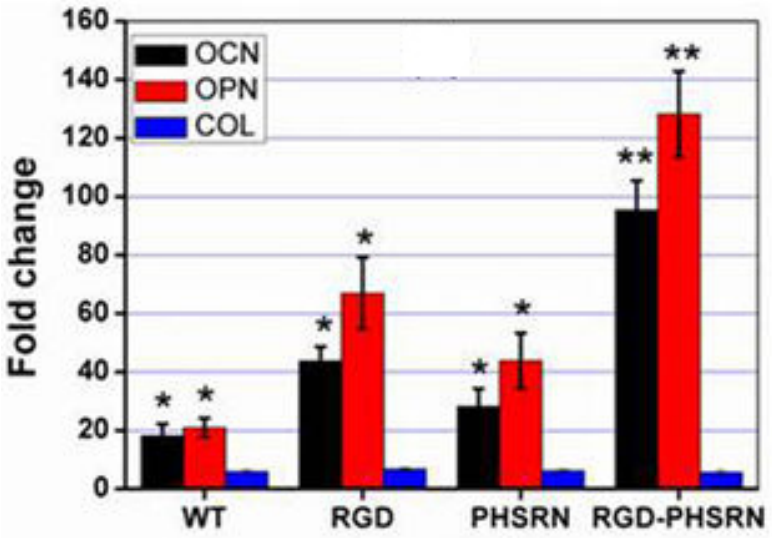


Figure 4.12: Cell differentiation through real-time PCR. Cell differentiation was regulated by different peptides displayed on the engineered phage types. All data represented the mean ± standard deviation (n = 3, * $p<0.05$, **$p<0.01$).

ALP as a marker protein specific for the osteoprogenitor activity was normally used to verify the osteoblastic differentiation of MSCs. The ALP assay demonstrated that both phage-based material and control groups showed positive ALP expression (Fig. 4.13). However, the group of RGD/PHSRN-phage presented the highest ALP activity among all groups. This result suggested the RGD/PHSRN-phage with unique nanotopography promoted the osteoblastic differentiation of MSCs, suggesting a synergetic enhancement by both the biochemical and topographical cues.

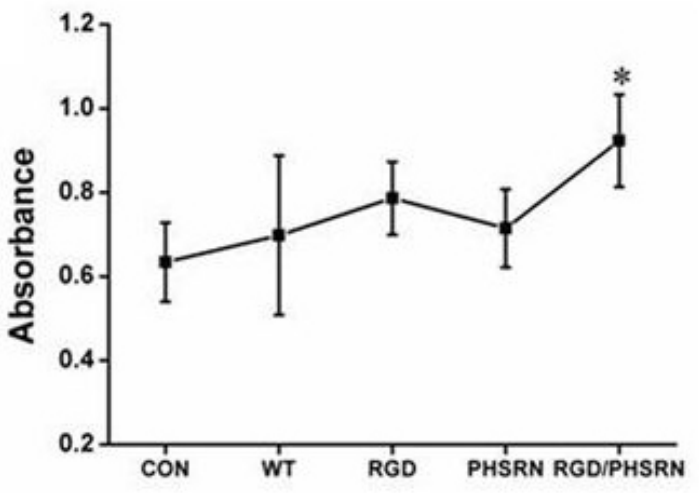


Figure 4.13: ALP activity assay. It is further demonstrated that the osteoblastic differentiation of MSCs was induced by phage-based film materials. All data represented the mean ± standard deviation (n = 3, * $p<0.05$, ** $p<0.01$).

4.4 Discussion and Conclusion

Compared to other nanofibers, M13 phage is unique because it can not only be used as a building block to build unique ridge/groove structures through self-assembly, but also introduce different peptides on the constituent building block into the resultant ridge/groove structures by the well-established phage display technique.[94, 98] This unique property of phage enables us to systematically study the effect of different

peptides on the substrates with constant topography on the stem cell fate. In this study, we constructed different recombinant engineered phages to display adhesive signaling peptide of RGD and PHSRN derived from fibronectin, respectively. Both RGD and PHSRN motifs have been identified as pervasive adhesive peptides to mediate multiple cell activities including cell adhesion, proliferation and differentiation,[175, 177-180] and have been widely used to design the smart biomaterials. Traditionally, such peptides are physically mixed into or chemically immobilized onto biomaterials, preventing us from forming aECM with ordered assembly of peptides and varying only the peptide sequences without changing topography in studying stem cell fates. Therefore, phage display is a unique approach to studying stem cell fate because it allows us to precisely introduce foreign peptide into a nanotopography by genetic means and the nanotopography can be generated by its self-assembly behavior. In addition, the fact that the self-assembly of phage is not affected by the peptide displayed on its surface makes it possible to form an ECM with different peptides but a constant nanotopography for us to systematically study the effect of peptide cues on the stem cell behavior.

M13 phage as a natural nanofiber (~880 nm by 6.6 nm) can be assembled into bundles due to its long-rod structure and monodispersity.[98, 184] The phage bundles can be further aligned to form phage-based 2-D film materials through two driving forces. One is the liquid crystalline assembly at the air-liquid interface during the evaporation process,[93-94, 185] another is the electrostatic interaction between negatively chargely phage nanofibers and positively chargely polylysine. As a result, an ECM was produced with a unique highly ordered topography where phage bundles as ridges are parallel to

each other and separated by grooves (Fig. 4.4). In addition, tuning the concentration of the phage suspension used for self-assembly on the substrate can control the size and surface roughness of phage bundles constituting the film (Fig. 4.5, 4.6 and 4.7).

It has been reported that the topography of culture substrate influences the cell behaviors by elongating cell shape.[167, 186-188] Dalby et al demonstrated that the topographical cue based on the use of disordered nanopits in the polymethylmethacrylate (PMMA) substrate can stimulate the osteoblastic differentiation of human MSCs without the osteogenic supplements.[189] The mechanism might be that the disordered nanopits resulted in longer adhesion, which impacts cytoskeleton tension. These changes in adhesion and cytoskeleton tension will have an effect on cell behavior through an indirect mechanotransductive pathway. Moreover, Jin et al showed that the topographical cue generated from the nanotubular-shaped titanium oxide regulated the osteogenic differentiation of hMSCs.[167] The possible mechanism is that topography-induced cell elongation stimulates the stem cell differentiation. Our current data also confirm that the ordered ridge/groove structure represented by the phage films significantly induced the elongation and parallel alignment of MSCs along phage bundles in phage-based film materials for all of the peptide sequences displayed on the constituent phage nanofibers. Therefore, the morphological changes of MSCs on phage-based film materials might further stimulate the mechanical difference of cytoskeleton, which plays a pivotal role in regulating mechanotransductive pathways and finally having an impact on multiple stem cell behaviors.[187] Although different topographical cues including nano-pits,[189] nano-tube[167] or nano-bundle (our work) are designed on the different substrates, including polymer (PMMA),[189] metal (TiO_2)[167] and

biomolecule (phage), respectively, to stimulate stem cell behavior, the nature of regulatory mechanism might be similar. That is, cell shape is changed by modulating cell adhesion on the substrate materials and finally stem cell fate is directed by biomechanical difference or mechanotransductive pathway.

The MTT result demonstrates that cell proliferation is influenced by both the peptide sequences displayed on the constituent phage nanofibers and the concentrations of the phage nanofibers (Fig. 4.10). Since the phage concentration influences the size and separation of phage bundles to modulate the nanotopographical cues and the peptide sequences displayed on phage represents the biochemical cues, we can conclude that stem cell morphology and alignment are solely modulated by the topographical cue, whereas the cell proliferation is directed by both topographical and biochemical cues.

In order to further understand the effect of both topographical and biochemical cues on cell differentiation, we design a culture system using primary media to elucidate which factor influence stem cell differentiation. It is widely demonstrated that the osteogenic differentiation media as a chemical stimulation plays a key role in enhancing osteoblastic differentiation of multiple stem cells including embryonic stem cells, induced pluripotent stem cells and adult stem cells.[190-192] Our results confirmed that the successful induction of osteoblastic differentiation can be performed in the media without any osteogenic supplements (Fig. 4.11 and 4.12). This fact means that the material itself can direct the osteoblastic differentiation of MSCs through its topographical and biochemical features in the absence of osteogenic supplements. RGD and PHSRN motifs derived from fibronectin, which is a major adhesive component in the natural ECM, have been widely demonstrated to mediate the stem cell behaviors

through specific integrin signal pathway.[193] The osteoprogenitor cells expressed some integrins, including $\alpha_5\beta_1$ specifically binding with RGD and RGD-PHSRN, to regulate osteoblast survival, proliferation, osteogenic gene expression and matrix mineralization.[175, 179] Our results showed that a combination of RGD and PHSRN presented on a unique ridge/groove nanotopography significantly enhanced osteoblastic differentiation (Fig. 4.11 and 4.12). Therefore, the osteoblastic differentiation of MSCs on the phage-based film were significantly stimulated by both topographical and biochemical cues.

In conclusion, designing materials to direct stem cell fate has a profound impact on stem cell biology and provides insights that will facilitate the clinical application of stem cells in modern regenerative medicine. In this study, a virus-activated aECM with controlled biochemical and topographical cues was precisely designed to mediate stem cell behavior. This specific aECM is characteristic of highly ordered topography with aligned ridge/groove nanostructures, which result from the self-assembly of phage nanofibers, and simultaneously presents the biochemical signals made of RGD and PHSRN peptides by phage display technique. The current data demonstrate that cell alignment and elongation are mainly regulated by topographical cues. Cell proliferation are greatly influenced via a combination of topographical and biochemcial cues. Due to the presence of the unique ridge/groove nanostructure made of phage nanofibers and the fibronectin derived peptides displayed on the phage nanofibers, the aECM can stimulate the osteoblastic differentiation of MSCs in the primary media without osteogenic supplements. Our findings suggest that a proper combination of unique nanotopographical and biochemical cues can control the stem cell behaviors including

induction of the osteoblastic differentiation. Our phage display approach represents a novel strategy for generating a virus-activated aECM, where peptide sequences can be systematically tuned on a unique, constant nanotopography by genetic means, for probing the biochemical cues in directing stem cell fate.

References

1. Venugopal, J.; Low, S.; Choon, A. T.; Kumar, A. B.; Ramakrishna, S., Electrospun-modified nanofibrous scaffolds for the mineralization of osteoblast cells. *J Biomed Mater Res A* **2008,** *85A* (2), 408-417.

2. Kim, G. M.; Wutzler, A.; Radusch, H. J.; Michler, G. H.; Simon, P.; Sperling, R. A.; Parak, W. J., One-dimensional arrangement of gold nanoparticles by electrospinning. *Chem Mater* **2005,** *17* (20), 4949-4957.

3. Lu, X. F.; Zhao, Y. Y.; Wang, C., Fabrication of PbS nanoparticles in polymer-fiber matrices by electrospinning. *Adv Mater* **2005,** *17* (20), 2485-2488.

4. Zhang, H. F.; Hussain, I.; Brust, M.; Butler, M. F.; Rannard, S. P.; Cooper, A. I., Aligned two- and three-dimensional structures by directional freezing of polymers and nanoparticles. *Nat Mater* **2005,** *4* (10), 787-793.

5. Segman-Magidovich, S.; Grisaru, H.; Gitli, T.; Levi-Kalisman, Y.; Rapaport, H., Matrices of acidic beta-sheet peptides as templates for calcium phosphate mineralization. *Adv Mater* **2008,** *20* (11), 2156-2161.

6. Warner, M. G.; Hutchison, J. E., Linear assemblies of nanoparticles electrostatically organized on DNA scaffolds. *Nat Mater* **2003,** *2* (4), 272-277.

7. Sharma, J.; Chhabra, R.; Cheng, A.; Brownell, J.; Liu, Y.; Yan, H., Control of self-assembly of DNA tubules through integration of gold nanoparticles. *Science* **2009,** *323* (5910), 112-116.

8. Zhang, S. G., Fabrication of novel biomaterials through molecular self-assembly. *Nat Biotechnol* **2003,** *21* (10), 1171-1178.

9. Archibald, D. D.; Mann, S., Template Mineralization of Self-Assembled Anisotropic Lipid Microstructures. *Nature* **1993,** *364* (6436), 430-433.

10. Shenton, W.; Pum, D.; Sleytr, U. B.; Mann, S., Synthesis of cadmium sulphide superlattices using self-assembled bacterial S-layers. *Nature* **1997,** *389* (6651), 585-587.

11. Klaus, T.; Joerger, R.; Olsson, E.; Granqvist, C. G., Silver-based crystalline nanoparticles, microbially fabricated. *P Natl Acad Sci USA* **1999,** *96* (24), 13611-13614.

12. Mao, C.; Flynn, C. E.; Hayhurst, A.; Sweeney, R.; Qi, J.; Georgiou, G.; Iverson, B.; Belcher, A. M., Viral assembly of oriented quantum dot nanowires. *P Natl Acad Sci USA* **2003,** *100* (12), 6946-6951.

13. Mao, C.; Solis, D. J.; Reiss, B. D.; Kottmann, S. T.; Sweeney, R. Y.; Hayhurst, A.; Georgiou, G.; Iverson, B.; Belcher, A. M., Virus-based toolkit for the directed synthesis of magnetic and semiconducting nanowires. *Science* **2004,** *303* (5655), 213-217.

14. Yonekura, K.; Maki-Yonekura, S.; Namba, K., Complete atomic model of the bacterial flagellar filament by electron cryomicroscopy. *Nature* **2003,** *424* (6949), 643-650.

15. Gekko, K.; Hasegawa, Y., Compressibility Structure Relationship of Globular-Proteins. *Biochemistry-Us* **1986,** *25* (21), 6563-6571.

16. Oosawa, F.; Fujime, S.; Ishiwata, S.; Mihashi, K., Dynamic Property of F-Actin and Thin Filament. *Cold Spring Harb Sym* **1973,** *37*, 277-285.

17. Darnton, N. C.; Berg, H. C., Force-extension measurements on bacterial flagella: Triggering polymorphic transformations. *Biophys J* **2007,** *92* (6), 2230-2236.

18. Samatey, F. A.; Imada, K.; Nagashima, S.; Vonderviszt, F.; Kumasaka, T.; Yamamoto, M.; Namba, K., Structure of the bacterial flagellar protofilament and implications for a switch for supercoiling. *Nature* **2001,** *410* (6826), 331-337.

19. Li, D.; Qu, X. W.; Newton, S. M. C.; Klebba, P. E.; Mao, C. B., Morphology-controlled synthesis of silica nanotubes through pH- and sequence-responsive morphological change of bacterial flagellar biotemplates. *J Mater Chem* **2012,** *22* (31), 15702-15709.

20. Li, D.; Newton, S. M.; Klebba, P. E.; Mao, C., Flagellar display of bone-protein-derived peptides for studying peptide-mediated biomineralization. *Langmuir* **2012,** *28* (47), 16338-16346.

21. Wang, F. K.; Li, D.; Mao, C. B., Genetically Modifiable Flagella as Templates for Silica Fibers: From Hybrid Nanotubes to 1D Periodic Nanohole Arrays. *Advanced Functional Materials* **2008,** *18* (24), 4007-4013.

22. Wang, F. K.; Nimmo, S. L.; Cao, B. R.; Mao, C. B., Oxide formation on biological nanostructures via a structure-directing agent: towards an understanding of precise structural transcription. *Chem Sci* **2012,** *3* (8), 2639-2645.

23. Westerlund-Wikstrom, B.; Tanskanen, J.; Virkola, R.; Hacker, J.; Lindberg, M.; Skurnik, M.; Korhonen, T. K., Functional expression of adhesive peptides as fusions to Escherichia coli flagellin. *Protein Eng* **1997,** *10* (11), 1319-1326.

24. Lowy, J.; Mcdonough, M. W., Structure of Filaments Produced by Re-Aggregation of Salmonella Flagellin. *Nature* **1964,** *204* (495), 125-127.

25. Hasegawa, E.; Kamiya, R.; Asakura, S., Thermal Transition in Helical Forms of Salmonella Flagella. *J Mol Biol* **1982,** *160* (4), 609-621.

26. Shenton, W.; Douglas, T.; Young, M.; Stubbs, G.; Mann, S., Inorganic-organic nanotube composites from template mineralization of tobacco mosaic virus. *Adv Mater* **1999,** *11* (3), 253-256.

27. Steinmetz, N. F.; Shah, S. N.; Barclay, J. E.; Rallapalli, G.; Lomonossoff, G. P.; Evans, D. J., Virus-Templated Silica Nanoparticles. *Small* **2009,** *5* (7), 813-816.

28. Efimov, V. P.; Nepluev, I. V.; Mesyanzhinov, V. V., Bacteriophage-T4 as a Surface Display Vector. *Virus Genes* **1995,** *10* (2), 173-177.

29. Ren, Z. J.; Lewis, G. K.; Wingfield, P. T.; Locke, E. G.; Steven, A. C.; Black, L. W., Phage display of intact domains at high copy number: A system based on SOC, the small outer capsid protein of bacteriophage T4. *Protein Sci* **1996,** *5* (9), 1833-1843.

30. Sternberg, N.; Hoess, R. H., Display of Peptides and Proteins on the Surface of Bacteriophage-Lambda. *P Natl Acad Sci USA* **1995,** *92* (5), 1609-1613.

31. Smith, G. P.; Petrenko, V. A., Phage display. *Chemical reviews* **1997,** *97* (2), 391-410.

32. Kehoe, J. W.; Kay, B. K., Filamentous phage display in the new millennium. *Chemical reviews* **2005,** *105* (11), 4056-4072.

33. Dogic, Z.; Fraden, S., Ordered phases of filamentous viruses. *Curr Opin Colloid In* **2006,** *11* (1), 47-55.

34. Krag, D. N.; Shukla, G. S.; Shen, G. P.; Pero, S.; Ashikaga, T.; Fuller, S.; Weaver, D. L.; Burdette-Radoux, S.; Thomas, C., Selection of tumor-binding ligands in cancer patients with phage display libraries. *Cancer Res* **2006,** *66* (15), 7724-7733.

35. Sarikaya, M.; Tamerler, C.; Schwartz, D. T.; Baneyx, F., Materials Assembly and Formation Using Engineered Polypeptides. *Annual Review of Materials Research* **2004,** *34* (1), 373-408.

36. Huang, W. Z.; Petrosino, J.; Palzkill, T., Display of functional beta-lactamase inhibitory protein on the surface of M13 bacteriophage. *Antimicrob Agents Ch* **1998,** *42* (11), 2893-2897.

37. Lee, S. K.; Yun, D. S.; Belcher, A. M., Cobalt ion mediated self-assembly of genetically engineered bacteriophage for biomimetic Co-Pt hybrid material. *Biomacromolecules* **2006,** *7* (1), 14-17.

38. Nam, K. T.; Wartena, R.; Yoo, P. J.; Liau, F. W.; Lee, Y. J.; Chiang, Y. M.; Hammond, P. T.; Belcher, A. M., Stamped microbattery electrodes based on self-assembled M13 viruses. *P Natl Acad Sci USA* **2008,** *105* (45), 17227-17231.

39. Hufton, S. E.; Moerkerk, P. T.; Meulemans, E. V.; de Bruine, A.; Arends, J. W.; Hoogenboom, H. R., Phage display of cDNA repertoires: the pVI display system and its applications for the selection of immunogenic ligands. *J Immunol Methods* **1999,** *231* (1-2), 39-51.

40. Gao, C. S.; Mao, S. L.; Kaufmann, G.; Wirsching, P.; Lerner, R. A.; Janda, K. D., A method for the generation of combinatorial antibody libraries using pIX phage display. *P Natl Acad Sci USA* **2002,** *99* (20), 12612-12616.

41. Lee, Y. J.; Yi, H.; Kim, W. J.; Kang, K.; Yun, D. S.; Strano, M. S.; Ceder, G.; Belcher, A. M., Fabricating Genetically Engineered High-Power Lithium-Ion Batteries Using Multiple Virus Genes. *Science* **2009,** *324* (5930), 1051-1055.

42. Chen, L. M.; Zurita, A. J.; Ardelt, P. U.; Giordano, R. J.; Arap, W.; Pasqualini, R., Design and validation of a bifunctional ligand display system for receptor targeting. *Chem Biol* **2004,** *11* (8), 1081-1091.

43. Lee, Y. J.; Lee, Y.; Oh, D.; Chen, T.; Ceder, G.; Belcher, A. M., Biologically Activated Noble Metal Alloys at the Nanoscale: For Lithium Ion Battery Anodes. *Nano Lett* **2010,** *10* (7), 2433-2440.

44. Nam, K. T.; Peelle, B. R.; Lee, S. W.; Belcher, A. M., Genetically driven assembly of nanorings based on the M13 virus. *Nano Lett* **2004,** *4* (1), 23-27.

45. Sunderland, K. S.; Yang, M.; Mao, C., Phage-Enabled Nanomedicine: From Probes to Therapeutics in Precision Medicine. *Angewandte Chemie* **2017,** *56* (8), 1964-1992.

46. Yang, M.; Sunderland, K.; Mao, C., Virus-Derived Peptides for Clinical Applications. *Chemical reviews* **2017,** *117* (15), 10377-10402.

47. Cao, B. R.; Yang, M. Y.; Mao, C. B., Phage as a Genetically Modifiable Supramacromolecule in Chemistry, Materials and Medicine. *Accounts Chem Res* **2016,** *49* (6), 1111-1120.

48. Naik, R. R.; Jones, S. E.; Murray, C. J.; McAuliffe, J. C.; Vaia, R. A.; Stone, M. O., Peptide templates for nanoparticle synthesis derived from polymerase chain reaction-driven phage display. *Advanced Functional Materials* **2004,** *14* (1), 25-30.

49. Li, Y. J.; Whyburn, G. P.; Huang, Y., Specific Peptide Regulated Synthesis of Ultrasmall Platinum Nanocrystals. *J Am Chem Soc* **2009,** *131* (44), 15998-15999.

50. Nam, Y. S.; Magyar, A. P.; Lee, D.; Kim, J. W.; Yun, D. S.; Park, H.; Pollom, T. S.; Weitz, D. A.; Belcher, A. M., Biologically templated photocatalytic nanostructures for sustained light-driven water oxidation. *Nature Nanotechnology* **2010,** *5* (5), 340-344.

51. Whaley, S. R.; English, D. S.; Hu, E. L.; Barbara, P. F.; Belcher, A. M., Selection of peptides with semiconductor binding specificity for directed nanocrystal assembly. *Nature* **2000,** *405* (6787), 665-668.

52. Flynn, C. E.; Mao, C. B.; Hayhurst, A.; Williams, J. L.; Georgiou, G.; Iverson, B.; Belcher, A. M., Synthesis and organization of nanoscale II-VI semiconductor materials using evolved peptide specificity and viral capsid assembly. *J Mater Chem* **2003,** *13* (10), 2414-2421.

53. Dang, X. N.; Yi, H. J.; Ham, M. H.; Qi, J. F.; Yun, D. S.; Ladewski, R.; Strano, M. S.; Hammond, P. T.; Belcher, A. M., Virus-templated self-assembled single-walled carbon nanotubes for highly efficient electron collection in photovoltaic devices. *Nature Nanotechnology* **2011,** *6* (6), 377-384.

54. Cui, Y.; Kim, S. N.; Jones, S. E.; Wissler, L. L.; Naik, R. R.; McAlpine, M. C., Chemical Functionalization of Graphene Enabled by Phage Displayed Peptides. *Nano Lett* **2010,** *10* (11), 4559-4565.

55. Sanghvi, A. B.; Miller, K. P. H.; Belcher, A. M.; Schmidt, C. E., Biomaterials functionalization using a novel peptide that selectively binds to a conducting polymer. *Nat Mater* **2005,** *4* (6), 496-502.

56. Serizawa, T.; Sawada, T.; Matsuno, H.; Matsubara, T.; Sato, T., A peptide motif recognizing a polymer stereoregularity. *J Am Chem Soc* **2005,** *127* (40), 13780-13781.

57. Lee, S. W.; Wood, B. M.; Belcher, A. M., Chiral smectic C structures of virus-based films. *Langmuir : the ACS journal of surfaces and colloids* **2003,** *19* (5), 1592-1598.

58. Tang, J. X.; Fraden, S., Isotropic-Cholesteric Phase-Transition in Colloidal Suspensions of Filamentous Bacteriophage-Fd. *Liq Cryst* **1995,** *19* (4), 459-467.

59. Dogic, Z.; Fraden, S., Cholesteric phase in virus suspensions. *Langmuir : the ACS journal of surfaces and colloids* **2000,** *16* (20), 7820-7824.

60. Neltner, B.; Peddie, B.; Xu, A.; Doenlen, W.; Durand, K.; Yun, D. S.; Speakman, S.; Peterson, A.; Belcher, A., Production of Hydrogen Using Nanocrystalline Protein-Templated Catalysts on M13 Phage. *Acs Nano* **2010,** *4* (6), 3227-3235.

61. Nam, K. T.; Kim, D. W.; Yoo, P. J.; Chiang, C. Y.; Meethong, N.; Hammond, P. T.; Chiang, Y. M.; Belcher, A. M., Virus-enabled synthesis and assembly of nanowires for lithium ion battery electrodes. *Science* **2006,** *312* (5775), 885-888.

62. Liu, A. H.; Abbineni, G.; Moo, C. B., Nanocomposite Films Assembled from Genetically Engineered Filamentous Viruses and Gold Nanoparticles: Nanoarchitecture- and Humidity-Tunable Surface Plasmon Resonance Spectra. *Adv Mater* **2009,** *21* (9), 1001-1005.

63. Souza, G. R.; Christianson, D. R.; Staquicini, F. I.; Ozawa, M. G.; Snyder, E. Y.; Sidman, R. L.; Miller, J. H.; Arap, W.; Pasqualini, R., Networks of gold nanoparticles and bacteriophage as biological sensors and cell-targeting agents. *P Natl Acad Sci USA* **2006,** *103* (5), 1215-1220.

64. Meegan, J. E.; Aggeli, A.; Boden, N.; Brydson, R.; Brown, A. P.; Carrick, L.; Brough, A. R.; Hussain, A.; Ansell, R. J., Designed self-assembled beta-sheet peptide fibrils as templates for silica nanotubes. *Advanced Functional Materials* **2004,** *14* (1), 31-37.

65. Ono, Y.; Kanekiyo, Y.; Inoue, K.; Hojo, J.; Nango, M.; Shinkai, S., Preparation of novel hollow fiber silica using collagen fibers as a template. *Chem Lett* **1999,** (6), 475-476.

66. Behrens, S.; Wu, J.; Habicht, W.; Unger, E., Silver nanoparticle and nanowire formation by microtubule templates. *Chem Mater* **2004,** *16* (16), 3085-3090.

67. Kumara, M. T.; Tripp, B. C.; Muralidharan, S., Exciton energy transfer in self-assembled quantum dots on bioengineered bacterial flagella nanotubes. *J Phys Chem C* **2007,** *111* (14), 5276-5280.

68. Kumara, M. T.; Muralidharan, S.; Tripp, B. C., Generation and characterization of inorganic and organic nanotubes on bioengineered flagella of mesophilic bacteria. *J Nanosci Nanotechno* **2007,** *7* (7), 2260-2272.

69. Hesse, W. R.; Luo, L. L.; Zhang, G. N.; Mulero, R.; Cho, J. H.; Kim, M. J., Mineralization of flagella for nanotube formation. *Mat Sci Eng C-Mater* **2009,** *29* (7), 2282-2286.

70. Kumara, M. T.; Tripp, B. C.; Muralidharan, S., Self-assembly of metal nanoparticles and nanotubes on bioengineered flagella scaffolds. *Chem Mater* **2007,** *19* (8), 2056-2064.

71. Jo, W.; Freedman, K. J.; Yi, D. K.; Kim, M. J., Fabrication of tunable silica-mineralized nanotubes using flagella as bio-templates. *Nanotechnology* **2012,** *23* (5), 055601.

72. Jo, W.; Freedman, K. J.; Kim, M. J., Metallization of biologically inspired silica nanotubes. *Mat Sci Eng C-Mater* **2012,** *32* (8), 2426-2430.

73. Jo, W.; Darmawan, M.; Kim, J.; Ahn, C. W.; Byun, D.; Baik, S. H.; Kim, M. J., Electrical property measurements of metallized flagella-templated silica nanotube networks. *Nanotechnology* **2013,** *24* (13), 135704.

74. Asakura, S., Polymerization of flagellin and polymorphism of flagella. *Adv Biophys* **1970,** *1*, 99-155.

75. Naik, R. R.; Stringer, S. J.; Agarwal, G.; Jones, S. E.; Stone, M. O., Biomimetic synthesis and patterning of silver nanoparticles. *Nat Mater* **2002,** *1* (3), 169-172.

76. Umetsu, M.; Mizuta, M.; Tsumoto, K.; Ohara, S.; Takami, S.; Watanabe, H.; Kumagai, I.; Adschiri, T., Bioassisted room-temperature immobilization and mineralization of zinc oxide - The structural ordering of ZnO nanoparticles into a flower-type morphology. *Adv Mater* **2005,** *17* (21), 2571-2575.

77. Mao, C. B.; Solis, D. J.; Reiss, B. D.; Kottmann, S. T.; Sweeney, R. Y.; Hayhurst, A.; Georgiou, G.; Iverson, B.; Belcher, A. M., Virus-based toolkit for the directed synthesis of magnetic and semiconducting nanowires. *Science* **2004,** *303* (5655), 213-217.

78. Avery, K. N.; Schaak, J. E.; Schaak, R. E., M13 Bacteriophage as a Biological Scaffold for Magnetically-Recoverable Metal Nanowire Catalysts: Combining Specific and Nonspecific Interactions To Design Multifunctional Nanocomposites. *Chem Mater* **2009,** *21* (11), 2176-2178.

79. Lee, Y. J.; Belcher, A. M., Nanostructure design of amorphous FePO4 facilitated by a virus for 3 V lithium ion battery cathodes. *J Mater Chem* **2011,** *21* (4), 1033-1039.

80. Perham, R. N.; Wilson, T. M., The characterization of intermediates formed during the disassembly of tobacco mosaic virus at alkaline pH. *Virology* **1978,** *84* (2), 293-302.

81. Niu, Z.; Liu, J.; Lee, L. A.; Bruckman, M. A.; Zhao, D.; Koley, G.; Wang, Q., Biological templated synthesis of water-soluble conductive polymeric nanowires. *Nano Lett* **2007,** *7* (12), 3729-3733.

82. Dujardin, E.; Peet, C.; Stubbs, G.; Culver, J. N.; Mann, S., Organization of metallic nanoparticles using tobacco mosaic virus templates. *Nano Lett* **2003,** *3* (3), 413-417.

83. Knez, M.; Sumser, M.; Bittner, A. M.; Wege, C.; Jeske, H.; Martin, T. P.; Kern, K., Spatially selective nucleation of metal clusters on the tobacco mosaic virus. *Advanced Functional Materials* **2004,** *14* (2), 116-124.

84. Rong, J. H.; Niu, Z. W.; Lee, L. A.; Wang, Q., Self-assembly of viral particles. *Curr Opin Colloid In* **2011,** *16* (6), 441-450.

85. Niu, Z.; Bruckman, M.; Kotakadi, V. S.; He, J.; Emrick, T.; Russell, T. P.; Yang, L.; Wang, Q., Study and characterization of tobacco mosaic virus head-to-tail assembly assisted by aniline polymerization. *Chem Commun* **2006,** (28), 3019-3021.

86. Knez, M.; Bittner, A. M.; Boes, F.; Wege, C.; Jeske, H.; Maiss, E.; Kern, K., Biotemplate synthesis of 3-nm nickel and cobalt nanowires. *Nano Lett* **2003,** *3* (8), 1079-1082.

87. Tsukamoto, R.; Muraoka, M.; Seki, M.; Tabata, H.; Yamashita, I., Synthesis of CoPt and FePt3 nanowires using the central channel of tobacco mosaic virus as a biotemplate. *Chem Mater* **2007,** *19* (10), 2389-2391.

88. Wang, F. K.; Cao, B. R.; Mao, C. B., Bacteriophage Bundles with Prealigned Ca2+ Initiate the Oriented Nucleation and Growth of Hydroxylapatite. *Chem Mater* **2010,** *22* (12), 3630-3636.

89. He, T.; Abbineni, G.; Cao, B. R.; Mao, C. B., Nanofibrous Bio-inorganic Hybrid Structures Formed Through Self-Assembly and Oriented Mineralization of Genetically Engineered Phage Nanofibers. *Small* **2010,** *6* (20), 2230-2235.

90. Mao, C. B.; Wang, F. K.; Cao, B. R., Controlling Nanostructures of Mesoporous Silica Fibers by Supramolecular Assembly of Genetically Modifiable Bacteriophages. *Angew Chem Int Edit* **2012,** *51* (26), 6411-6415.

91. Kumara, M. T.; Srividya, N.; Muralidharan, S.; Tripp, B. C., Bioengineered flagella protein nanotubes with cysteine loops: Self-assembly and manipulation in an optical trap. *Nano Lett* **2006,** *6* (9), 2121-2129.

92. Chung, W. J.; Merzlyak, A.; Yoo, S. Y.; Lee, S. W., Genetically Engineered Liquid-Crystalline Viral Films for Directing Neural Cell Growth. *Langmuir : the ACS journal of surfaces and colloids* **2010,** *26* (12), 9885-9890.

93. Chung, W. J.; Oh, J. W.; Kwak, K.; Lee, B. Y.; Meyer, J.; Wang, E.; Hexemer, A.; Lee, S. W., Biomimetic self-templating supramolecular structures. *Nature* **2011,** *478* (7369), 364-368.

94. Zhu, H. B.; Cao, B. R.; Zhen, Z. P.; Laxmi, A. A.; Li, D.; Liu, S. R.; Mao, C. B., Controlled growth and differentiation of MSCs on grooved films assembled from monodisperse biological nanofibers with genetically tunable surface chemistries. *Biomaterials* **2011,** *32* (21), 4744-4752.

95. Kumara, M. T.; Tripp, B. C.; Muralidharan, S., Layer-by-layer assembly of bioengineered flagella protein nanotubes. *Biomacromolecules* **2007,** *8* (12), 3718-3722.

96. Cao, B. R.; Zhu, Y.; Wang, L.; Mao, C. B., Controlled Alignment of Filamentous Supramolecular Assemblies of Biomolecules into Centimeter-Scale Highly Ordered Patterns by Using Nature-Inspired Magnetic Guidance. *Angew Chem Int Edit* **2013,** *52* (45), 11750-11754.

97. Wang, J. L.; Yang, M. Y.; Zhu, Y.; Wang, L.; Tomsia, A. P.; Mao, C. B., Phage Nanofibers Induce Vascularized Osteogenesis in 3D Printed Bone Scaffolds. *Adv Mater* **2014,** *26* (29), 4961-4966.

98. Merzlyak, A.; Indrakanti, S.; Lee, S. W., Genetically Engineered Nanofiber-Like Viruses For Tissue Regenerating Materials. *Nano Lett* **2009,** *9* (2), 846-852.

99. Souza, G. R.; Yonel-Gumruk, E.; Fan, D.; Easley, J.; Rangel, R.; Guzman-Rojas, L.; Miller, J. H.; Arap, W.; Pasqualini, R., Bottom-Up Assembly of Hydrogels from Bacteriophage and Au Nanoparticles: The Effect of Cis- and Trans-Acting Factors. *Plos One* **2008,** *3* (5), e2242.

100. Chen, P. Y.; Hyder, M. N.; Mackanic, D.; Courchesne, N. M. D.; Qi, J.; Klug, M. T.; Belcher, A. M.; Hammond, P. T., Assembly of Viral Hydrogels for Three-Dimensional Conducting Nanocomposites. *Adv Mater* **2014,** *26* (30), 5101-5107.

101. Mao, C. B.; Liu, A. H.; Cao, B. R., Virus-Based Chemical and Biological Sensing. *Angew Chem Int Edit* **2009,** *48* (37), 6790-6810.

102. Niu, Z. W.; Bruckman, M. A.; Harp, B.; Mello, C. M.; Wang, Q., Bacteriophage M13 as a Scaffold for Preparing Conductive Polymeric Composite Fibers. *Nano Res* **2008,** *1* (3), 235-241.

103. Sunderland, K. S.; Yang, M. Y.; Mao, C. B., Phage-Enabled Nanomedicine: From Probes to Therapeutics in Precision Medicine. *Angew Chem Int Edit* **2017,** *56* (8), 1964-1992.

104. Yi, H. J.; Ghosh, D.; Ham, M. H.; Qi, J. F.; Barone, P. W.; Strano, M. S.; Belcher, A. M., M13 Phage-Functionalized Single-Walled Carbon Nanotubes As Nanoprobes for Second Near-Infrared Window Fluorescence Imaging of Targeted Tumors. *Nano Lett* **2012,** *12* (3), 1176-1183.

105. Ghosh, D.; Lee, Y.; Thomas, S.; Kohli, A. G.; Yun, D. S.; Belcher, A. M.; Kelly, K. A., M13-templated magnetic nanoparticles for targeted in vivo imaging of prostate cancer. *Nature Nanotechnology* **2012,** *7* (10), 677-682.

106. Xia, Y. N.; Yang, P. D.; Sun, Y. G.; Wu, Y. Y.; Mayers, B.; Gates, B.; Yin, Y. D.; Kim, F.; Yan, Y. Q., One-dimensional nanostructures: Synthesis, characterization, and applications. *Adv Mater* **2003,** *15* (5), 353-389.

107. Lee, Y. M.; Kim, Y. H.; Lee, J. H.; Park, J. H.; Park, N. G.; Choe, W. S.; Ko, M. J.; Yoo, P. J., Highly Interconnected Porous Electrodes for Dye-Sensitized Solar Cells Using Viruses as a Sacrificial Template. *Advanced Functional Materials* **2011,** *21* (6), 1160-1167.

108. Royston, E.; Ghosh, A.; Kofinas, P.; Harris, M. T.; Culver, J. N., Self-assembly of virus-structured high surface area nanomaterials and their application as battery electrodes. *Langmuir : the ACS journal of surfaces and colloids* **2008,** *24* (3), 906-912.

109. Chen, X. L.; Gerasopoulos, K.; Guo, J. C.; Brown, A.; Wang, C. S.; Ghodssi, R.; Culver, J. N., Virus-Enabled Silicon Anode for Lithium-Ion Batteries. *Acs Nano* **2010,** *4* (9), 5366-5372.

110. Gerasopoulos, K.; McCarthy, M.; Banerjee, P.; Fan, X.; Culver, J. N.; Ghodssi, R., Biofabrication methods for the patterned assembly and synthesis of viral nanotemplates. *Nanotechnology* **2010,** *21* (5), 055304.

111. Chen, X. L.; Gerasopoulos, K.; Guo, J. C.; Brown, A.; Wang, C. S.; Ghodssi, R.; Culver, J. N., A Patterned 3D Silicon Anode Fabricated by Electrodeposition on a Virus-Structured Current Collector. *Advanced Functional Materials* **2011,** *21* (2), 380-387.

112. Pomerantseva, E.; Gerasopoulos, K.; Chen, X. Y.; Rubloff, G.; Ghodssi, R., Electrochemical performance of the nanostructured biotemplated V2O5 cathode for lithium-ion batteries. *J Power Sources* **2012,** *206*, 282-287.

113. Beznosov, S. N.; Veluri, P. S.; Pyatibratov, M. G.; Chatterjee, A.; MacFarlane, D. R.; Fedorov, O. V.; Mitra, S., Flagellar filament bio-templated inorganic oxide materials - towards an efficient lithium battery anode. *Sci Rep-Uk* **2015,** *5*, 7736.

114. Favier, F.; Walter, E. C.; Zach, M. P.; Benter, T.; Penner, R. M., Hydrogen sensors and switches from electrodeposited palladium mesowire arrays. *Science* **2001,** *293* (5538), 2227-2231.

115. Lee, D.; Choe, Y. J.; Choi, Y. S.; Bhak, G.; Lee, J.; Paik, S. R., Photoconductivity of Pea-Pod-Type Chains of Gold Nanoparticles Encapsulated within Dielectric Amyloid Protein Nanofibrils of alpha-Synuclein. *Angew Chem Int Edit* **2011,** *50* (6), 1332-1337.

116. Maier, S. A.; Brongersma, M. L.; Kik, P. G.; Meltzer, S.; Requicha, A. A. G.; Atwater, H. A., Plasmonics - A route to nanoscale optical devices. *Adv Mater* **2001,** *13* (19), 1501-1505.

117. Maier, S. A.; Kik, P. G.; Atwater, H. A.; Meltzer, S.; Harel, E.; Koel, B. E.; Requicha, A. A. G., Local detection of electromagnetic energy transport below the diffraction limit in metal nanoparticle plasmon waveguides. *Nat Mater* **2003,** *2* (4), 229-232.

118. Su, B.; Wu, Y. C.; Tang, Y.; Chen, Y.; Cheng, W. L.; Jiang, L., Free-Standing 1D Assemblies of Plasmonic Nanoparticles. *Adv Mater* **2013,** *25* (29), 3968-3972.

119. Li, Y.; Cao, B.; Yang, M.; Zhu, Y.; Suh, J.; Mao, C., Identification of Novel Short BaTiO3-Binding/Nucleating Peptides for Phage-Templated in Situ Synthesis of BaTiO3 Polycrystalline Nanowires at Room Temperature. *ACS Applied Materials & Interfaces* **2016,** *8* (45), 30714-30721.

120. Wang, Y. C.; Ju, Z. G.; Cao, B. R.; Gao, X.; Zhu, Y.; Qiu, P. H.; Xu, H.; Pan, P. T.; Bao, H. Z.; Wang, L.; Mao, C. B., Ultrasensitive Rapid Detection of Human Serum Antibody Biomarkers by Biomarker-Capturing Viral Nanofibers. *Acs Nano* **2015,** *9* (4), 4475-4483.

121. Cao, B. R.; Xu, H.; Mao, C. B., Controlled Self-Assembly of Rodlike Bacterial Pili Particles into Ordered Lattices. *Angew Chem Int Edit* **2011,** *50* (28), 6264-6268.

122. Wnek, M.; Gorzny, M. L.; Ward, M. B.; Walti, C.; Davies, A. G.; Brydson, R.; Evans, S. D.; Stockley, P. G., Fabrication and characterization of gold nano-wires templated on virus-like arrays of tobacco mosaic virus coat proteins. *Nanotechnology* **2013,** *24* (2), 025605.

123. Lim, J. S.; Kim, S. M.; Lee, S. Y.; Stach, E. A.; Culver, J. N.; Harris, M. T., Formation of Au/Pd Alloy Nanoparticles on TMV. *J Nanomater* **2010**, 620505.

124. Shah, S. N.; Khan, A. A.; Espinosa, A.; Garcia, M. A.; Nuansing, W.; Ungureanu, M.; Heddle, J. G.; Chuvilin, A. L.; Wege, C.; Bittner, A. M., Virus-Templated Near-Amorphous Iron Oxide Nanotubes. *Langmuir* **2016,** *32* (23), 5899-5908.

125. Wei, Z. Y.; Maeda, Y.; Matsui, H., Discovery of Catalytic Peptides for Inorganic Nanocrystal Synthesis by a Combinatorial Phage Display Approach. *Angew Chem Int Edit* **2011,** *50* (45), 10585-10588.

126. Petrenko, V. A., Evolution of phage display: from bioactive peptides to bioselective nanomaterials. *Expert Opin Drug Del* **2008,** *5* (8), 825-836.

127. Huang, Y.; Chiang, C. Y.; Lee, S. K.; Gao, Y.; Hu, E. L.; De Yoreo, J.; Belcher, A. M., Programmable assembly of nanoarchitectures using genetically engineered viruses. *Nano Lett* **2005,** *5* (7), 1429-1434.

128. Tseng, R. J.; Tsai, C.; Ma, L.; Ouyang, J.; Ozkan, C. S.; Yang, Y., Digital memory device based on tobacco mosaic virus conjugated with nanoparticles. *Nature Nanotechnology* **2006,** *1* (1), 72-77.

129. Aljabali, A. A. A.; Barclay, J. E.; Cespedes, O.; Rashid, A.; Staniland, S. S.; Lomonossoff, G. P.; Evans, D. J., Charge Modified Cowpea Mosaic Virus Particles for Templated Mineralization. *Advanced Functional Materials* **2011,** *21* (21), 4137-4142.

130. Aljabali, A. A. A.; Shah, S. N.; Evans-Gowing, R.; Lomonossoff, G. P.; Evans, D. J., Chemically-coupled-peptide-promoted virus nanoparticle templated mineralization. *Integrative Biology* **2011,** *3* (2), 119-125.

131. Gao, C.; Li, W. W.; Morimoto, H.; Nagaoka, Y.; Maekawa, T., Magnetic carbon nanotubes: Synthesis by electrostatic self-assembly approach and application in biomanipulations. *J Phys Chem B* **2006,** *110* (14), 7213-7220.

132. Correa-Duarte, M. A.; Perez-Juste, J.; Sanchez-Iglesias, A.; Giersig, M.; Liz-Marzan, L. M., Aligning Au nanorods by using carbon nanotubes as templates. *Angew Chem Int Edit* **2005,** *44* (28), 4375-4378.

133. Zhou, X. S.; Yin, Y. X.; Wan, L. J.; Guo, Y. G., Self-Assembled Nanocomposite of Silicon Nanoparticles Encapsulated in Graphene through Electrostatic Attraction for Lithium-Ion Batteries. *Adv Energy Mater* **2012,** *2* (9), 1086-1090.

134. Kabachii, Y. A.; Golub, A. S.; Kochev, S. Y.; Lenenko, N. D.; Abramchuk, S. S.; Antipin, M. Y.; Valetsky, P. M.; Stein, B. D.; Mahmoud, W. E.; A-Ghamdi, A. A.; Bronstein, L. M., Multifunctional Nanohybrids by Self-Assembly of Monodisperse Iron Oxide Nanoparticles and Nanolamellar MoS2 Plates. *Chem Mater* **2013,** *25* (12), 2434-2440.

135. Caruso, F.; Caruso, R. A.; Mohwald, H., Nanoengineering of inorganic and hybrid hollow spheres by colloidal templating. *Science* **1998,** *282* (5391), 1111-1114.

136. Peng, S.; Lee, Y. M.; Wang, C.; Yin, H. F.; Dai, S.; Sun, S. H., A Facile Synthesis of Monodisperse Au Nanoparticles and Their Catalysis of CO Oxidation. *Nano Res* **2008,** *1* (3), 229-234.

137. Dabbousi, B. O.; RodriguezViejo, J.; Mikulec, F. V.; Heine, J. R.; Mattoussi, H.; Ober, R.; Jensen, K. F.; Bawendi, M. G., (CdSe)ZnS core-shell quantum dots: Synthesis and characterization of a size series of highly luminescent nanocrystallites. *J Phys Chem B* **1997,** *101* (46), 9463-9475.

138. Wang, F.; Mao, C. B., Nanotubes connected to a micro-tank: hybrid micro-/nano-silica architectures transcribed from living bacteria as bioreactors. *Chem Commun* **2009,** (10), 1222-1224.

139. Li, D.; Newton, S. M. C.; Klebba, P. E.; Mao, C. B., Flagellar Display of Bone-Protein-Derived Peptides for Studying Peptide-Mediated Biomineralization. *Langmuir* **2012,** *28* (47), 16338-16346.

140. Ikeda, T.; Kamiya, R.; Yamaguchi, S., Excretion of Flagellin by a Short-Flagella Mutant of Salmonella-Typhimurium. *J Bacteriol* **1983,** *153* (1), 506-510.

141. Krueger, K. M.; Al-Somali, A. M.; Mejia, M.; Colvin, V. L., The hydrodynamic size of polymer stabilized nanocrystals. *Nanotechnology* **2007,** *18* (47), 475709.

142. Su, K. H.; Wei, Q. H.; Zhang, X.; Mock, J. J.; Smith, D. R.; Schultz, S., Interparticle coupling effects on plasmon resonances of nanogold particles. *Nano Lett* **2003,** *3* (8), 1087-1090.

143. Massart, R., Preparation of Aqueous Magnetic Liquids in Alkaline and Acidic Media. *Ieee T Magn* **1981,** *17* (2), 1247-1248.

144. Chan, W. C. W.; Nie, S. M., Quantum dot bioconjugates for ultrasensitive nonisotopic detection. *Science* **1998,** *281* (5385), 2016-2018.

145. Aydin, K.; Ferry, V. E.; Briggs, R. M.; Atwater, H. A., Broadband polarization-independent resonant light absorption using ultrathin plasmonic super absorbers. *Nature communications* **2011,** *2,* 517.

146. Park, S. G.; Mun, C.; Lee, M.; Jeon, T. Y.; Shim, H. S.; Lee, Y. J.; Kwon, J. D.; Kim, C. S.; Kim, D. H., 3D Hybrid Plasmonic Nanomaterials for Highly Efficient Optical Absorbers and Sensors. *Adv Mater* **2015,** *27* (29), 4290-4295.

147. Wang, D.; Zhu, W.; Best, M. D.; Camden, J. P.; Crozier, K. B., Wafer-scale metasurface for total power absorption, local field enhancement and single molecule Raman spectroscopy. *Sci Rep* **2013,** *3*, 2867.

148. Zhou, L.; Tan, Y.; Ji, D.; Zhu, B.; Zhang, P.; Xu, J.; Gan, Q.; Yu, Z.; Zhu, J., Self-assembly of highly efficient, broadband plasmonic absorbers for solar steam generation. *Science advances* **2016,** *2* (4), e1501227.

149. Hedayati, M. K.; Javaherirahim, M.; Mozooni, B.; Abdelaziz, R.; Tavassolizadeh, A.; Chakravadhanula, V. S.; Zaporojtchenko, V.; Strunkus, T.; Faupel, F.; Elbahri, M., Design of a perfect black absorber at visible frequencies using plasmonic metamaterials. *Adv Mater* **2011,** *23* (45), 5410-5414.

150. Moreau, A.; Ciraci, C.; Mock, J. J.; Hill, R. T.; Wang, Q.; Wiley, B. J.; Chilkoti, A.; Smith, D. R., Controlled-reflectance surfaces with film-coupled colloidal nanoantennas. *Nature* **2012,** *492* (7427), 86-89.

151. Hagglund, C.; Zeltzer, G.; Ruiz, R.; Thomann, I.; Lee, H. B.; Brongersma, M. L.; Bent, S. F., Self-assembly based plasmonic arrays tuned by atomic layer deposition for extreme visible light absorption. *Nano Lett* **2013,** *13* (7), 3352-3357.

152. Li, D.; Qu, X.; Newton, S. M.; Klebba, P. E.; Mao, C., Morphology-controlled synthesis of silica nanotubes through pH- and sequence-responsive morphological change of bacterial flagellar biotemplates. *J Mater Chem* **2012,** *22*, 15702-15709.

153. Li, D.; Mathew, B.; Mao, C., Biotemplated synthesis of hollow double-layered core/shell titania/silica nanotubes under ambient conditions. *Small* **2012,** *8* (23), 3691-3697.

154. Bardy, S. L.; Ng, S. Y.; Jarrell, K. F., Prokaryotic motility structures. *Microbiology* **2003,** *149* (Pt 2), 295-304.

155. Silverman, M.; Simon, M., Flagellar rotation and the mechanism of bacterial motility. *Nature* **1974,** *249* (452), 73-74.

156. Mao, C.; Flynn, C. E.; Hayhurst, A.; Sweeney, R.; Qi, J.; Georgiou, G.; Iverson, B.; Belcher, A. M., Viral assembly of oriented quantum dot nanowires. *Proceedings of the National Academy of Sciences of the United States of America* **2003,** *100* (12), 6946-51.

157. Chen, X.; Gerasopoulos, K.; Guo, J.; Brown, A.; Wang, C.; Ghodssi, R.; Culver, J. N., Virus-enabled silicon anode for lithium-ion batteries. *Acs Nano* **2010,** *4* (9), 5366-5372.

158. Ikeda, T.; Kamiya, R.; Yamaguchi, S., Excretion of flagellin by a short-flagella mutant of Salmonella typhimurium. *J Bacteriol* **1983,** *153* (1), 506-510.

159. Gwo, S.; Chen, H. Y.; Lin, M. H.; Sun, L.; Li, X., Nanomanipulation and controlled self-assembly of metal nanoparticles and nanocrystals for plasmonics. *Chemical Society reviews* **2016,** *45* (20), 5672-5716.

160. Abdelaziz, R.; Disci-Zayed, D.; Hedayati, M. K.; Pohls, J. H.; Zillohu, A. U.; Erkartal, B.; Chakravadhanula, V. S.; Duppel, V.; Kienle, L.; Elbahri, M., Green chemistry and nanofabrication in a levitated Leidenfrost drop. *Nature communications* **2013,** *4*, 2400.

161. Kraemer, D.; Jie, Q.; McEnaney, K.; Cao, F.; Liu, W. S.; Weinstein, L. A.; Loomis, J.; Ren, Z. F.; Chen, G., Concentrating solar thermoelectric generators with a peak efficiency of 7.4%. *Nat Energy* **2016,** *1*, 1-8.

162. Kraemer, D.; Poudel, B.; Feng, H. P.; Caylor, J. C.; Yu, B.; Yan, X.; Ma, Y.; Wang, X.; Wang, D.; Muto, A.; McEnaney, K.; Chiesa, M.; Ren, Z.; Chen, G., High-performance flat-panel solar thermoelectric generators with high thermal concentration. *Nat Mater* **2011,** *10* (7), 532-538.

163. Morrison, S. J.; Spradling, A. C., Stem cells and niches: Mechanisms that promote stem cell maintenance throughout life. *Cell* **2008,** *132* (4), 598-611.

164. Lutolf, M. P.; Blau, H. M., Artificial Stem Cell Niches. *Adv Mater* **2009,** *21* (32-33), 3255-3268.

165. Even-Ram, S.; Artym, V.; Yamada, K. M., Matrix control of stem cell fate. *Cell* **2006,** *126* (4), 645-647.

166. Watt, F. M.; Hogan, B. L. M., Out of Eden: Stem cells and their niches. *Science* **2000,** *287* (5457), 1427-1430.

167. Oh, S.; Brammer, K. S.; Li, Y. S. J.; Teng, D.; Engler, A. J.; Chien, S.; Jin, S., Stem cell fate dictated solely by altered nanotube dimension. *P Natl Acad Sci USA* **2009,** *106* (7), 2130-2135.

168. Kilian, K. A.; Bugarija, B.; Lahn, B. T.; Mrksich, M., Geometric cues for directing the differentiation of mesenchymal stem cells. *P Natl Acad Sci USA* **2010,** *107* (11), 4872-4877.

169. Kubota, H.; Avarbock, M. R.; Brinster, R. L., Growth factors essential for self-renewal and expansion of mouse spermatogonial stem cells. *P Natl Acad Sci USA* **2004,** *101* (47), 16489-16494.

170. Discher, D. E.; Mooney, D. J.; Zandstra, P. W., Growth Factors, Matrices, and Forces Combine and Control Stem Cells. *Science* **2009,** *324* (5935), 1673-1677.

171. Yamashita, Y. M.; Fuller, M. T.; Jones, D. L., Signaling in stem cell niches: lessons from the Drosophila germline. *J Cell Sci* **2005,** *118* (4), 665-672.

172. Duncan, A. W.; Rattis, F. M.; DiMascio, L. N.; Congdon, K. L.; Pazianos, G.; Zhao, C.; Yoon, K.; Cook, J. M.; Willert, K.; Gaiano, N.; Reya, T., Integration of Notch and Wnt signaling in hematopoietic stem cell maintenance. *Nat Immunol* **2005,** *6* (3), 314-322.

173. Zhu, A. J.; Haase, I.; Watt, F. M., Signaling via beta 1 integrins and mitogen-activated protein kinase determines human epidermal stem cell fate in vitro. *P Natl Acad Sci USA* **1999,** *96* (12), 6728-6733.

174. Artavanis-Tsakonas, S.; Rand, M. D.; Lake, R. J., Notch signaling: Cell fate control and signal integration in development. *Science* **1999,** *284* (5415), 770-776.

175. Martino, M. M.; Mochizuki, M.; Rothenfluh, D. A.; Rempel, S. A.; Hubbell, J. A.; Barker, T. H., Controlling integrin specificity and stem cell differentiation in 2D and 3D environments through regulation of fibronectin domain stability. *Biomaterials* **2009,** *30* (6), 1089-1097.

176. Hynes, R. O., Integrins - Versatility, Modulation, and Signaling in Cell-Adhesion. *Cell* **1992,** *69* (1), 11-25.

177. Jeschke, B.; Meyer, J.; Jonczyk, A.; Kessler, H.; Adamietz, P.; Meenen, N. M.; Kantlehner, M.; Goepfert, C.; Nies, B., RGD-peptides for tissue engineering of articular cartilage. *Biomaterials* **2002,** *23* (16), 3455-3463.

178. Hersel, U.; Dahmen, C.; Kessler, H., RGD modified polymers: biomaterials for stimulated cell adhesion and beyond. *Biomaterials* **2003,** *24* (24), 4385-4415.

179. Garcia, A. J.; Reyes, C. D., Bio-adhesive surfaces to promote osteoblast differentiation and bone formation. *J Dent Res* **2005,** *84* (5), 407-413.

180. Tosatti, S.; Schwartz, Z.; Campbell, C.; Cochran, D. L.; VandeVondele, S.; Hubbell, J. A.; Denzer, A.; Simpson, J.; Wieland, M.; Lohmann, C. H.; Textor, M.; Boyan, B. D., RGD-containing peptide GCRGYGRGDSPG reduces enhancement of osteoblast differentiation by poly(L-lysine)-graft-poly(ethylene glycol)-coated titanium surfaces. *J Biomed Mater Res A* **2004,** *68A* (3), 458-472.

181. Xu, H.; Cao, B. R.; George, A.; Mao, C. B., Self-Assembly and Mineralization of Genetically Modifiable Biological Nanofibers Driven by beta-Structure Formation. *Biomacromolecules* **2011,** *12* (6), 2193-2199.

182. Liu, A. H.; Abbineni, G.; Mao, C. B., Nanocomposite Films Assembled from Genetically Engineered Filamentous Viruses and Gold Nanoparticles: Nanoarchitecture- and Humidity-Tunable Surface Plasmon Resonance Spectra. *Adv Mater* **2009,** *21* (9), 1001-1005.

183. Livak, K. J.; Schmittgen, T. D., Analysis of relative gene expression data using real-time quantitative PCR and the 2(T)(-Delta Delta C) method. *Methods* **2001,** *25* (4), 402-408.

184. Chiang, C. Y.; Mello, C. M.; Gu, J. J.; Silva, E. C. C. M.; Van Vliet, K. J.; Belcher, A. M., Weaving genetically engineered functionality into mechanically robust virus fibers. *Adv Mater* **2007,** *19* (6), 826-832.

185. Lin, Y.; Balizan, E.; Lee, L. A.; Niu, Z. W.; Wang, Q., Self-Assembly of Rodlike Bio-nanoparticles in Capillary Tubes. *Angew Chem Int Edit* **2010,** *49* (5), 868-872.

186. Biggs, M. J. P.; Richards, R. G.; Gadegaard, N.; McMurray, R. J.; Affrossman, S.; Wilkinson, C. D. W.; Oreffo, R. O. C.; Dalby, M. J., Interactions with nanoscale topography: Adhesion quantification and signal transduction in cells of osteogenic and multipotent lineage. *J Biomed Mater Res A* **2009,** *91A* (1), 195-208.

187. Biggs, M. J. P.; Richards, R. G.; McFarlane, S.; Wilkinson, C. D. W.; Oreffo, R. O. C.; Dalby, M. J., Adhesion formation of primary human osteoblasts and the functional response of mesenchymal stem cells to 330 nm deep microgrooves. *J R Soc Interface* **2008,** *5* (27), 1231-1242.

188. Engler, A. J.; Sen, S.; Sweeney, H. L.; Discher, D. E., Matrix elasticity directs stem cell lineage specification. *Cell* **2006,** *126* (4), 677-689.

189. Dalby, M. J.; Gadegaard, N.; Tare, R.; Andar, A.; Riehle, M. O.; Herzyk, P.; Wilkinson, C. D. W.; Oreffo, R. O. C., The control of human mesenchymal cell differentiation using nanoscale symmetry and disorder. *Nat Mater* **2007,** *6* (12), 997-1003.

190. Buttery, L. D. K.; Bourne, S.; Xynos, J. D.; Wood, H.; Hughes, F. J.; Hughes, S. P. F.; Episkopou, V.; Polak, J. M., Differentiation of osteoblasts and in vitro bone formation from murine embryonic stem cells. *Tissue Eng* **2001,** *7* (1), 89-99.

191. Bilousova, G.; Jun, D. H.; King, K. B.; De Langhe, S.; Chick, W. S.; Torchia, E. C.; Chow, K. S.; Klemm, D. J.; Roop, D. R.; Majka, S. M., Osteoblasts Derived from Induced Pluripotent Stem Cells Form Calcified Structures in Scaffolds Both in Vitro and in Vivo. *Stem Cells* **2011,** *29* (2), 206-216.

192. Schneider, R. K.; Puellen, A.; Kramann, R.; Raupach, K.; Bornemann, J.; Knuechel, R.; Perez-Bouza, A.; Neuss, S., The osteogenic differentiation of adult bone marrow and perinatal umbilical mesenchymal stem cells and matrix remodelling in three-dimensional collagen scaffolds. *Biomaterials* **2010,** *31* (3), 467-480.

193. Keselowsky, B. G.; Collard, D. M.; Garcia, A. J., Integrin binding specificity regulates biomaterial surface chemistry effects on cell differentiation. *P Natl Acad Sci USA* **2005,** *102* (17), 5953-5957.

Appendix A: List of Abbreviations

1D	one-dimensional
2D	two-dimensional
3D	three-dimensional
aECM	artificial extracellular matrix
AFM	atomic force microscope
ALP	alkaline phosphatase
Arbp	acidic ribosomal phosphoprotein
AuNPs	gold nanoparticles
AuNWs	gold nanowires
COL	collagen I-α1
CNTs	carbon nanotubes
DAPI	4,6-diamidino-2-phenylindole
DMF	dimethylformamide
DSSC	dye-sensitized solar cell
ECM	extracellular matrix
EDX	energy-dispersive X-ray
HAP	hydroxyapatite
LIB	lithium ion battery
LSPR	localized surface plasmon resonance
MNPs	magnetic nanoparticles
MPA	3-mercaptopropionic acid
MSCs	mesenchymal stem cells

MTT	3-(4,5-dimethylthiazol-2-yl)-2,5-diphenyl tetrazolium bromide
NIR	near infrared
NPs	nanoparticles
OAm	oleylamine
OCN	osteocalcin
OPN	osteopontin
PBS	phosphate buffered saline
PCR	polymerase chain reaction
PEG	polyethylene glycol
PEI	polyethyleneimine
PI	isoelectric point
pNPP	p-nitrophenyl phosphate
PVP	polyvinylpyrrolidone
QDs	quantum dots
Ra	average surface roughness
s-PEI	small molecular weight PEI
SEM	scanning electron microscope
SNTs	silica nanotubes
STEG	solar thermoelectric generation
SWNT	single-walled carbon nanotube
TEG	thermoelectric generation
TEM	transmission electron microscope
TMV	tobacco mosaic virus

UA	uranyl acetate
WT	wild type

Appendix B: List of Copyrights and Permissions

ROYAL SOCIETY OF CHEMISTRY LICENSE TERMS AND CONDITIONS

Oct 18, 2017

This Agreement between Ms. Lin Wang ("You") and Royal Society of Chemistry ("Royal Society of Chemistry") consists of your license details and the terms and conditions provided by Royal Society of Chemistry and Copyright Clearance Center.

License Number	4211731290340
License date	Oct 18, 2017
Licensed Content Publisher	Royal Society of Chemistry
Licensed Content Publication	Journal of Materials Chemistry
Licensed Content Title	Morphology-controlled synthesis of silica nanotubes through pH- and sequence-responsive morphological change of bacterial flagellar biotemplates
Licensed Content Author	Dong Li,Xuewei Qu,Salete M. C. Newton,Philip E. Klebba,Chuanbin Mao
Licensed Content Date	May 21, 2012
Licensed Content Volume	22
Licensed Content Issue	31
Type of Use	Thesis/Dissertation
Requestor type	academic/educational
Portion	figures/tables/images
Number of figures/tables/images	1
Format	print and electronic
Distribution quantity	10
Will you be translating?	no
Order reference number	
Title of the thesis/dissertation	BIONANOFIBER-BASED NANOSTRUCTURE FABRICATION AND APPLICATION
Expected completion date	Dec 2017
Estimated size	130
Requestor Location	Ms. Lin Wang 4821 Baker St NORMAN, OK 73072 United States Attn: Ms. Lin Wang
Billing Type	Invoice
Billing Address	Ms. Lin Wang 4821 Baker St NORMAN, OK 73072

NATURE PUBLISHING GROUP LICENSE
TERMS AND CONDITIONS

Oct 18, 2017

This Agreement between Ms. Lin Wang ("You") and Nature Publishing Group ("Nature Publishing Group") consists of your license details and the terms and conditions provided by Nature Publishing Group and Copyright Clearance Center.

License Number	4211740803545
License date	Oct 18, 2017
Licensed Content Publisher	Nature Publishing Group
Licensed Content Publication	Nature
Licensed Content Title	Complete atomic model of the bacterial flagellar filament by electron cryomicroscopy
Licensed Content Author	Koji Yonekura, Saori Maki-Yonekura and Keiichi Namba
Licensed Content Date	Aug 7, 2003
Licensed Content Volume	424
Licensed Content Issue	6949
Type of Use	reuse in a dissertation / thesis
Requestor type	academic/educational
Format	print and electronic
Portion	figures/tables/illustrations
Number of figures/tables/illustrations	2
High-res required	no
Figures	Figure 2 and Figure 3
Author of this NPG article	no
Your reference number	
Title of your thesis / dissertation	BIONANOFIBER-BASED NANOSTRUCTURE FABRICATION AND APPLICATION
Expected completion date	Dec 2017
Estimated size (number of pages)	130
Requestor Location	Ms. Lin Wang 4821 Baker St NORMAN, OK 73072 United States Attn: Ms. Lin Wang
Billing Type	Invoice
Billing Address	Ms. Lin Wang 4821 Baker St NORMAN, OK 73072

THE AMERICAN ASSOCIATION FOR THE ADVANCEMENT OF SCIENCE LICENSE TERMS AND CONDITIONS

Oct 18, 2017

This Agreement between Ms. Lin Wang ("You") and The American Association for the Advancement of Science ("The American Association for the Advancement of Science") consists of your license details and the terms and conditions provided by The American Association for the Advancement of Science and Copyright Clearance Center.

License Number	4211951001073
License date	Oct 18, 2017
Licensed Content Publisher	The American Association for the Advancement of Science
Licensed Content Publication	Science
Licensed Content Title	Virus-Based Toolkit for the Directed Synthesis of Magnetic and Semiconducting Nanowires
Licensed Content Author	Chuanbin Mao,Daniel J. Solis,Brian D. Reiss,Stephen T. Kottmann,Rozamond Y. Sweeney,Andrew Hayhurst,George Georgiou,Brent Iverson,Angela M. Belcher
Licensed Content Date	Jan 9, 2004
Licensed Content Volume	303
Licensed Content Issue	5655
Volume number	303
Issue number	5655
Type of Use	Thesis / Dissertation
Requestor type	Scientist/individual at a research institution
Format	Print and electronic
Portion	Figure
Number of figures/tables	2
Order reference number	
Title of your thesis / dissertation	BIONANOFIBER-BASED NANOSTRUCTURE FABRICATION AND APPLICATION
Expected completion date	Dec 2017
Estimated size(pages)	130
Requestor Location	Ms. Lin Wang 4821 Baker St NORMAN, OK 73072 United States Attn: Ms. Lin Wang
Billing Type	Invoice
Billing Address	Ms. Lin Wang 4821 Baker St NORMAN, OK 73072

JOHN WILEY AND SONS LICENSE TERMS AND CONDITIONS

Oct 18, 2017

This Agreement between Ms. Lin Wang ("You") and John Wiley and Sons ("John Wiley and Sons") consists of your license details and the terms and conditions provided by John Wiley and Sons and Copyright Clearance Center.

License Number	4211951422645
License date	Oct 18, 2017
Licensed Content Publisher	John Wiley and Sons
Licensed Content Publication	Advanced Materials
Licensed Content Title	Inorganic–Organic Nanotube Composites from Template Mineralization of Tobacco Mosaic Virus
Licensed Content Author	Wayne Shenton,Trevor Douglas,Mark Young,Gerald Stubbs,Stephen Mann
Licensed Content Date	Mar 1, 1999
Licensed Content Pages	4
Type of use	Dissertation/Thesis
Requestor type	University/Academic
Format	Print and electronic
Portion	Figure/table
Number of figures/tables	3
Original Wiley figure/table number(s)	Figure 2, Figure 3 and Figure 4
Will you be translating?	No
Title of your thesis / dissertation	BIONANOFIBER-BASED NANOSTRUCTURE FABRICATION AND APPLICATION
Expected completion date	Dec 2017
Expected size (number of pages)	130
Requestor Location	Ms. Lin Wang 4821 Baker St NORMAN, OK 73072 United States Attn: Ms. Lin Wang
Publisher Tax ID	EU826007151
Billing Type	Invoice
Billing Address	Ms. Lin Wang 4821 Baker St NORMAN, OK 73072 United States Attn: Ms. Lin Wang

ACS Publications
Most Trusted. Most Cited. Most Read.

Title: Bacteriophage Bundles with Prealigned Ca2+ Initiate the Oriented Nucleation and Growth of Hydroxylapatite

Author: Fuke Wang, Binrui Cao, Chuanbin Mao

Publication: Chemistry of Materials

Publisher: American Chemical Society

Date: Jun 1, 2010

Copyright © 2010, American Chemical Society

Logged in as:
Lin Wang
Account #:
3001207351

LOGOUT

PERMISSION/LICENSE IS GRANTED FOR YOUR ORDER AT NO CHARGE

This type of permission/license, instead of the standard Terms & Conditions, is sent to you because no fee is being charged for your order. Please note the following:

- Permission is granted for your request in both print and electronic formats, and translations.
- If figures and/or tables were requested, they may be adapted or used in part.
- Please print this page for your records and send a copy of it to your publisher/graduate school.
- Appropriate credit for the requested material should be given as follows: "Reprinted (adapted) with permission from (COMPLETE REFERENCE CITATION). Copyright (YEAR) American Chemical Society." Insert appropriate information in place of the capitalized words.
- One-time permission is granted only for the use specified in your request. No additional uses are granted (such as derivative works or other editions). For any other uses, please submit a new request.

If credit is given to another source for the material you requested, permission must be obtained from that source.

ELSEVIER LICENSE
TERMS AND CONDITIONS

Oct 18, 2017

This Agreement between Ms. Lin Wang ("You") and Elsevier ("Elsevier") consists of your license details and the terms and conditions provided by Elsevier and Copyright Clearance Center.

License Number	4211960407104
License date	Oct 18, 2017
Licensed Content Publisher	Elsevier
Licensed Content Publication	Biomaterials
Licensed Content Title	Controlled growth and differentiation of MSCs on grooved films assembled from monodisperse biological nanofibers with genetically tunable surface chemistries
Licensed Content Author	Haibao Zhu,Binrui Cao,Zipeng Zhen,Ayyagari A. Laxmi,Dong Li,Shaorong Liu,Chuanbin Mao
Licensed Content Date	Jul 1, 2011
Licensed Content Volume	32
Licensed Content Issue	21
Licensed Content Pages	9
Start Page	4744
End Page	4752
Type of Use	reuse in a thesis/dissertation
Intended publisher of new work	other
Portion	figures/tables/illustrations
Number of figures/tables/illustrations	1
Format	both print and electronic
Are you the author of this Elsevier article?	No
Will you be translating?	No
Original figure numbers	Figure 1
Title of your thesis/dissertation	BIONANOFIBER-BASED NANOSTRUCTURE FABRICATION AND APPLICATION
Expected completion date	Dec 2017
Estimated size (number of pages)	130
Requestor Location	Ms. Lin Wang 4821 Baker St NORMAN, OK 73072 United States Attn: Ms. Lin Wang

NATURE PUBLISHING GROUP LICENSE
TERMS AND CONDITIONS

Oct 18, 2017

This Agreement between Ms. Lin Wang ("You") and Nature Publishing Group ("Nature Publishing Group") consists of your license details and the terms and conditions provided by Nature Publishing Group and Copyright Clearance Center.

License Number	4211961029972
License date	Oct 18, 2017
Licensed Content Publisher	Nature Publishing Group
Licensed Content Publication	Nature Nanotechnology
Licensed Content Title	Virus-templated self-assembled single-walled carbon nanotubes for highly efficient electron collection in photovoltaic devices
Licensed Content Author	Xiangnan Dang, Hyunjung Yi, Moon-Ho Ham, Jifa Qi, Dong Soo Yun, Rebecca Ladewski
Licensed Content Date	Apr 24, 2011
Licensed Content Volume	6
Licensed Content Issue	6
Type of Use	reuse in a dissertation / thesis
Requestor type	academic/educational
Format	print and electronic
Portion	figures/tables/illustrations
Number of figures/tables/illustrations	2
High-res required	no
Figures	Figure 1 and Figure 2
Author of this NPG article	no
Your reference number	
Title of your thesis / dissertation	BIONANOFIBER-BASED NANOSTRUCTURE FABRICATION AND APPLICATION
Expected completion date	Dec 2017
Estimated size (number of pages)	130
Requestor Location	Ms. Lin Wang 4821 Baker St NORMAN, OK 73072 United States Attn: Ms. Lin Wang
Billing Type	Invoice
Billing Address	Ms. Lin Wang 4821 Baker St NORMAN, OK 73072

ELSEVIER LICENSE
TERMS AND CONDITIONS

Oct 18, 2017

This Agreement between Ms. Lin Wang ("You") and Elsevier ("Elsevier") consists of your license details and the terms and conditions provided by Elsevier and Copyright Clearance Center.

License Number	4211961201652
License date	Oct 18, 2017
Licensed Content Publisher	Elsevier
Licensed Content Publication	Journal of Power Sources
Licensed Content Title	Electrochemical performance of the nanostructured biotemplated V2O5 cathode for lithium-ion batteries
Licensed Content Author	Ekaterina Pomerantseva,Konstantinos Gerasopoulos,Xinyi Chen,Gary Rubloff,Reza Ghodssi
Licensed Content Date	May 15, 2012
Licensed Content Volume	206
Licensed Content Issue	n/a
Licensed Content Pages	6
Start Page	282
End Page	287
Type of Use	reuse in a thesis/dissertation
Intended publisher of new work	other
Portion	figures/tables/illustrations
Number of figures/tables/illustrations	2
Format	both print and electronic
Are you the author of this Elsevier article?	No
Will you be translating?	No
Original figure numbers	Figure 1 and figure 3
Title of your thesis/dissertation	BIONANOFIBER-BASED NANOSTRUCTURE FABRICATION AND APPLICATION
Expected completion date	Dec 2017
Estimated size (number of pages)	130
Requestor Location	Ms. Lin Wang 4821 Baker St NORMAN, OK 73072 United States Attn: Ms. Lin Wang
Publisher Tax ID	98-0397604